NASA CR-152391

NASA-CR-152391-VOL-2

ANALYSIS OF WIND TUNNEL TEST RESULTS FOR A 9.39-PER CENT SCALE MODEL OF A VSTOL FIGHTER/ATTACK AIRCRAFT

VOLUME II - EVALUATION OF PREDICTION METHODOLOGIES

DR. J. R. LUMMUS
G. T. JOYCE
C. D. O'MALLEY

Prepared under Contract NAS2-10344
by
General Dynamics
Fort Worth Division
for
Ames Research Center

NATIONAL AERONAUTICS AND SPACE ADMINISTRATION

1. Report No.	2. Government Accession No.	3. Recipient's Catalog No.
NASA CR-152391		

4. Title and Subtitle	5. Report Date
Analysis of Wind Tunnel Test Results for a 9.39-percent Scale Model of a VSTOL Fighter/Attack Aircraft	October, 1980
	6. Performing Organization Code

7. Author(s)	8. Performing Organization Report No.
Dr. J. R. Lummus, G. T. Joyce, C. D. O'Malley	
	10. Work Unit No.

9. Performing Organization Name and Address	11. Contract or Grant No.
General Dynamics/Fort Worth Division P. O. Box 748 Fort Worth, Texas 76101	NAS2-10344
	13. Type of Report and Period Covered
12. Sponsoring Agency Name and Address	Contractor Final Report Sept. 10, 1979-Feb. 10, 1981
NASA, AMES Research Center, Moffett Field, Ca 94035	14. Sponsoring Agency Code

15. Supplementary Notes

AMES Research Center Technical Monitor W. P. Nelms
(415) 965-5880

16. Abstract

The results of a series of NASA AMES wind tunnel tests of a General Dynamics vectored-engine-over wing, Navy VSTOL fighter/attack configuration have been analyzed to (1) assess prediction method capabilities, (2) evaluate geometry variations such as multiple canard longitudinal locations and strake shapes, and (3) evaluate the effects of configuration changes associated with varying the propulsive lift system from a jet-diffuser ejector to a Remote Augmentation Lift System (RALS). Configuration modification and additional testing and analysis are recommended to adequately evaluate the configuration potential.

This document is presented in four volumes - Volume I - Study Overview, Volume II - Evaluation of Prediction Methodologies, Volume III - Effects of Configuration Variations from Baseline E205 Configuration on Aerodynamic Characteristics, and Volume IV - RALS R104 Aerodynamic Characteristics and Comparisons with E205 Configuration Aerodynamic Characteristics.

17. Key Words (Suggested by Author(s))	18. Distribution Statement
CANARD, STRAKE, AERODYNAMIC PREDICTION METHODS	

19. Security Classif. (of this report)	20. Security Classif. (of this page)	21. No. of Pages	22. Price*
UNCLASSIFIED	UNCLASSIFIED		

For sale by the National Technical Information Service, Springfield, Virginia 22161

VOLUME II - EVALUATION OF PREDICTION METHODOLOGIES

TABLE OF CONTENTS

Predicted vs Test E205 Baseline Configuration Aerodynamic Characteristics

LIST OF FIGURES

LIST OF FIGURES (CONT'D.)

LIST OF FIGURES (CONT'D.)

LIST OF FIGURES (CONT'D.)

LIST OF FIGURES (CONT'D.)

LIST OF FIGURES (CONT'D.)

LIST OF FIGURES (CONT'D.)

VOLUME II

LIST OF TABLES

LIST OF SYMBOLS

a. English Symbols

A	axial force, lb (N)
a.c.	aerodynamic center, $\%\bar{c}$
AR	aspect ratio
b	span, in. (m)
$\bar{c}$, MAC	mean aerodynamic chord, in. (m)
C_A	axial force coefficient
$C_{A_{ejector}}$	axial force coefficient due to ejector
C_D	drag coefficient
$C_{D_{AERO}}$	aero-only drag coefficient (no thrust increments included)
$C_{D_{min}}$	minimum drag coefficient
C_{D_E}	equivalent drag coefficient
$C_{D_{RAM}}$	ram-drag coefficient (engine inlet)
C_{D_t}	total drag coefficient
C_L	lift coefficient
$C_{L_{buffet}}$	buffet-onset lift coefficient
C_{L_E}	equivalent lift coefficient
$C_{L_{max}}$	maximum lift coefficient
$C_{L_{aero}}$	aero-only lift coefficient (no thrust increments included)
C_{L_t}	total lift coefficient
C_l	rolling moment coefficient

C_{l_β}	rolling moment derivative due to sideslip, 1/deg
C_{m_E}	equivalent pitching moment coefficient
$C_{m_{X_{\bar{c}}}}$	pitching moment coefficient about x percent $\bar{c}$
C_{m_o}	zero lift pitching moment coefficient
C_{m_t}	total pitching moment coefficient
C_N	normal force coefficient
C_n	yawing moment coefficient
C_{n_β}	yawing moment derivative due to sideslip, 1/deg
C_T	thrust coefficient, $\frac{T}{qS_{REF}}$
C_Y	side force coefficient
C_{Y_β}	side force derivative due to sideslip, 1/deg
CMU, C	ideal thrust coefficient, $\dot{w}\ Vj/gqS_{REF}$
D	drag, lb(N)
e	span efficiency factor
ESF	engine scale factor, $\frac{T}{T_{ESF = 1.0}}$
IGE	in ground effect
L	lift, lb(N)
L_Γ	lift due to supercirculation, lb(N)
l	rolling moment, ft lb (Nm)
M	Mach number
m	pitching moment, ft lb(Nm)
NPR	nozzle pressure ratio, $\frac{\text{Total Pressure}}{P}$

N	normal force, lb(kg)
n	yawing moment, ft lb (Nm)
OGE	out of ground effect
P	freestream static pressure, lb/ft^2 $(\frac{N}{m^2})$
P_o	freestream total pressure, lb/ft^2, $(\frac{N}{m^2})$
q	freestream dynamic pressure, lb/ft^2 $(\frac{N}{m^2})$
S_C	canard exposed area, ft^2 (m^2)
S_{ref}	reference area, $ft^2(m^2)$ (usually equal to S_W)
STOL	short takeoff or landing
S_W	area of trapezoidal wing extended to centerline, $ft^2(m^2)$
Sv_T	exposed area of vertical tail, $ft^2(m^2)$
T	thrust, lb(N)
V_∞	freestream velocity, ft/sec, knots (m/sec)
V_j	jet velocity based on isentropic expansion from nozzle camber total pressure to freestream static pressure, ft/sec (m/sec)
VSTOL	vertical or short takeoff or landing
VTOL	vertical takeoff or landing
VEO-Wing	vectored engine over wing
$\dot{w}$	weight flow, lb/sec (kg/sec)
X_{cp}	action point of circulation lift relative to leading edge of MAC

b. Greek Symbols

α alpha	angle of attack, deg
β, beta	angle of sideslip, deg
Γ	supercirculation
γ	flight path angle, deg
δ_C, δ_i	canard deflection (positive, leading-edge up), deg
δ_{TE}, δ_F	VEO-Wing nozzle and outboard flaperon deflection, deg; except for aileron action the flaperons and VEO-Wing nozzle flaps always deflect together.
θ	pitch attitude angle, deg
θ_J	jet thrust deflection out of VEO-Wing nozzles when deflected, $_{TE}$, deg
Λ_{LE}	leading-edge sweep angle, deg
λ	taper ratio, $\frac{\text{tip chord}}{\text{root chord}}$
ϕ	ejector measured thrust/isentropic supply thrust (where isentropic supply thrust is the thrust which would be obtained from supplied air at the nozzle exit of pressures and flow rates expanded at isentropically to ambient pressure)

c. Model Symbols

B_1	VSTOL ejector configuration E-205 basic fuselage with fuselage strake that blends the fuselage to the inboard section to the wing.
B_2	VSTOL RALS configuration R-104 basic fuselage
C_1	All moveable nacelle-mounted horizontal canard of VSTOL ejector configuration E-205 in the mid-location
C_2	Horizontal canard H_1 in VSTOL E-205 or RALS R104 fwd-location
C_3	Horizontal canard in VSTOL E-205 or RALS R104 aft-location
N	VSTOL ejector configuration E-205 or RALS R104 VEO-wing nacelle
S_1	Baseline strake on E205 configuration
S_2	High sweep strake on E205 configuration
S_3	Low sweep strake on E205 configuration
V	All moveable vertical tail of VSTOL ejector configuration E-205 or RALS R104
W_1	VSTOL ejector configuration E-205 wing with linear elements between SS 96.496 and SS 223.695
W_2	VSTOL RALS configuration R-104 wing with linear elements between SS 87.231 and SS 214.430

VOLUME II - EVALUATION OF PREDICTION METHODOLOGIES

One of the primary objectives of this investigation is an evaluation of current prediction methodologies to estimate the aerodynamic uncertainties identified in Reference 1 for the E205 configuration described in Volume I, Section 3.1. This evaluation was accomplished by comparing predicted and wind tunnel test data in three major categories: untrimmed longitudinal aerodynamics, trimmed longitudinal aerodynamics, and lateral-directional aerodynamic characteristics.

1.0 Untrimmed Longitudinal Aerodynamics

Figures 1-1 through 1-2 demonstrate the variation of the baseline E205 wind tunnel model lift, drag, and pitching moment with angle of attacks and Mach number for $.2 \leq M \leq 1.2$. Although these data will be analyzed in some detail in subsequent sections, they are presented here to provide an overview of the basic trends; that is, increasing lift slope (in the linear α range), increasing positive stability and increasing minimum drag with increasing Mach No. as expected. The high angle-of-attack, M = .4 characteristics obtained in the low speed wind tunnel test (Figure 1-1) agree well with the M = .4 data obtained in the transonic test (Figure 1-2).

1.1 Aerodynamic Center vs Mach No.

The aerodynamic-center (a.c.) travel with Mach No. is a real driver in the E205 design. As explained in Reference 1, the E205 configuration is longitudinally, statically unstable to achieve the VEO-wing nozzle benefits. The predicted instability levels are greater than can be presently tolerated. The maximum allowable instability dictated by control system limitations is approximately 15-18% MAC. Therefore, the Flight Control System (FCS) will be used to augment the stability to the required level of frequency and damping. As part of this augmentation the flight control computer will be used to schedule the canard as a function of Mach number and angle of attack to achieve the desired level of static longitudinal stability. Obviously then, the aerodynamic-center travel is an important parameter that must be accurately predicted. Estimates of the E205 configuration aerodynamic-center travel with Mach No. have been made by using the Carmichael Procedure (Reference 2) and the Datcom method (Reference 3). Figure 1-3 presents a General Dynamics a.c.-prediction-accuracy correlation for the Carmichael procedure for various configurations, including the VEO-wing fighter model of Reference 4. The correction vs

Mach No. indicated for the VEO-wing fighter model was applied to the Carmichael predictions for the E205 baseline configuration (a similar configuration) to produce the corrected Carmichael estimates, which are compared with wind tunnel results in Figure 1-4 for a zero-degree canard deflection and with canard off. The Datcom estimate for canard at a zero-degree deflection for M = .4 is also shown for reference and shows a significant disparity between the prediction methods.

It is very difficult to predict the E205 a.c. with either of these existing methods because of the unusual aspects of the configuration: the wide, flat body with separated nacelles, the relatively blunt forward strake, etc. However, the Carmichael procedure plus the correlation-correction developed by General Dynamics did yield surprisingly good predictions at most subsonic and transonic Mach numbers. There are, however, some significant discrepancies for Mach No. > 1.6 (the predictions are conservative). The predicted trends and levels agree rather well with the test data below Mach No. = 1.6 and the accuracy of the predictions in this speed regime is certainly satisfactory for preliminary design purposes. For Mach No.'s $\geq$ 1.6, the predictions are unsatisfactory.

1.2 Zero-Lift Pitching Moment Coefficient (Cmo) vs Mach No.

Figure 1-5 compares the test and predicted variations of zero-lift pitching moment with Mach No. for the baseline E205 configuration ($\delta c = 0°$). (The effects of removing the canards and wings as well as shifting the canards to alternate longitudinal locations are also indicated from the test data described in Volume III).

The estimated Cmo variation presented in Figure 1-5 for the baseline configuration is the direct result of the experimental data bases used for predicting the aerodyamics of each speed regime for the full-scale aircraft (as described in Volume I, Section 3.2) because no prediction method per se is available to handle predicting the Cmo for a configuration like the E205 with the unusual combinations of body, strake, nacelle, and wing camber and the subsequent interference between the components. However, the Carmichael procedure would have probably provided some guidance to doing a better job of predicting C_{m_0}. Figure 1-5 emphasizes the inability to predict the Cmo variation; further analysis of the canard and wing trailing-edge flap effectiveness and the resulting trim (Section 2.0) indicate the real importance of being able to accurately predict and tailor the Cmo characteristics.

1.3 Minimum Drag vs Mach No.

The estimated minimum drag variation with Mach No. for the E205 wind tunnel model baseline configuration ($\delta c = 0°$)

is compared with the wind tunnel results in Figure 1-6. The estimated model minimum drag was derived from the estimated full-scale aircraft minimum drag according to the equation shown at the bottom of Table 1-1. Table 1-1 from Reference 1 has been modified to demonstrate how the estimated wind tunnel model minimum drag was developed from the full scale airplane minimum drag at various Mach Nos. by removing the increments for roughness and protuberance drag (because it's a "smooth" wind tunnel model), flap scrub drag (because the model is unpowered), and the missiles and launcher drag (because the model, unlike the airplane, has no missiles and launchers); minimum drag corrections for Reynolds Number differences between the full-scale and model were also applied as well as corrections to the supersonic wave drag for differences between the full-scale airplane lines and the wind tunnel model lines. (Note the respective cross-sectional area distributions in Figures 1-7 and 1-8.) The inlet spill drag increments were determined experimentally for the E205 wind tunnel model as described in Volume I and added to the estimated model minimum drag variation with Mach No., making possible the direct comparison of model estimated and test data shown in Figure 1-6.

This comparison indicates that the prediction methods described in Volume I, are very effective in the subsonic and transonic speed regimes. In fact, good agreement is achieved for $M \leq 1.2$. For $1.2 \leq$ Mach No. ≤ 2.0 the prediction methods tend to underestimate the wind tunnel data. There are probably two causes for this low estimate: (1) uncertainty in the estimated increment due to the lines modifications for the aft sting and (2) uncertainty in the interference drag for this type of configuration.

Figure 1-9 shows a plot of the variation with Mach No. of the increment in minimum drag due to the aft sting for several General Dynamics wind tunnel models; these increments were experimentally determined by subtracting drag levels using alternate mounting methods. Note that the added cross-sectional area required for the sting installation (relative to the actual airplane lines) results in a reduction in drag for all of the configurations tested except the VEO-fighter model (Figure 1-9). The complete VEO-fighter configuration results in positive drag increments subsonically and varies from positive to negative to positive as Mach No. varies from 1.2 to 2.0.

The prediction method (the Harris procedure) employed to estimate the supersonic wave drag of the E205 wind tunnel model indicated a drag reduction for the aft sting installation rather than the drag increase indicated (at some Mach numbers by the VEO-fighter configuration model) as shown in

Table 1-1 E205 WIND TUNNEL MODEL MINIMUM DRAG BUILDUP FROM E205 AIRPLANE MINIMUM DRAG BUILDUP (SEE EQUATION (1) BELOW

Sref = 384 ft2

DRAG COMPONENT	MACH NUMBER							
	.2	.4	.6	.8	.9	1.2	1.6	1.8
	(Drag in Counts)							
Friction	166.5	149.3	139.0	130.4	126.5	116.0	103.0	90.8
Form	17.2	15.5	14.2	13.4	13.1	-	-	-
Interference	8.2	6.9	10.9	21.0	22.2	-	-	-
Wing Camber	2.1	2.1	2.1	2.1	6.3	9.4	10.4	14.6
Roughness + Protuberance	25.9	25.9	25.9	25.9	25.9	32.5	28.8	25.4
Flap Scrub	32.7	10.9	5.5	4.4	4.4	2.2	1.1	1.1
Wave	-	-	-	-	-	292.3	289.4	281.4
Missiles + Launchers								
(2) Wing-Tip LCLM	7.7	7.7	7.7	7.9	8.7	16.1	14.3	12.2
(2) NAC-MT'D AMRAAM	7.7	7.7	7.7	7.9	8.9	13.5	11.0	7.5
Total $C_{D_{min}}$ Full Scale	268	226	213	213	216	482	458	433
$\Delta C_{D_{min}}$ Scale/RE	9.0	27.2	36.5	42.1	44.2	44.7	44.7	44.7
$\Delta C_{D_{wave}}$ (Full scale to model)	-	-	-	-	-	33.0	33.6	45.6
$\Delta C_{D_{spill}}$ (Model)	0	0	2	5.0	8.0	16.0	15.0	0
Total $C_{D_{min}}$ Model	203	201	204.7	214	220.3	511	496	477

Eq (1) PREDICTED $C_{D_{MIN\ MODEL}} = C_{D_{MIN}}$ FULL SCALE AIRPLANE $- \Delta C_{D_{MIN}}$ ROUGH + PROT. $- \Delta C_{D_{MIN}}$ FLAP SCRUB $- \Delta C_{D_{MIN}}$ MISSILES + LAUNCHERS $+ \Delta C_{D_{MIN}}$ SCALE/RE FULL SCALE TO MODEL $+ \Delta C_{D_{MIN}}$ MODEL SPILL DRAG $+ \Delta C_{D_{WAVE}}$ BETWEEN MODEL AND FULL SCALE LINES INCL. (STING MOD).

Figure 1-9. In fact, the Harris procedure usually predicts a drag reduction for aft-sting modifications where area increases result in reductions in the aft slopes of the cross-sectional area distribution as seen with the E205 wind tunnel model. Since the aft-sting increment was not evaluated experimentally for the E205 configuration, it's impossible to know how much the prediction is off due to using the Harris procedure.

The second reason for the discrepancy between the predicted and test $C_{D_{min}}$ may lie with the inability to predict the interference drag. VEO-wing fighter model wind tunnel data indicate that the interference drag produced by the combination of configuration components is higher than predicted using the same prediction methods as those employed in the E205 prediction. This "excess" interference drag increment from the fighter model has been corrected for reference area and added to the E205 minimum drag prediction shown in Figure 1-10 to demonstrate the upper bound of the predicted drag level that might be expected if the E205 "excess" interference drag were the same as that of the VEO-wing fighter model. Actually, the excess interference drag of the E205 configuration is expected to be different from the VEO-wing fighter because the geometric sources of the interference, i.e., the channel shape between the nacelles and fuselage spine where shocks form at certain speeds, will differ substantially between the two configurations. Since the E205's channel is much more "open," the excess interference is expected to be smaller than that shown in Figure 1-9 based on the VEO-wing fighter model.

Note that the results of two methods for predicting the Mach = .2 minimum drag are compared in Figure 1-6. The $C_{D_{min}} = .0203$ was estimated using the method described above, that is using the normal prediction methods employed by General Dynamics for an arbitrary configuration for which there is no previous wind tunnel data. The $C_{D_{min}} = .0236$ was predicted using the equations described in Volume I Section 3.2 to correct the wind tunnel data from the VEO-wing fighter model and powered research model to a prediction of the E205 configuration. This is the method employed to develop the low speed power-on (and power-off) aerodynamics used for transition and STOL in Reference 1 and described in Section 1.4. It is somewhat surprising that better agreement is achieved with a "generalized" method than with a prediction built up from previous wind tunnel data. One of the reasons for this is a change in component interference drag between the fighter model and the E205 configuration (narrow channel vs wide open strake, etc.).

1.4 Power-Off Untrimmed Lift, Drag, and Pitching Moment

Table 1-2 summarizes the matrix of power-on and power-off, untrimmed and trimmed comparisons of predicted and wind tunnel data for the baseline E205 wind tunnel model that are included in this report. In this section the power-on and power-off untrimmed comparisons are presented while the trimmed power-on and power-off comparisons are presented in Section 2.1.

The predicted power-off, untrimmed lift, drag, and pitching moment curves for the E205 wind tunnel model in the low speed and supersonic speed regimmes are compared with the corresponding wind tunnel data in Figures 1-11 through 1-13 and 1-18 through 1-19. The predicted, transonic power-off untrimmed curves were not developed for the reasons explained in Volume I, Section 3.2.

At Mach No. = .2, the predicted wing-body and wing-body-canard ($\delta_c = 0°$ and $\delta_{TE} = 0°$) power-off lift, drag, and pitching moment coefficients are compared with the wind tunnel data in Figure 1-11. The predicted data were developed as described in Volume I, Section 3.2 based on the VEO-fighter-model wing-body characteristics and research-model canard, flap, and supercirculation increments. The wind tunnel lift, drag, and pitching moment characteristics are in general more favorable than predicted; that is, for a given angle of attack the wind tunnel data exhibits more lift, less drag, and a more negative pitching moment. There is reasonably good agreement between predicted and test wing-body $C_{L\alpha}$ and dCM/dCL in the attached flow region ($\alpha \geq$ 8-10°); the agreement with predicted minimum drag is also acceptable and could be even better if the prediction method employed at other Mach No's were employed at M = .2 (See Section 1.3). Both the predicted and test data indicate early wing separation beginning at α = 8-10° with the wind tunnel model actually producing slightly higher lift and less drag than predicted. The major difference between the predicted and test wing-body data lies in the inability to accurately predict the Cmo of the configuration; the configuration exhibits more effective positive camber (and hence more nose down moment) than expected. This is a surprise since each component was considered geometrically uncambered (except the fuselage which has a large upswept negatively cambered boatail which should produce a positive moment increment).

With the canard on at zero deflection, the agreement between prediction and test data is still reasonably good. However, there is still a substantial difference between the predicted and test Cmo of about the same magnitude observed

Table 1-2 MATRIX OF POWER-ON AND POWER-OFF, TRIMMED AND UNTRIMMED COMPARISONS OF PREDICTED AND WIND TUNNEL DATA FOR THE BASELINE E205 WIND TUNNEL MODEL

POWER	SUBSONIC		TRANSONIC		SUPERSONIC	
	UNTRIMMED	TRIMMED	UNTRIMMED	TRIMMED	UNTRIMMED	TRIMMED
POWER-OFF						
PREDICTED	x	-	-	x	x	-
WIND TUNNEL	x	-	-	x	x	x
POWER-ON						
PREDICTED	x	x	-	x	-	-
WIND TUNNEL	x	x	-	x	-	-

in the wing-body case. As described in Volume III, Section 2.0, the canard effectiveness (Figure 1-11) is larger than predicted because the upwash induced by the E205 wing-body is substantially different from that of the research model which does not have a lifting strake area between the nacelle and fuselage spine like the E205. The highly swept, sharp edged strake of the baseline E205 configuration probably creates a substantial vortex flowfield about the strake which extends outboard even past the nacelle to influence the canard flowfield resulting in a higher upwash than expected using the research model canard effectiveness. The changes in the incremental lift, drag, and pitching moment due to the canard in and out of the presence of the wing (Figures 1-14 through 1-17)indicate the effects on the canard flowfield caused by the wing. Please note that these "canard increments" are (canard on - canard off) at a given canard location and deflection.

The wind tunnel and predicted effects of wing trailing edge flap deflection are shown in Figures 1-12 and 1-13 for δ_{TE} = 10° and 25°. Again, the wind tunnel data is more favorable than predicted with more lift, less drag, and a more negative pitching moment. The major differences are due to the cumulative errors in predicting the wing-body and wing-body-canard configuration (as descussed above) coupled with the errors in predicting the wing trailing edge flap effectiveness. The low speed wing trailing edge flap effectiveness was also derrived from the Research model data which yields more pessimistic flap increments than obtained with the E205 wind tunnel model as seen in Section 1.5.

The predicted and test untrimmed wing-body and wing-body-canard lift, drag, and pitching curves for Mach numbers of 1.2 and 1.6 are compared in Figures 1-18 and 1-19. Canard deflections of 0° and +10° are presented. These comparisons indicate very good agreement between test and predictions at M = 1.2 primarily because the predictions are based on VEO-wing fighter model data (rather than Research model data) which, although not totally like the E205 configuration, is more similar than the Research model used for low speed and transonic predictions. At M = 1.6 the errors in predicting C_{m_0} and CD_{min} are not acceptable. It should be noted that there are no power effects to be added to the supersonic aerodynamics. Figures 1-20 and 1-21 present the Mach = 1.8 and 2.0 wind tunnel results for δ_c = 0°, δ_{TE} = 0° for completeness.

Comparisons of the M = .2 predicted and wind tunnel untrimmed "total" aerodynamic coefficients (which include power effects) were developed according to the equations of Volume I, Section 3.2. These "total" aerodynamic coefficients were developed by adding the several components to the unpowered "aero-only" coefficients described above; the components are as follows: the incremental lift, drag, and pitching moment due supercirculation (from the Powered Research model testing described in Reference 1), the engine ram drag, the ejector ram drag, and the vectored thrust components from the forward ejectors and the Veo-nozzles.

Therefore the same power effects for a given flight condition are added to the unpowered predicted and wind tunnel aerodynamics to arrive at the untrimmed powered comparisons shown in Figures 1-22 through 1-25 at Mach number .2 and C_T TOTAL = 1.81. These data were of course developed to determine comparisons between the trimmed power-on aerodynamics presented in Section 2.0. As explained in Section 2.0 the thrust split between the VEO-nozzles and the forward ejector (Figure 1-26) is a function of angle of attack and flap deflection for a given Mach number and power setting (which fixes C_T TOTAL) and are prescribed to arrive at a reasonable trimmed angle of attack range. Therefore, the thrust split is varying along the lift, drag, and pitching moment curves of Figures 1-22 through 1-25 for a given flap deflection according to Figure 1-26.

Since the same power effects have been added to the predicted and wind tunnel unpowered data to arrive at the comparisons in Figure 1-22, the differences are still primarily attributable to those described above with the unpowered comparisons. In general, the test data shows more favorable aerodynamics than predicted with higher lift, less drag, and a more nose down pitching moment for a given angle of attack. A major part of the difference between the wind tunnel and predicted characteristics lies with the error in predicting Cmo but there is also an error in predicting the trailing-edge-flap effectiveness as discussed in Section 1.5.

1.5 Wing Trailing-Edge Flap Effectiveness

As noted in Section 1.4, the M = .2 predicted wing trailing-edge flap effectiveness for the E205 configuration was derived from the Research model described in Volume I; the Research model power-off and power-on flap increments were presented for the E205 configuration in Reference 1 as a function of flap deflection, angle of attack, and C . These Research model incremental data were developed in the presence of the undeflected canard and with a fuselage/nacelle/strake arrangement (Volume I) which differs substantially from that of the E205 configuration.

Figures 1-11 through 1-13 together with Figures 1-22 through 1-25 present the M = .2 wind tunnel lift, drag, and pitching moment curves for variations in trailing-edge flap deflections of 0°, 10°, and 25° and variations in canard deflections. These data form the basis for developing the lift, drag, and pitching moment increments due to flap deflection which are shown in Figures 1-35 through 1-45 and compared with the predicted flap increments (relative to flap undeflected) in Figures 1-27 and 1-28. Note that there is a variation of wind-tunnel-flap effectiveness with canard deflection while the predicted increments were developed with the canard undeflected.

The wind tunnel data indicates that at M = .2, the 10°-flap produces more lift than predicted at low α's (< 8°) for all canard deflections. As the canard deflection is increased or decreased from the undeflected position, the downwash on the wing from the canard produces a decrease in flap effectiveness; the flap effectiveness also decreases with increasing angle of attack. The center of pressure and hence the flap pitching moment increment is much less affected by canard deflection. The drag increment is affected by canard deflection but increases with increasing angle of attack.

With the flaps deflected twenty five degrees the same trends are indicated with canard deflection and angle of attack at M = .2. However, the decrease in wind-tunnel-flap lift increment with α and δ_C is much more dramatic than at δ_{TE} = 10°. In general, the low speed flap effectiveness is about as predicted, especially at low α's and δ_C's near zero degrees.

Figures 1-29 through 1-34 provide the transonic (Mach = .6 to 1.2) lift, drag, and pitching moment curves that indicate the effect of wing trailing-edge flap deflection with varying canard deflection and angle of attack. Because of the way the transonic predictions were developed (see Volume I, Section 3.2) predicted flap incremental effects are not available to compare directly with the wind tunnel flap increments presented in Figure 1-35 through 1-43 for δ_c = 10° and 25° at Mach numbers of .6, .9 and 1.2. The effect of increasing Mach number is, in general, to decrease the flap lift increment at a given canard deflection and angle of attack with a small change in pitching moment increment but little change in drag increment.

Figures 1-41 through 1-43 indicate the flap lift, drag, and moment increments at Mach = .6 to 1.2 with the canard removed for δ_{TE} = 10° and 25°. When these increments are compared with Figures 1-35 through 1-40, they indicate that the 10° and 25° flap increments with the canard removed are almost the same as with the canard on at zero degrees deflection (with the exception of the increments for M = .6 and α's > 4° where the canard removed increment behaves like the δ_C = -20° case).

Subsonically, the addition of the canard produces a downwash on the wing, lowering the effective local angle of attack of the wing which reduces the adverse pressure gradient on the upper surface of the wing at the wing trailing edge-flap allowing the flap to work to higher α's before flap separation begins. As the Mach number is increased to .9 the boundary layer is thinned reducing the adverse pressure gradient at the flap so that the addition

of the canard has a less dramatic effect on the flap increment than at lower Mach numbers. Supersonically, (M = 1.2) the flap increments are slightly higher in the presence of the canard (and increase with increasing α).

Figures 1-44 and 1-45 illustrate the lift, drag, and pitching moment increments at M = 1.6 and 2.0 due to deflecting the trailing-edge flap ten degrees in the presence of the canard of varying deflection and with the canard removed. These curves indicate that the canard deflection or presence of the canard has little influence on the flap effectiveness.

1.6 Buffet Onset Characteristics

The buffet characteristics of the ejector vehicle are portrayed in Figures 1-46 through 1-55. The wing bending moment coefficient (C_{rms}), an indicator of buffet, is plotted as a function of angle of attack and Mach numbers in Figures 1-46 and 1-47. At Mach = 0.6, the onset of buffet occur near an angle of attack of 8 degrees. Buffet progresses with increasing angle of attack until the wing stall. As the wing stalls, outboard to inboard, the wing bending moment coefficient decreases and then levels off.

The effect of canard location on the buffet characteristics is displayed in Figures 1-48 through 1-50 for Mach numbers of 0.6 through 1.2. At M = .6, compared to the mid located canard (C1), the forward located canard (C2) has a milder buildup to approximately the same level of intensity. The aft located canard (C3) has a more direct effect in that the intensity is higher and occurs at a lower angle of attack. This same effect is much more pronounced at Mach = 0.9. The intensity with the forward located canard follows the trend of the wing body configurations. At supersonic speeds (M = 1.2) this level of intensity for all the canard location is much milder.

Figures 1-51 through 1-53 contain the variation of C_{rms} for various canard deflections. For modest deflections (+10, -10) the levels of intensity differ little. For the case of large negative canard deflections (-20^{o}) the unporting of the canard causes an earlier buffet onset angle of attack and has a higher intensity as the wing outboard portion stalls first. This stalling is evident from the pitching moment data as well.

Figures 1-54 and 1-55 compare the predicted and wind-tunnel buffet onset angle of attack ($\alpha_{B.O.}$) variation with Mach number for the E205 configuration. In Figure 1-54 three types of $\alpha_{B.O.}$ indicators are compared, CRMS, CN, and CA. As noted in Reference 1, the predicted $\alpha_{B.O.}$ for the baseline E205 configuration were determined by analyzing the axial force data of the VEO-wing fighter configuration force model (from test TF512 conducted at the AEDC PWT 4T Transonic wind tunnel) by using the methods described in Reference 11 of Reference 1. As noted in Reference 1, this VEO-wing fighter configuration model was not specifically instrumented to obtain buffet data but it appears from Figures 1-54 and 1-55 that the data was adequate to do a relatively good job of predicting the wind tunnel results for the E205 model, especially the trends if not the absolute values.

With the $\delta_C = \delta_{TE} = 0°$ (Figure 1-54) the wind tunnel data actually indicates a higher (more favorable) $\alpha_{B.O.}$ than predicted with the Crms and Ca indicators, providing the best agreement with the test data. With the canard removed the limited test data agrees well with the predictions out to Mach .9.

Zero and +10° canard deflections produce higher $\alpha_{B.O.}$ than predicted (Figure 1-55;) while the negative canard deflections induce earlier $\alpha_{B.O.}$ than predicted.

Figure 1-55 also indicates that the baseline longitudinal canard location produces a higher $\alpha_{B.O.}$ than either the forward of aft canard locations.

2.0 TRIMMED LONGITUDINAL AERODYNAMICS

2.1 Trimmed Power-Off Aerodynamics

As noted in Table 1-2, the E205 trimmed power-off transonic and supersonic aerodynamics developed from the untrimmed power-off wind tunnel and predicted characteristics of Section 1.4 are compared in this section as well as the trimmed power-on subsonic and transonic wind tunnel and predicted aerodynamics. Power-off trimmed comparisons between predictions and test data are made at model scale while power-on trimmed comparisons are made for the full scale airplane to confirm the airplane aerodynamics used in the design effort of Reference 1. The subsonic, trimmed power-off aerodynamics were not developed from the test data because the M = .6 power-off data indicates the same trends that would be observed if the M = .2 power-off data were trimmed. The supersonic, trimmed, power-on data are the same as the supersonic power-off data since there are no supersonic power effects anticipated.

One of the original intents in the analysis and comparison of the predicted and wind tunnel data was to determine and compare e's that are comparable to those used in Reference 1 and displayed in Figure 2-1. These e's were developed from the Research model data by removing camber effects to arrive at e's based on an undisplaced drag polar; the source of the camber effects was experimentally determined to be the wing camber (the fuselage being a body of revolution). Because of the fuselage shape of the E205 configuration, there is an apparent fuselage camber effect that was not determined experimentally. Therefore it is impossible to develop comparable polar e's to those presented in Reference 1 so the drag polar comparisons between predictions and test results are discussed in terms of polar "shape" and $C_{D_{min}}$ for power-off and power-on cases which is probably more meaningful to understanding airplane performance than e's any way.

Figures 2-2, 2-3, and 2-6 compare the wind tunnel and predicted power-off trimmed drag polars for Mach numbers of .6, .9, and 2.0, respectively, while both trimmed lift and drag curves are shown in Figures 2-4 and 2-5 for Mach numbers of 1.2 and 1.6.

Trimmed lift curves are not presented for Mach = .6 and .9 because of the manner in which these polar predictions were developed directly from envelope trimmed e's (from Research model data) as explained in Volume I, Section 3.2.

The predicted power-off trimmed drag polars of Figures 2-2 and 2-3 at M = .6 and .9 were developed by using the CDmin estimated for the wind tunnel model (Table 1-1) and the power-off trimmed e's from Figure 2-1 which, as noted above, were developed from the Research model data using the wing trailing-edge flap deflections only for trim (with the canard undeflected) . It was recognized in Reference 1 that these e's were not necessarily the optimum achievable using both canard and flap deflections for trim but they were assumed "representative" of what could be achieved with canard/flap combinations given enough experimental data. Figures 2-2 and 2-6 indicate that this was certainly a reasonable assumption.

Two types of trimmed power-off wind tunnel drag polars are compared with the predicted polars in Figures 2-2 and 2-6: (1) trimming by varying only the wing trailing-edge flap leaving the canard undeflected, and (2) trimming with an envelope of optimum canard and wing trailing-edge flap combinations (within the experimental data limitations). These envelope lift curves and drag polars obtained by trimming with the optimum canard/flap combinations were developed as indicated in Figures 2-7 through 2-10. At M = .6, the wind tunnel polars trimmed with the trailing-edge flap only (canard undeflected) are not as good as predicted; the polar shape is worse and the minimum drag appears to be a little higher than predicted (additional flap-deflection data would be required to accurately determine the trimmed minimum drag). There is closer agreement between the predicted and test trimmed data when using the optimum canard/flap combination derived from Figure 2-7 which yields the envelope polar shown in Figure 2-2.

In fact, if the wind-tunnel-developed envelope polar for M = .6 (trimming with the optimum canard/flap combination) is compared with the predicted polar (trimming with the flap only) at a common $C_{D_{min}}$, the test data actually shows a better polar shape than the prediction for $C_L < .76$. Although trimming with the flap only yields a worse polar shape than trimming with the canard and flap, the trimmed lift for a given angle of attack is lower when trimming with the flap alone but the trimmed L/D is better with the canard and flap combination as shown in Figure 2-11.

At M = .9 (Figure 2-3), the error in predicting $C_{D_{min}}$ is larger than for M = .6. The actual trimmed wind tunnel data (trimming with trailing-edge flap only or with canard/flap combinations) has a slightly better polar shape than the estimated polar. If the minimum drag had been estimated correctly, the agreement between prediction and test would have been quite good. Its interesting to note that trimming with the trailing-edge flap only or with the canard/flap combination makes very little difference in the lift curve and drag polar shape (as evidenced by Figures 2-2 and 2-3);

however, the maximum trimmable α-range with each trim-method is probably different and more test data would be required to determine the α-limits. Figure 2-12 provides a similar comparison of the power-off, trimmed, L/D vs α with each trim method indicating that trim with the optimum canard/flap combination is better for $\alpha < 3°$.

Figure 2-4 compares M = 1.2 predicted and wind tunnel trimmed lift and drag curves. Trimming with the optimum combination of canard and wing trailing-edge flap yields a better polar shape and a higher lift slope than predicted. Trimming with the wing trailing-edge flap only ($\delta C = 0°$) produces a higher $C_{D_{min}}$ than predicted but a better polar shape.

The supersonic predictions were based on the VEO-wing fighter model data rather than the Research model data which was used subsonically. The supersonic predictions were trimmed using the canard only with zero trailing-edge flap deflections which compares with the low-C_L region of the canard/flap trimmed envelope wind tunnel polar of Figure 2-4 (where the zero trailing-edge flap deflection is used at the low-C_L region for trimming). The canard/flap combination does yield a better polar at all C_L's. The difference in the predicted and test values lies primarily then in the inability to predict a.c. and Cmo satisfactorily at the supersonic Mach numbers.

At M =1.6 and 2.0 the errors in predicting CDmin, Cmo and a.c. result in somewhat optimistic predictions as shown in Figures 2-5 and 2-6; the trimmed CDmin is higher than predicted, the polar shape is somewhat worse than predicted, while the CLo is also somewhat lower than predicted. The C_L however is as predicted.

2.2 Trimmed Power-On Aerodynamics

Power-on, trimmed aerodynamics were developed for the full scale E205 airplane configuration by applying minimum drag corrections to the model-scale, power-on, untrimmed data of Section 1.4. Comparisons between predicted and wind- tunnel data corrected to full scale were developed at subsonic and transonic Mach numbers. (There are no power effects at supersonic Mach numbers.)

The low speed, power-on, trimmed comparisons between the predictions and wind tunnel results (corrected to full scale) are indicated in Figures 2-13 and 2-14. The aerodynamic coefficients presented are "total" coefficients which include the thrust related forces and moments and are defined by the equations of Section 3.2 of Volume I.

The maximum total thrust coefficient ($C_{T_{TOTAL}}$) and the ram drag of the engine and ejector are also functions of Mach number. Given the hot-day dynamic pressure, q, the engine and ejector ram drag coefficients are calculated according to the equation defined in Section 4.1.1 of Reference 1. These ram drag coefficients are assumed to act in the axial direction according as shown in Section 3.2 of Volume I. The ejector ram drag coefficient is a function of the air diverted to the ejector, i.e., the thrust split between the main engine and the ejector. These ram drag and thrust components are also used in the referenced equations of Volume I, Section 3.2 to determine the thrust induced forces and moments which are then added to the unpowered aerodynamic data to develop the power-on aerodynamic data. The power-on aerodynamic data for zero canard deflection (from wind tunnel and predictions) are trimmed at Mach = 0.2 using the wing trailing-edge flap and VEO-nozzle plus the forward ejector as trimming devices (see Figures 2-13 and 2-14). The E205 airplane can be trimmed at any reasonable angle of attack depending on the thrust split (between VEO-nozzle and ejector) and the flap/nozzle deflection.

The variation of nozzle deflection with the ratio (VEO-nozzle thrust/total thrust) was shown in Figure 1-26. The relationships between the thrust splits and nozzle deflection were developed and used with the predicted E205 aerodynamic power-off untrimmed data to obtain the predicted, trimmed, power-on lift and drag curves presented in Figure 2-13; these thrust splits and nozzle deflection combinations were also combined with the E205 power-off wind tunnel data to develop the power-on trimmed curves shown in Figure 2-14.

Figures 2-13 and 2-14 indicate that an envelope exists for various attitudes and flap/nozzle deflection where the airplane can be trimmed in pitch. The flap/nozzle deflection can be scheduled as a function of angle-of-attack for operation at a Mach number anywhere in the envelope described in Figures 2-13 and 2-14. It should be recognized that a set of these envelope trim lift-drag polars exists at each Mach number and that at each Mach number, a thrust split is determined which is a function of the flap/nozzle deflection and angle of attack.

Also in Figures 2-13 and 2-14 a constraint line is indicated which represents the case of all thrust being diverted to the nozzles with none to the ejectors; this line represents a limiting case for aircraft operation.

The shape of the drag polars in Figures 2-13 and 2-14 at large flap deflections is typical of a normal airplane configuration; this is not the case at lower flap deflections, as the flap deflection is reduced to zero, increasing angle of attack results in decreased drag. This is the result of higher thrust required from the ejector for trim at low angles of attack (causing an increase in ejector ram drag) than at higher angles of attack. The net result is a decrease in the total drag at the higher angles of attack and lower flap settings which in turn results in the polar shapes exhibited.

Comparing Figures 2-13 and 2-14 further, the wind tunnel corrected data actually shows better performance than the estimated data due to better power-off flap performance.

Although not shown in Figures 2-13 and 2-14, the variation in canard deflection would result in an increase in the size of the trim envelope but is considered a second order effect relative to the trim with nozzle deflection and ejector thrust.

Figures 2-15 and 2-16 compare the Mach = .6 and .9 trimmmed power-on polars for the full scale E205 configuration. The transonic power effects were determined for the predicted and wind tunnel data by calculating the change in induced drag due to power from the power-on and power-off e's (determined from the Research model as described in Figure 2-1. At Mach = .6, C_M = .302 (combat at 10,000 ft altitude) the predicted minimum drag is 14% lower than the corrected wind tunnel data while the corrected test data has a better polar shape than the prediction for C_L <.76 and worse for C_L >.76. The predictions at M = .6 are certainly within acceptable accuracy levels, especially for preliminary design purposes. At M = .9, C_M = .159 the wind tunnel minimum trimmed drag is higher than predicted while the polar shape is substantially better than predicted. The differences in the predicteed and test minimum trimmed drag are probably primarily due to an inability to predict the minimum trim drag penalty since the unpowered, untrimmed $C_{D_{min}}$ differed only by 15 counts (.0237 vs .0222).

Although there are no supersonic power effects, a comparison of the trimmed predicted and wind tunnel drag polars corrected to full-scale is shown in Figure 2-17 for Mach = 1.2. The trimmed minimum drag from the test data and predictions agree well while the polar shape derived from the test data is actually better than that of the predicted polar (just as at model scale).

3.0 LATERAL-DIRECTIONAL AERODYNAMICS

Comparisons between the predicted and tested lateral-directional characteristics of the baseline E205 configuration are examined in this section. In general, the DATCOM procedures were used to develop the predicted characteristics.

3.1 Rigid Sideslip Derivatives

Sideforce coefficient derivative, Cy_β, is displayed in Figure 3-1 as a function of angle of attack for discrete Mach numbers and as a function of Mach number at zero angle of attack. The trend with angle of attack is rather well predicted. However, the level of prediction variation with Mach number is somewhat lower. From the analysis of the R104-model transonic data, it was found that the lower-than-expected variation with Mach number can be principally attributed to the sidewash gradient. The sidewash for the E205 configuration derivative was predicted as 1.0 while the test data indicates a gradient on the order of 0.3. This sidewash gradient effects the vertical tail contribution to sideforce slope which results in the lower sideforce gradient in the test data.

The consequences of the sidewash gradient is even more apparent in the directional stability parameter, C_{n_β}, as shown in Figure 3-2. The test level of C_{n_β} is approximately half that predicted. This is directly attributable to the inaccurate prediction of the sidewash gradient.

The variation of C_{n_β} with angle of attack is also shown in this figure and indicates that while the DATCOM prediction gives only the slightest variation with angle of attack, the test data shows deteriorating stability as angle of attack is increased. This is most notable at the supersonic Mach numbers.

The level of static directional stability, C_{n_β}, for the complete E205 baseline configuration is stable at small angles of attack but degrades to static instability at 18 degrees at M = 0.6 as shown in Figure 3-2. This angle of attack for static directional instability decreases with Mach number. At Mach = 0.9 it is 15 degrees and Mach = 1.2 it is 7.6 degrees. The vertical tail contributes to stability to at least 12 degrees angle of attack at M = 0.9 and possibly higher. (The largest angle of attack tested with the vertical tail off was 12 degrees.) This indicates that the large forward fuselage is a destabilizing element. The effect of the canard either on or off is very small on the directional stability while undeflected. At small angles of

attack, the addition of the canard is slightly destabilizing. Only slight differences in rolling moment due to sideslip can be noted for canard on or off.

The lateral-directional coefficients are fairly linear in the range of sideslip angles tested, -6° to +10°. The variation of rolling moment coefficient with the vertical tail off is only slightly nonlinear. The derivatives discussed above are based on a least square curve fit over a range of two degrees (0 to 2°).

The dihedral effect, C_{l_β}, is shown in Figure 3-3. The trend with angle of attack is predicted fairly well in the linear region when compared to the test data. After the wing becomes ineffective (angles of attack of 8 to 10 degrees because of no leading-edge protection) the prediction-test correlation is less favorable. The characteristic level of C_{l_β} with Mach number at a constant angle of attack is predicted well subsonically but the comparison diverges as supersonic speeds are attained.

3.2 Vertical Tail Effectiveness

Several wind tunnel data runs are available from which the vertical tail effectiveness could be determined. These were the tail-off and vertical-tail-deflection runs for zero angle of attack ($\alpha \approx 0.2°$). Runs with vertical tail deflection were also conducted at 18 degrees angle of attack but unfortunately there was no vertical tail off data at that angle of attack. The results of the analysis of this data indicate a sidewash-sideslip gradient of approximately 1/4. This gradient degrades the effective lift curve slope of the vertical tail. As noted above, the predicted sideforce derivative is higher than the test value primarily because a sidewash gradient of 1.0 was used in predicting the E205 lateral-directional derivatives. This is also reflected in the predicted-test comparison of C_{n_β}. The variation of dihedral effect, however, which is primarily a wing function, was predicted fairly well.

Directional control effectiveness is displayed in Figure 3-4. The level of effectiveness is predicted well at low speed but deteriorates as speed is increased. Apparently the force generated by the vertical tail surface is less than predicted.

3.3 AILERON EFFECTIVENESS

Aileron effectiveness is presented in Figure 3-5. The predicted level is lower than the test results at zero angle of attack. This may be attributable to the DATCOM prediction technique. The location of the ailerons on E205 are immediately behind and outboard of the nacelle. The DATCOM

method does not provide for any interference of this type, either favorable or adverse. As the wing becomes less effective at angles of attack from 6-10 degrees, the aileron effectiveness drops to become less than predicted.

4.0 REFERENCES

1. Lummus, J. R., Study of Aerodynamic Technology for a VSTOL Fighter/Attack Aircraft, NASA CR-152128, May, 1978.

2. Carmichael, R. L., Costellano, C. R., and Chen, F. C., "The Use of Finite Element Methods for Predicting the Aerodynamics of Wing-Body Combinations," Analytical Methods in Aircraft Aerodynamics, NASA SP-228, October, 1969.

3. Hoak, D. E., USAF Stability and Control DATCOM, October, 1960.

4. Heim, E. R., Basic Aerodynamic Data for a Vectored-Engine-Over-Wing Configuration, AEDC-TR-78-1, February 1978.

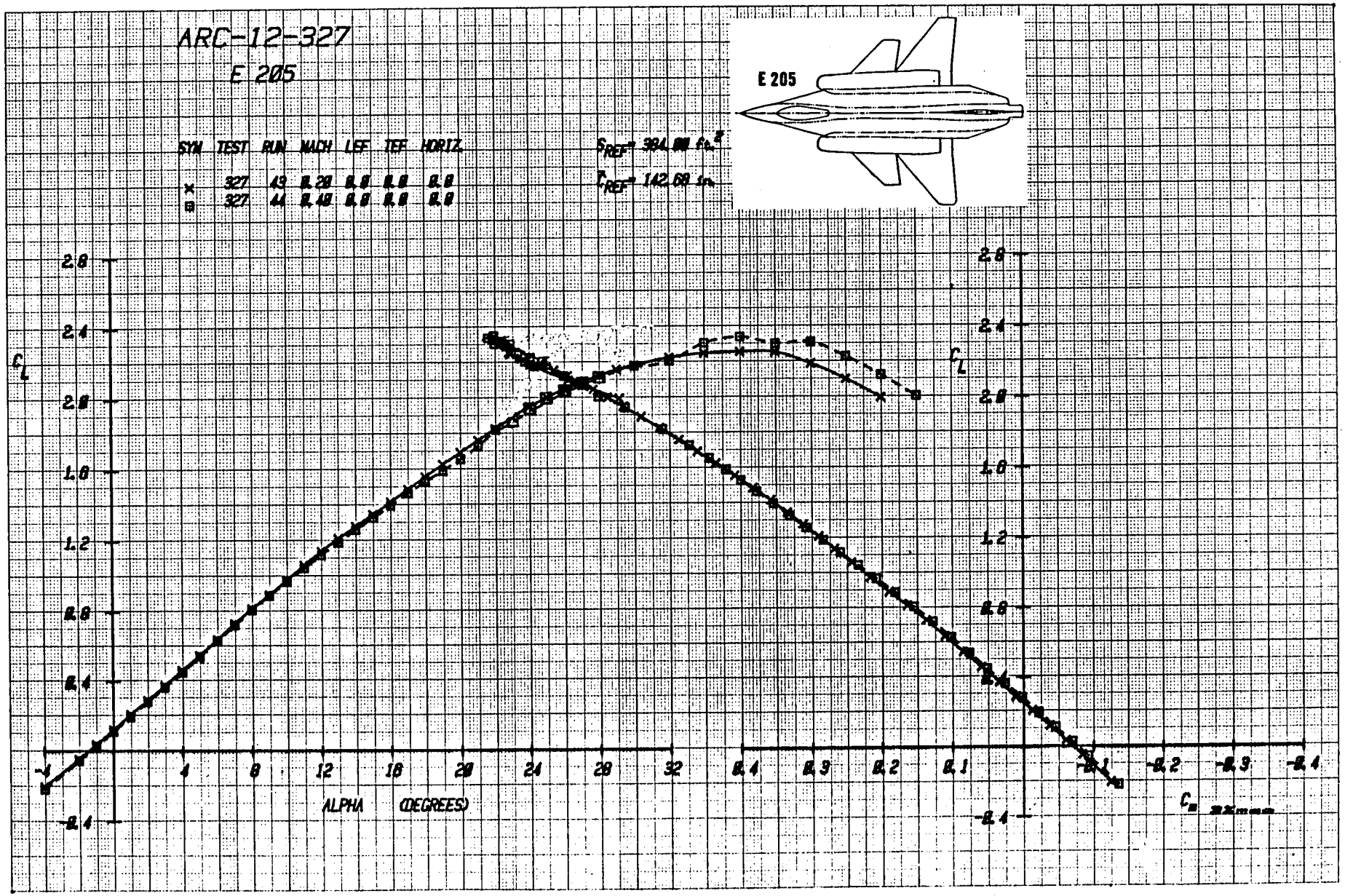

Figure 1-1a Effect of Mach Number on Lift and Moment

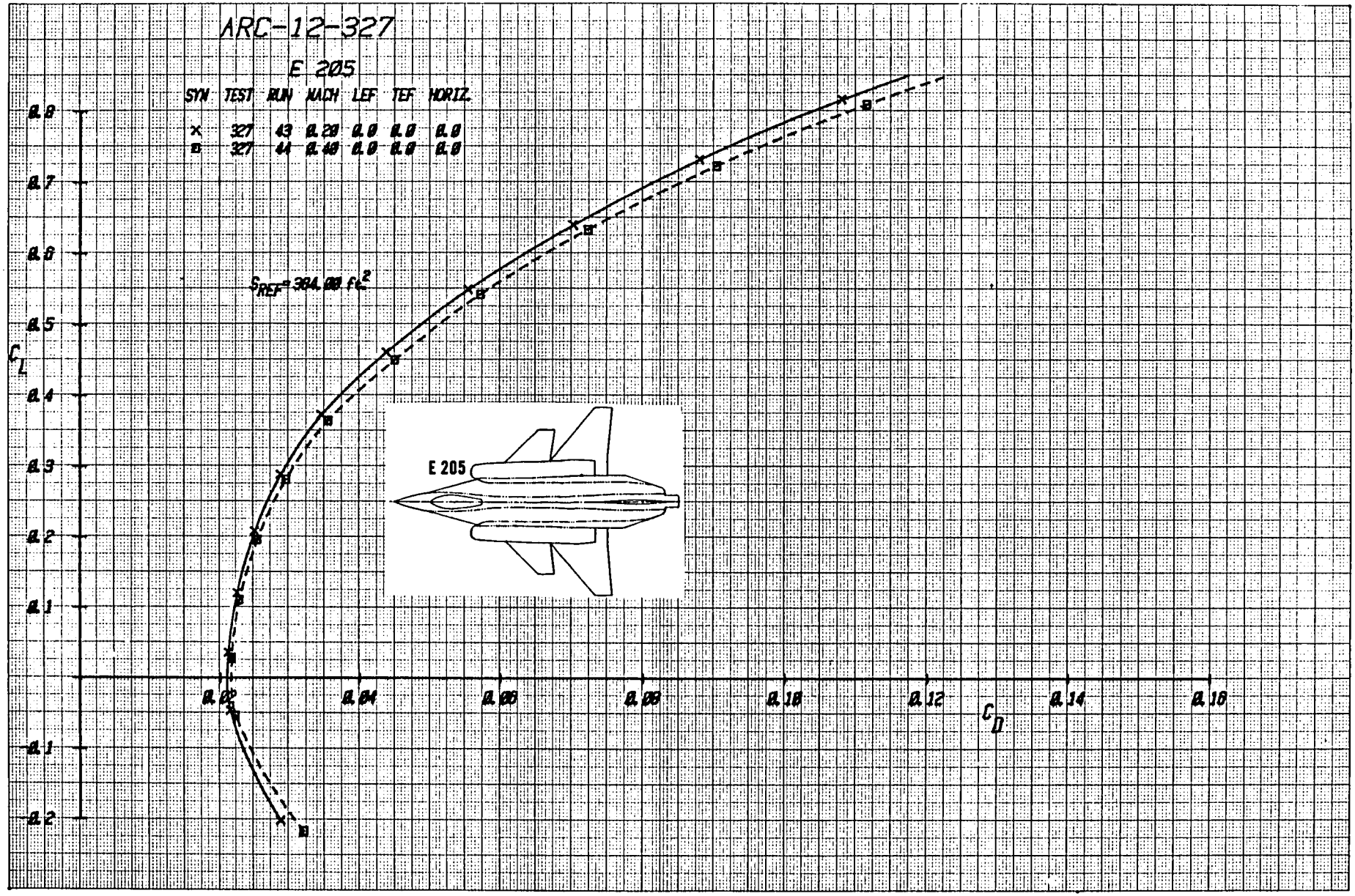

Figure 1-1b Effect of Mach Number on Drag, (Expanded Drag Scale)

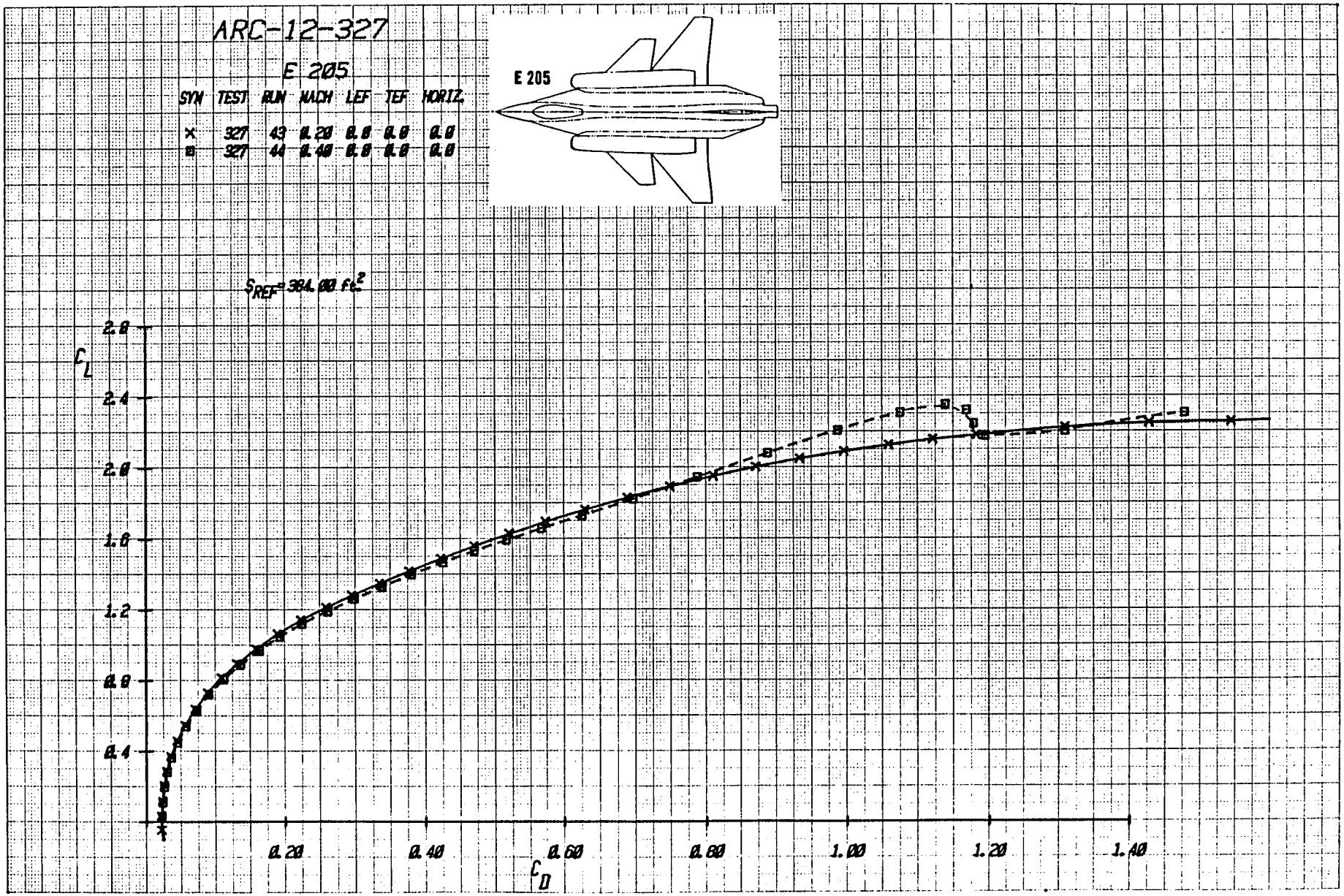

Figure1-1c Effect of Mach Number on Drag

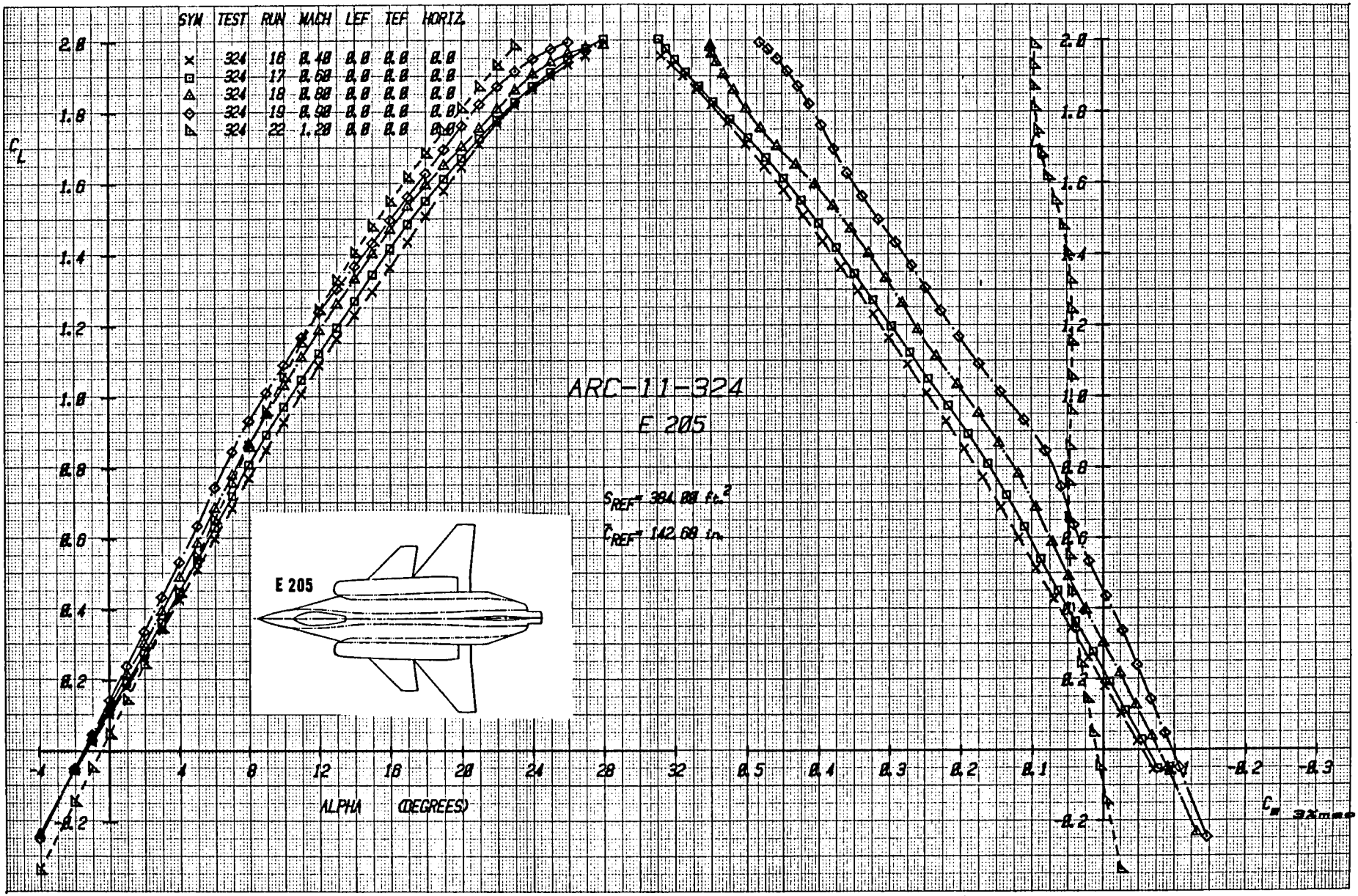

Figure 1-2a Effect of Mach Number on Lift and Moment

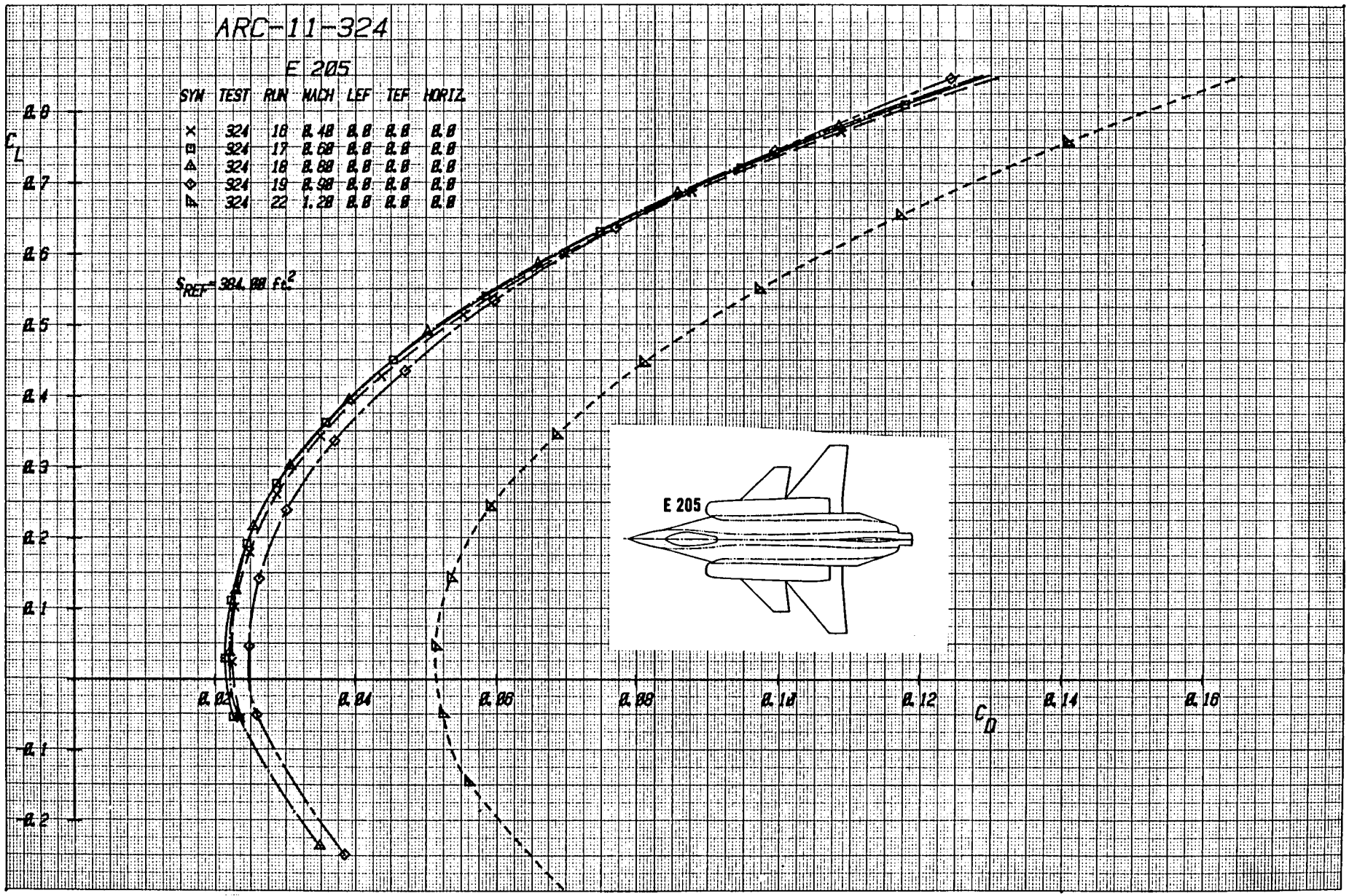

Figure 1-2b Effect of Mach Number on Drag

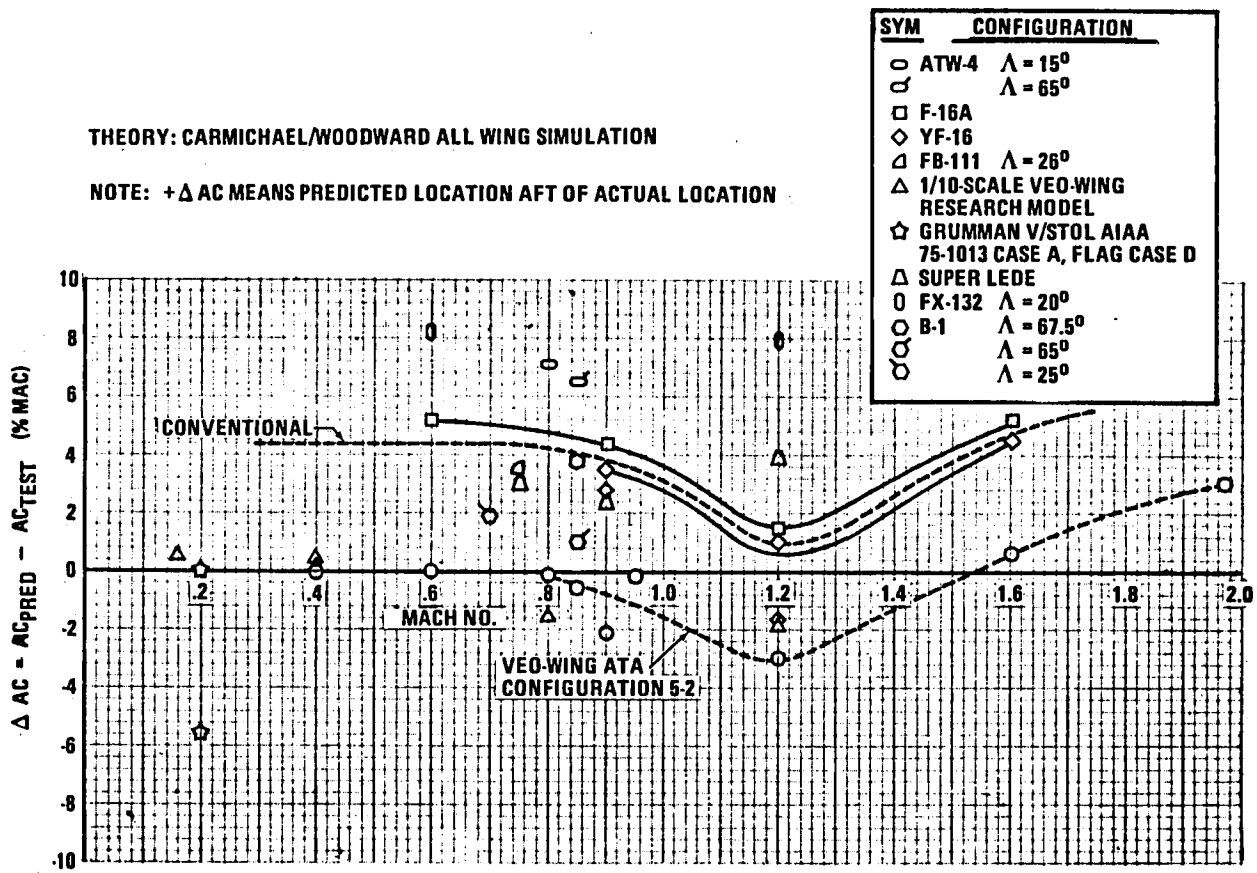

Figure 1-3 Aerodynamic Center Test/Theory Correlation

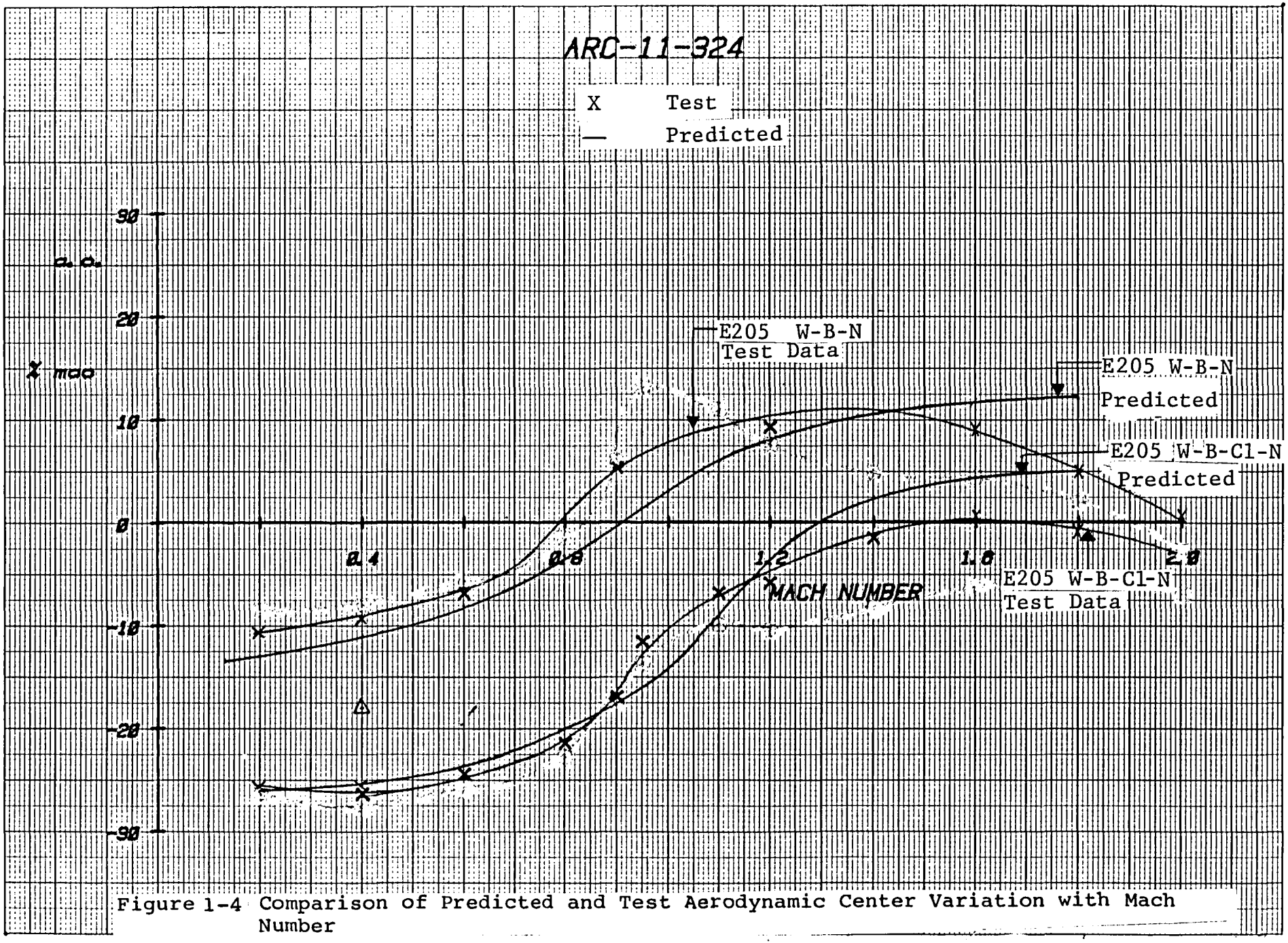

Figure 1-4 Comparison of Predicted and Test Aerodynamic Center Variation with Mach Number

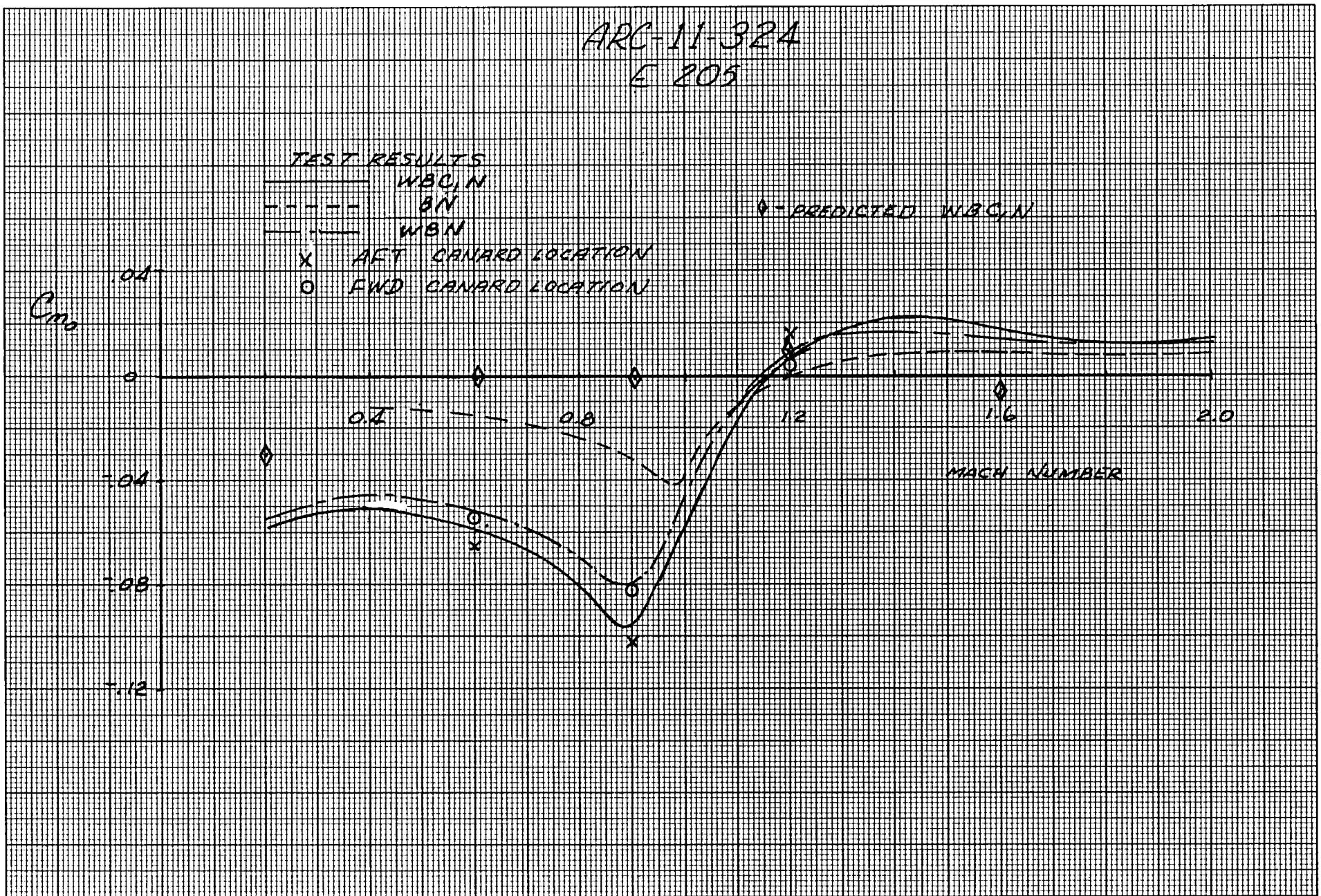

Figure 1-5 Comparison of Predicted and Test E205 Model Zero Lift Pitching Moment Coefficient (C_{M_0}), Variation with Mach Number

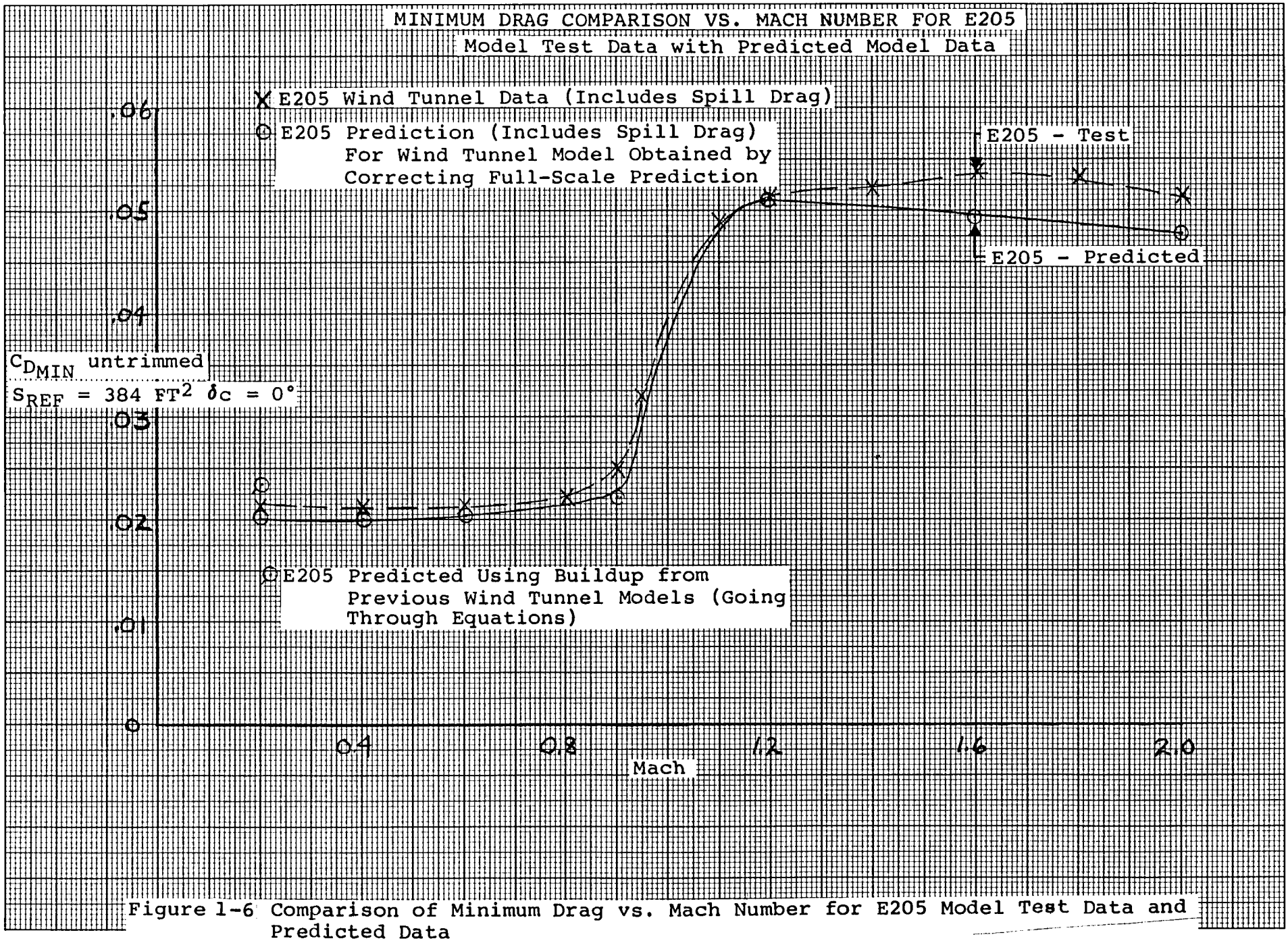

Figure 1-6 Comparison of Minimum Drag vs. Mach Number for E205 Model Test Data and Predicted Data

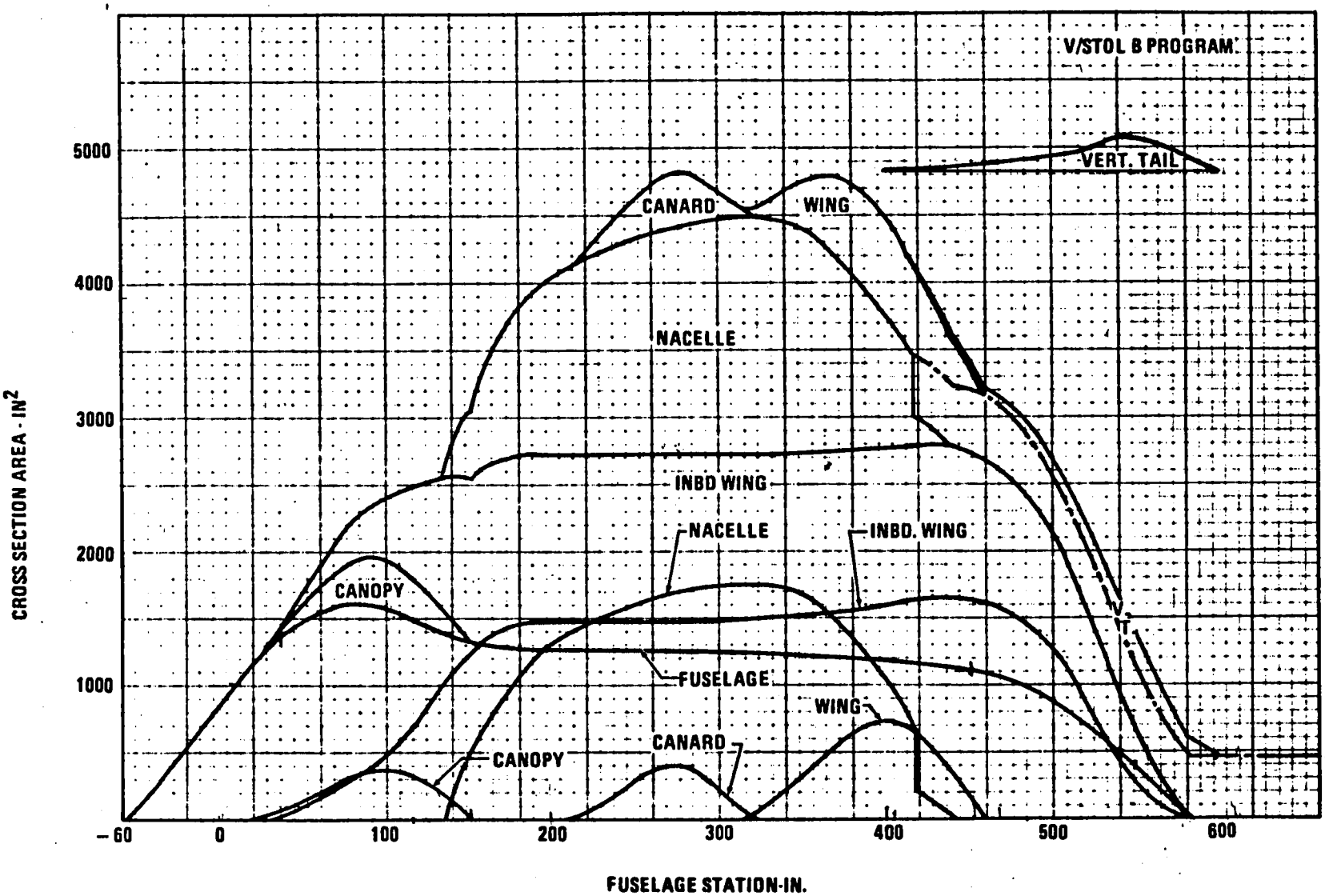

Figure 1-7 E205 Full-Scale Airplane Cross-Sectional Area Distribution

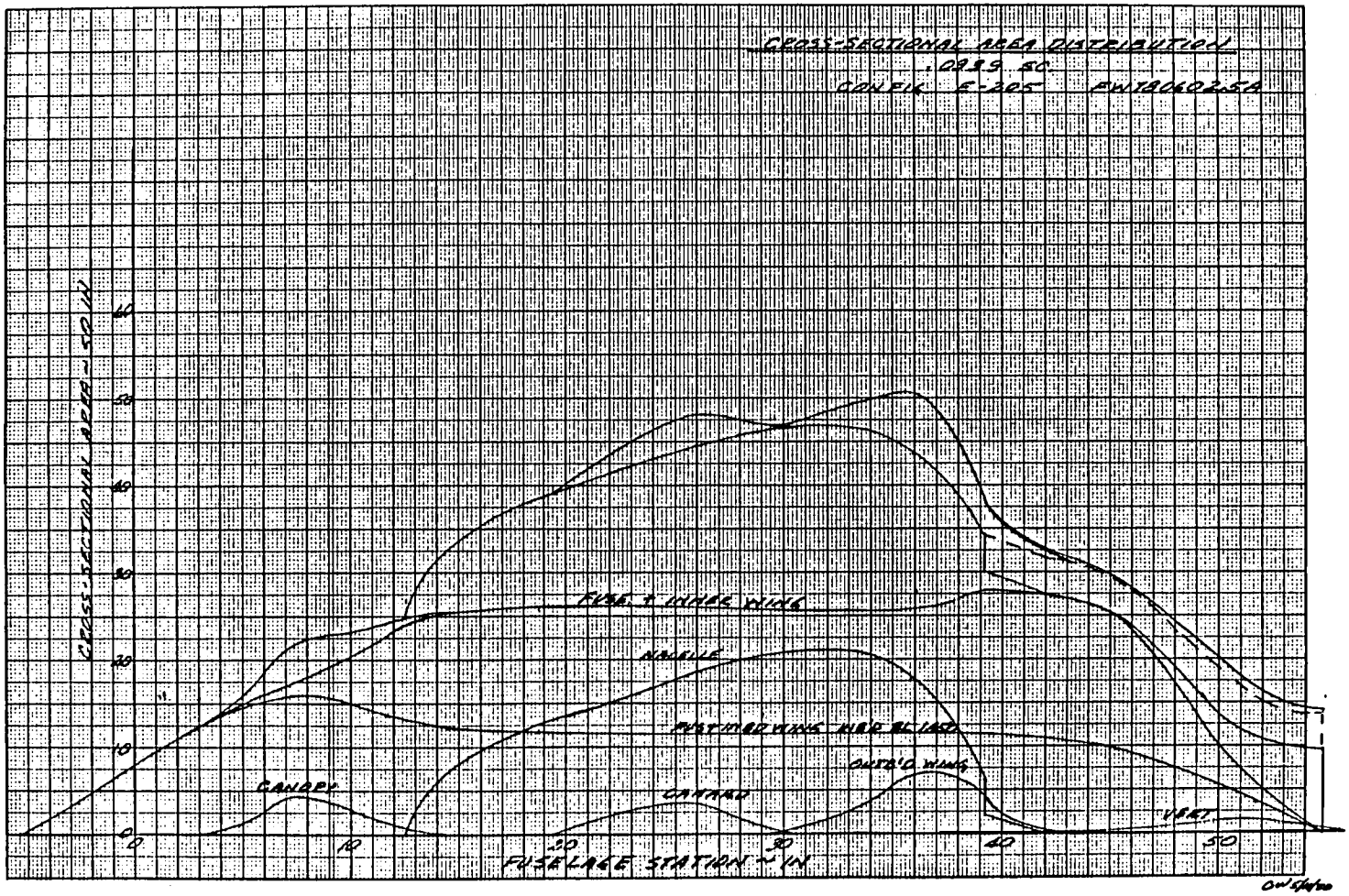

Figure 1-8 E205 Wind Tunnel Model Cross-Sectional Area Distribution

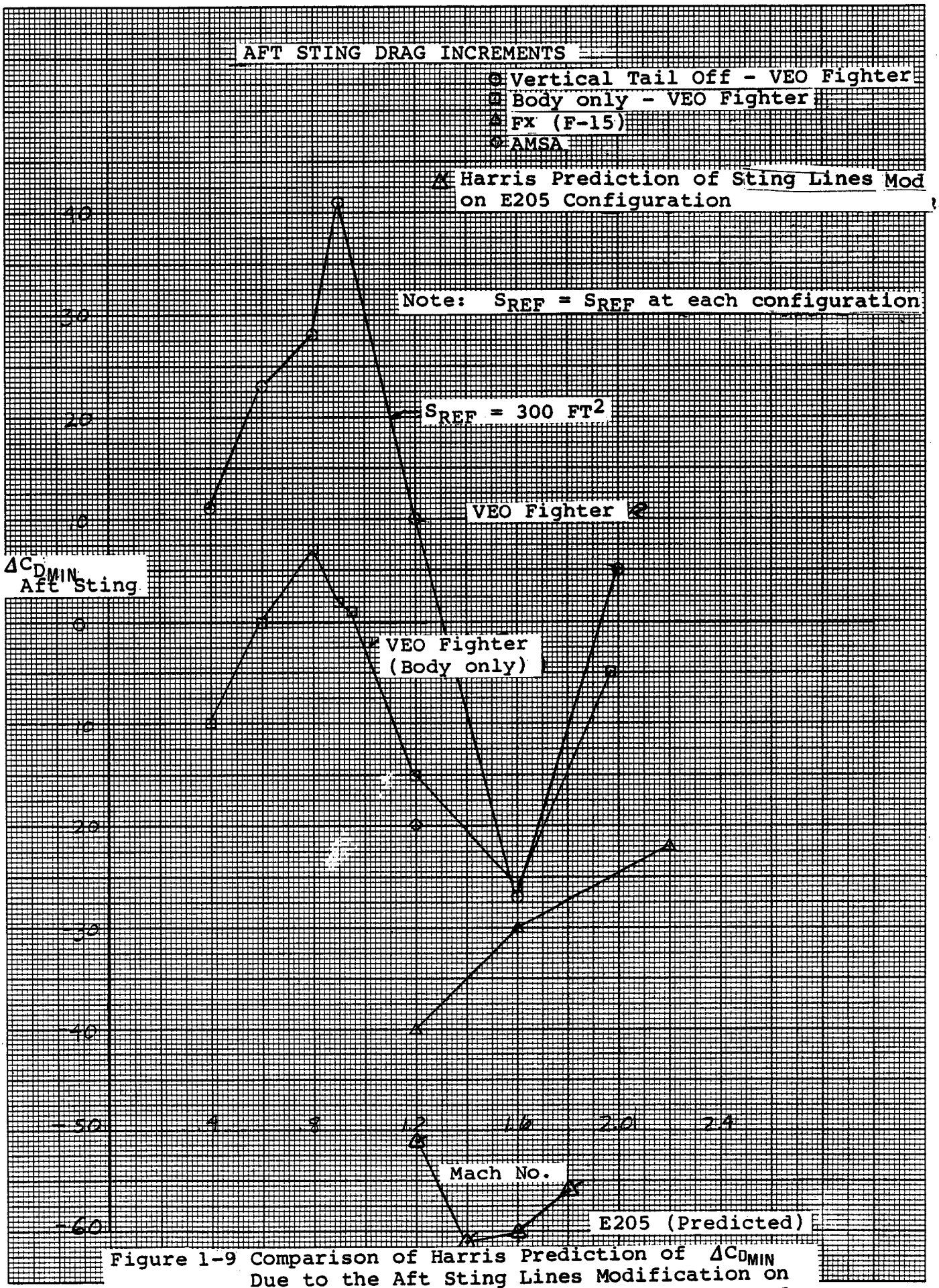

Figure 1-9 Comparison of Harris Prediction of $\Delta C_{D_{MIN}}$ Due to the Aft Sting Lines Modification on the E205 Model with Experimental Results for Other Configurations

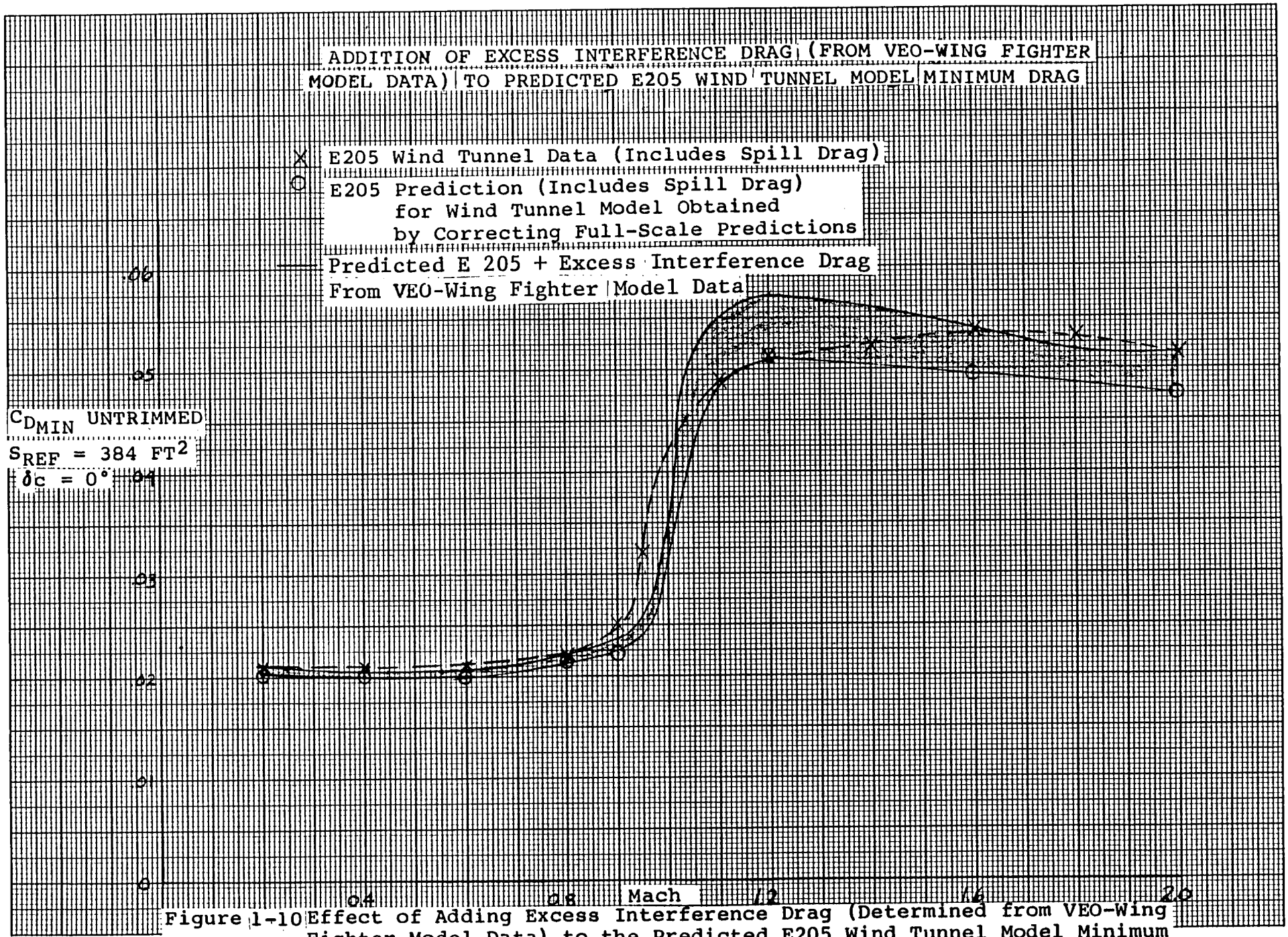

Figure 1-10 Effect of Adding Excess Interference Drag (Determined from VEO-Wing Fighter Model Data) to the Predicted E205 Wind Tunnel Model Minimum Drag

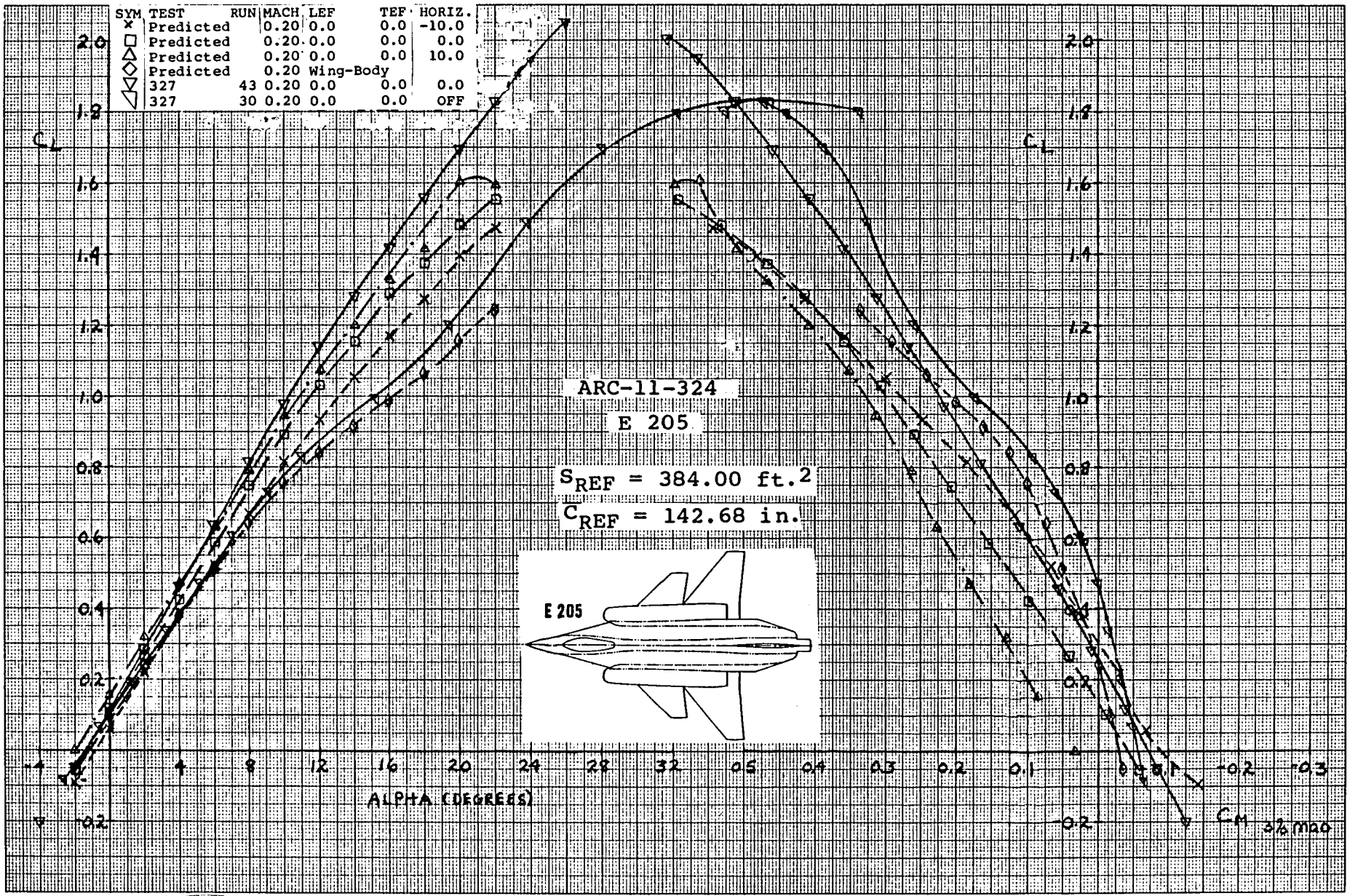

Figure 1-11a Lift and Moment Comparison of Predicted and Test Longitudinal Aerodynamic Characteristics of Baseline E 205 Configuration, Power-Off, Mach = .2

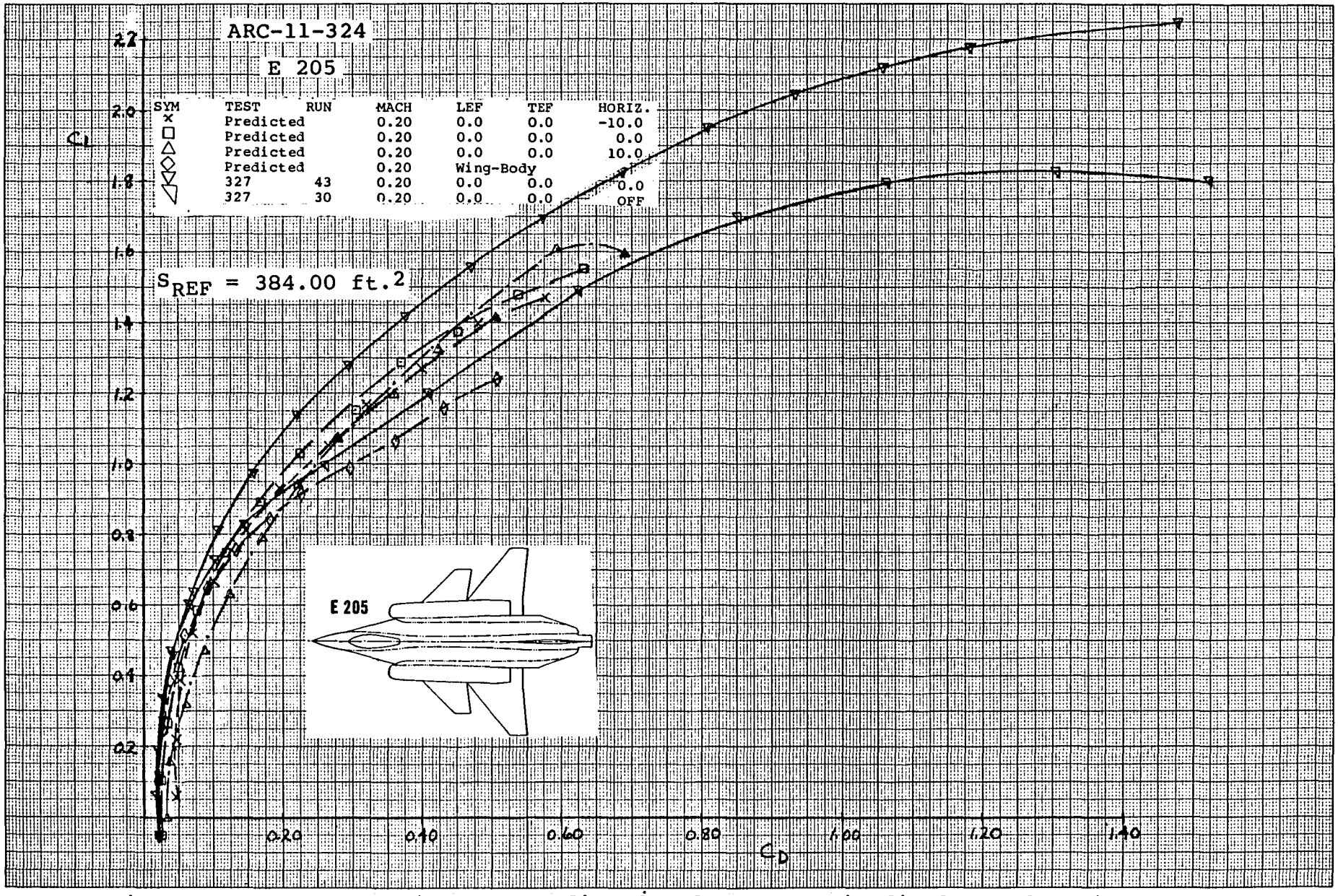

Figure 1-11b Drag Comparison of Predicted and Test Longitudinal Aerodynamic Characteristics of Baseline E 205 Configuration, (Expanded Drag Scale), Power-Off, Mach = .2

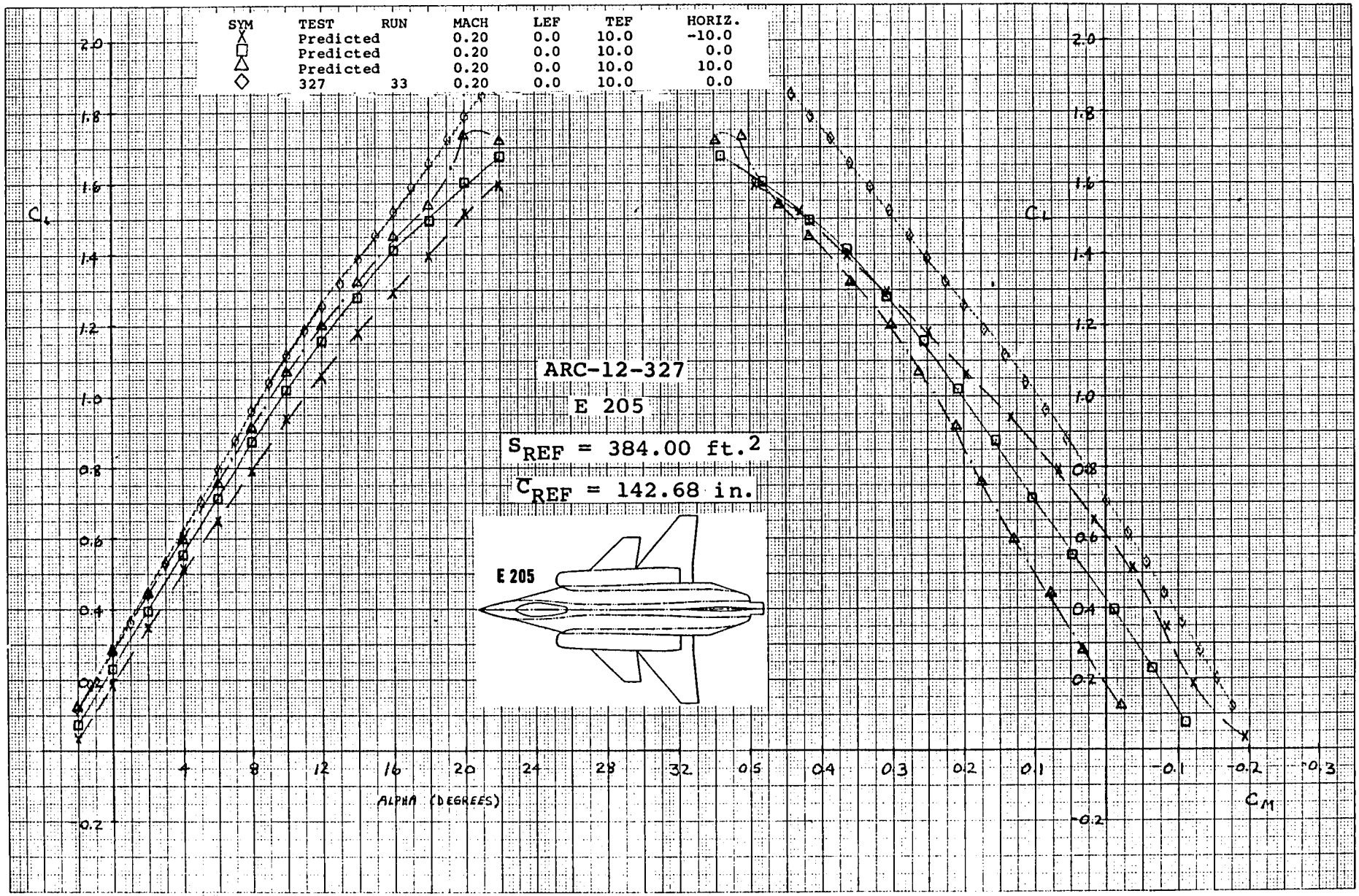

Figurel-12aLift and Moment Comparison of Predicted and Test Longitudinal Aerodynamic Characteristics of Baseline E205 Configuration with Wing Trailing-Edge Flap Deflected +10°, Power-Off, Mach = .2

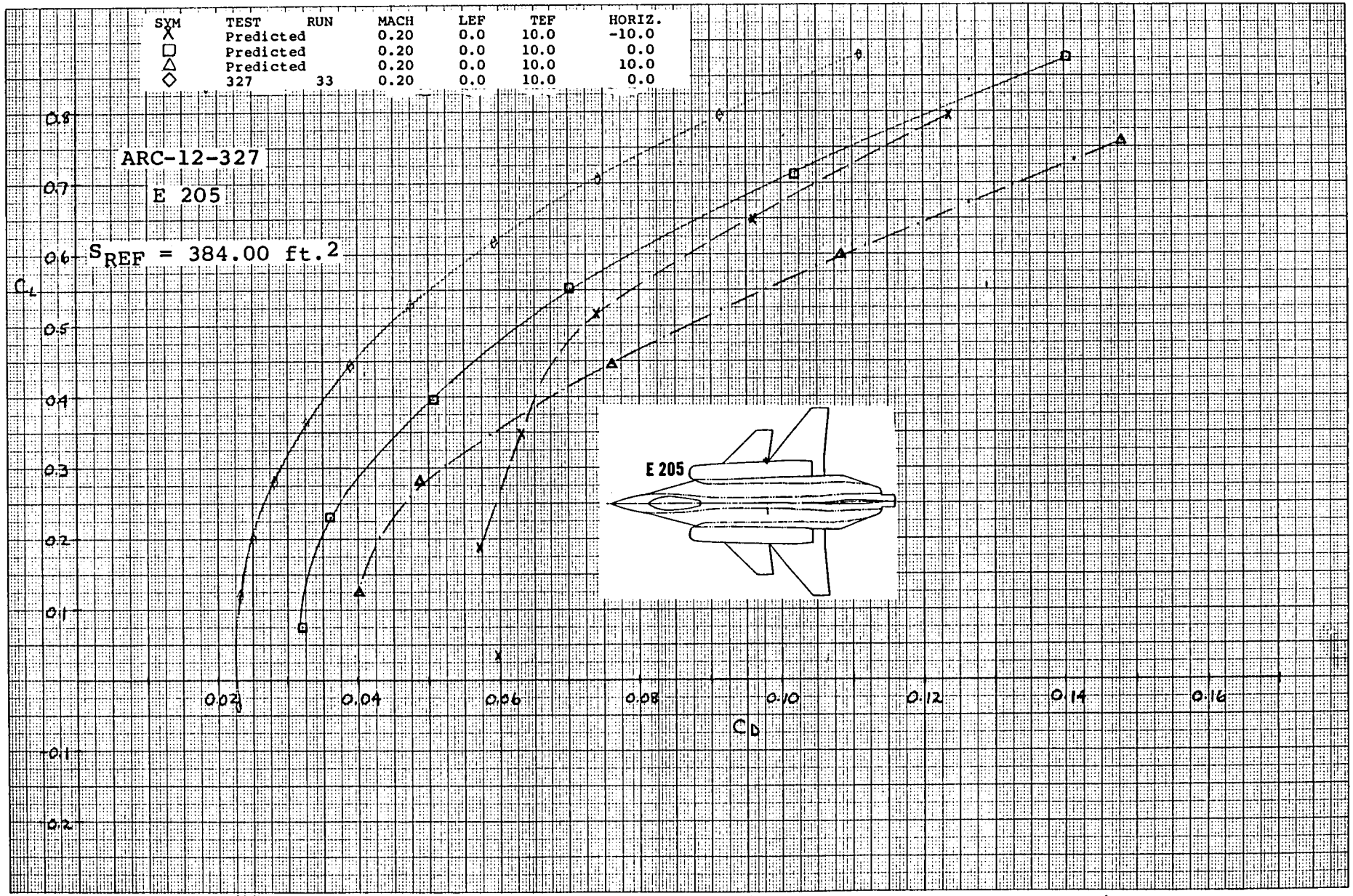

Figurel-12bDrag Comparison of Predicted and Test Longitudinal Aerodynamic Characteristics of Baseline E205 Configuration with Wing Trailing-Edge Flap Deflected +10°, Power- Off, Mach = .2

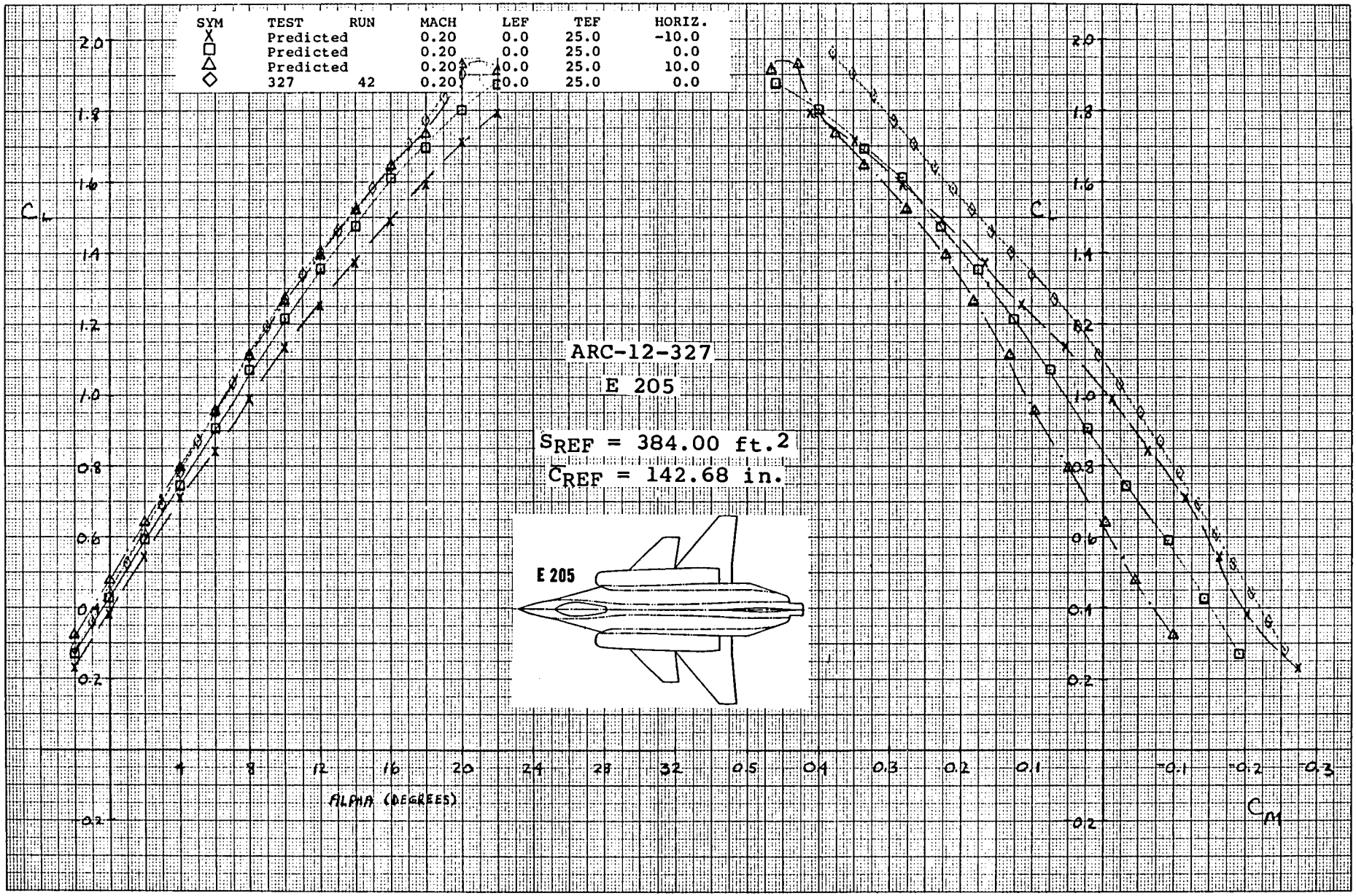

Figurel-13aLift and Moment Comparison of Predicted and Test Longitudinal Aerodynamic Characteristics of Baseline E205 Configuration with Wing Trailing-Edge Flap Deflected +25°, Power-Off, Mach = .2

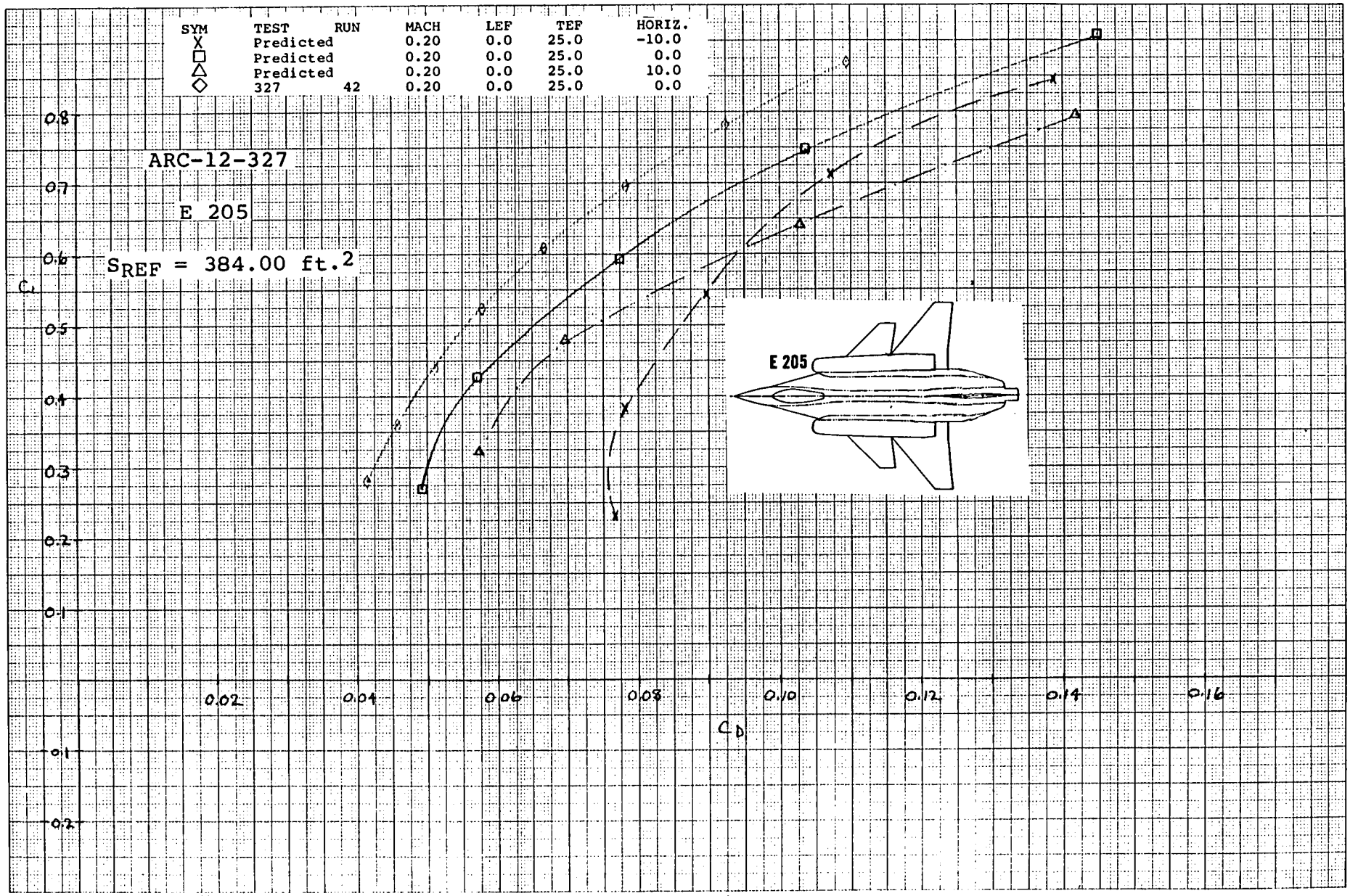

Figurel-13bDrag Comparison of Predicted and Test Longitudinal Aerodynamic Characteristics of Baseline E205 Configuration with Wing Trailing-Edge Flap Deflected +25°, Power-Off, Mach = .2

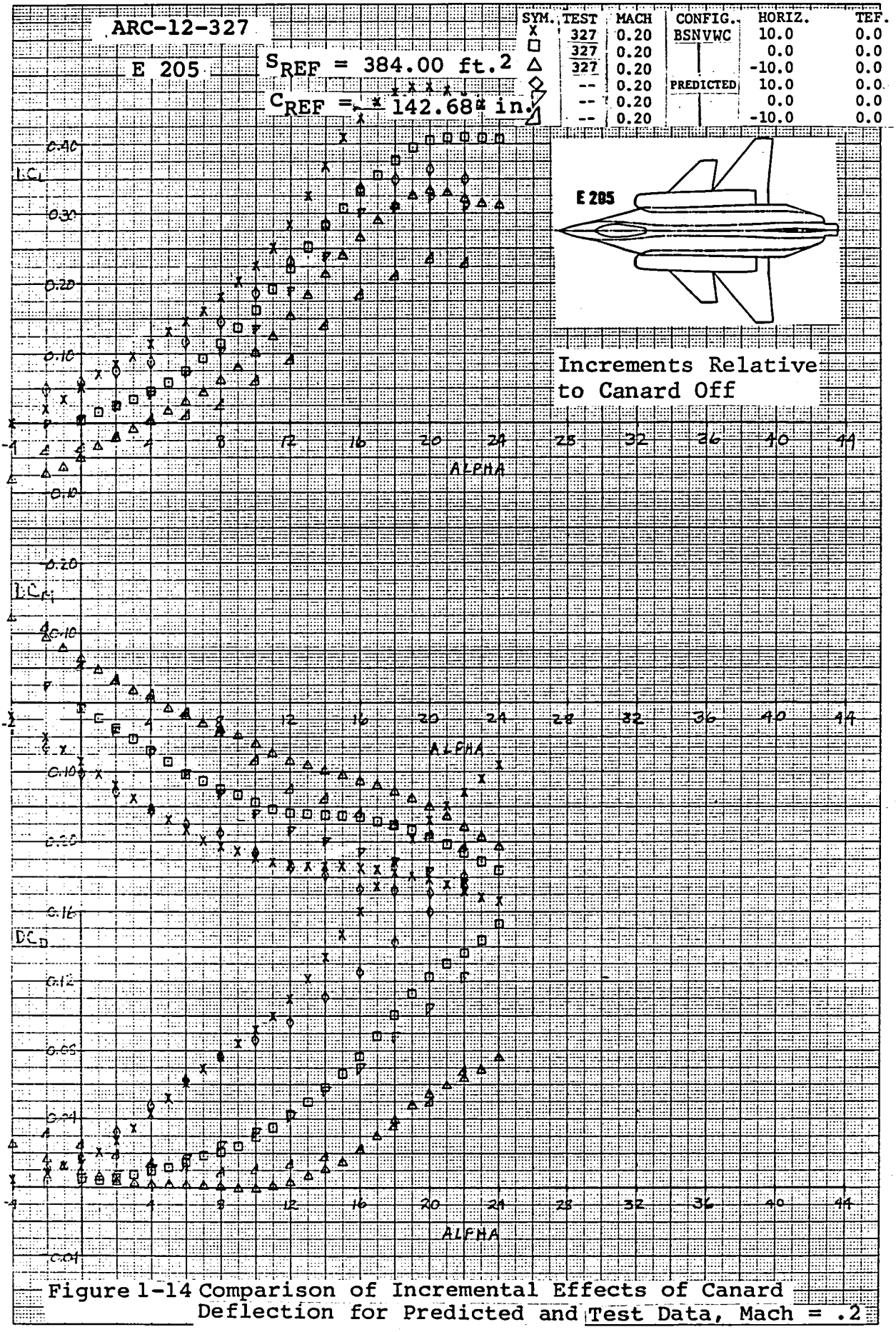

Figure 1-14 Comparison of Incremental Effects of Canard Deflection for Predicted and Test Data, Mach = .2

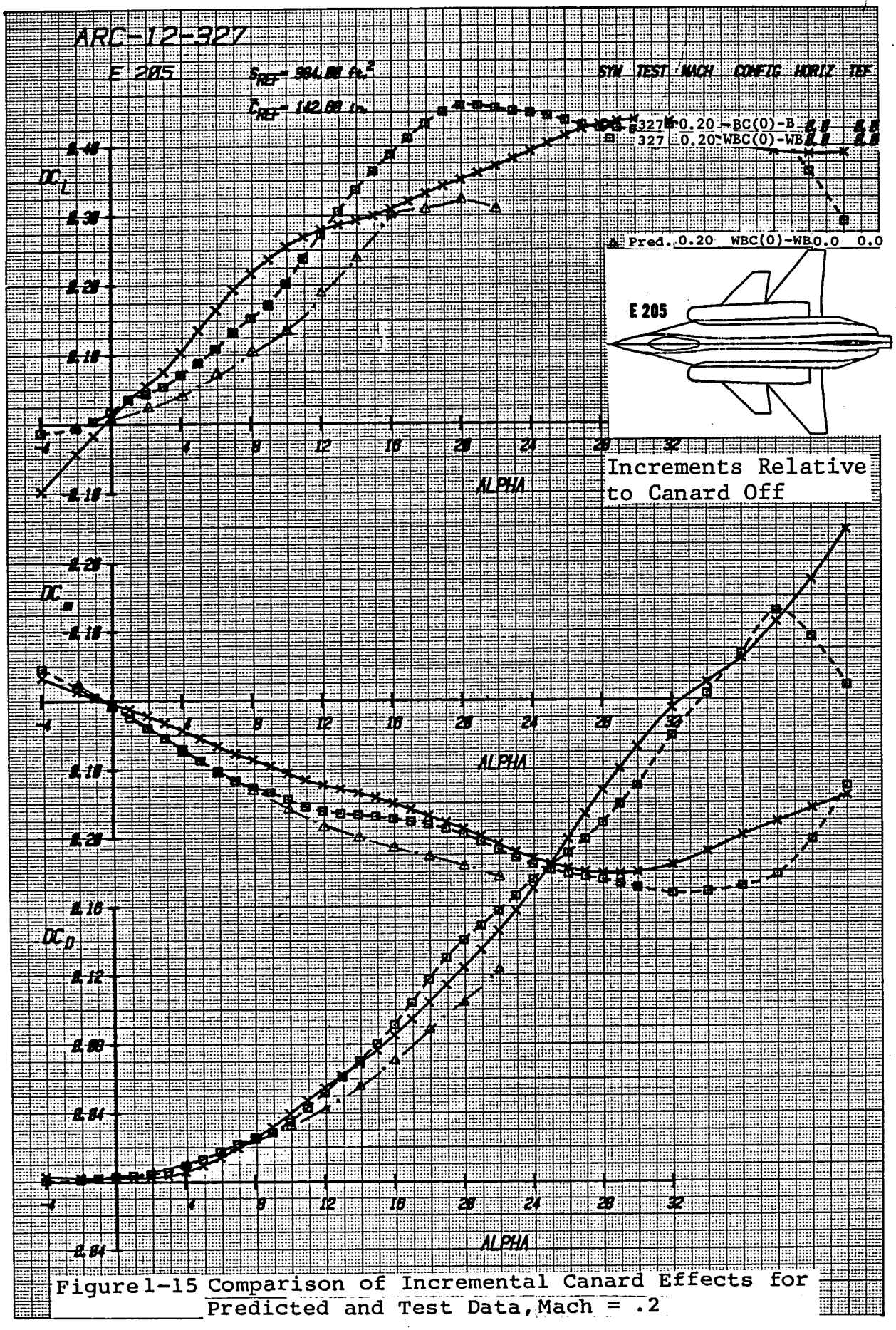

Figure 1-15 Comparison of Incremental Canard Effects for Predicted and Test Data, Mach = .2

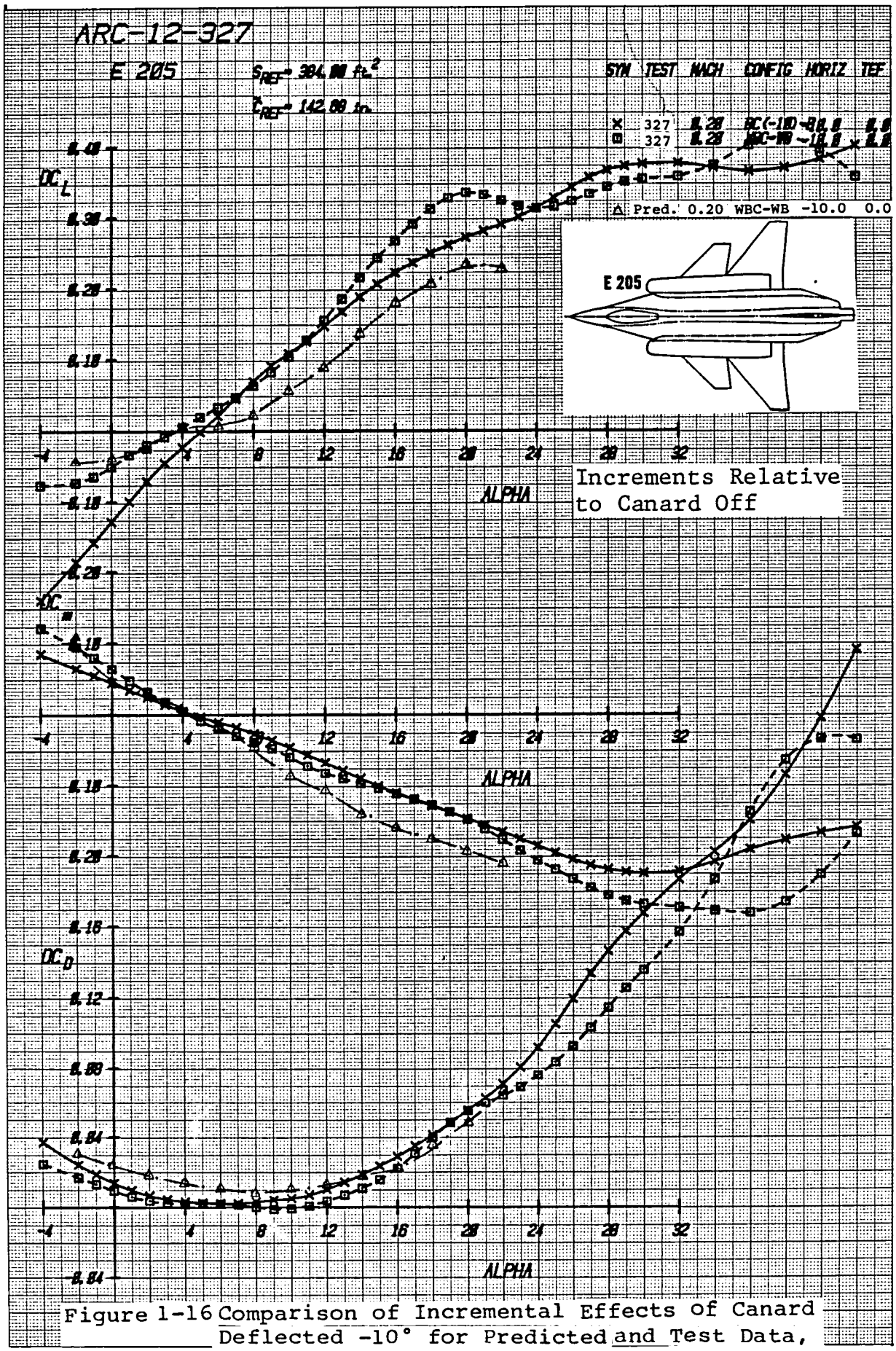

Figure 1-16 Comparison of Incremental Effects of Canard Deflected -10° for Predicted and Test Data, Mach = .2

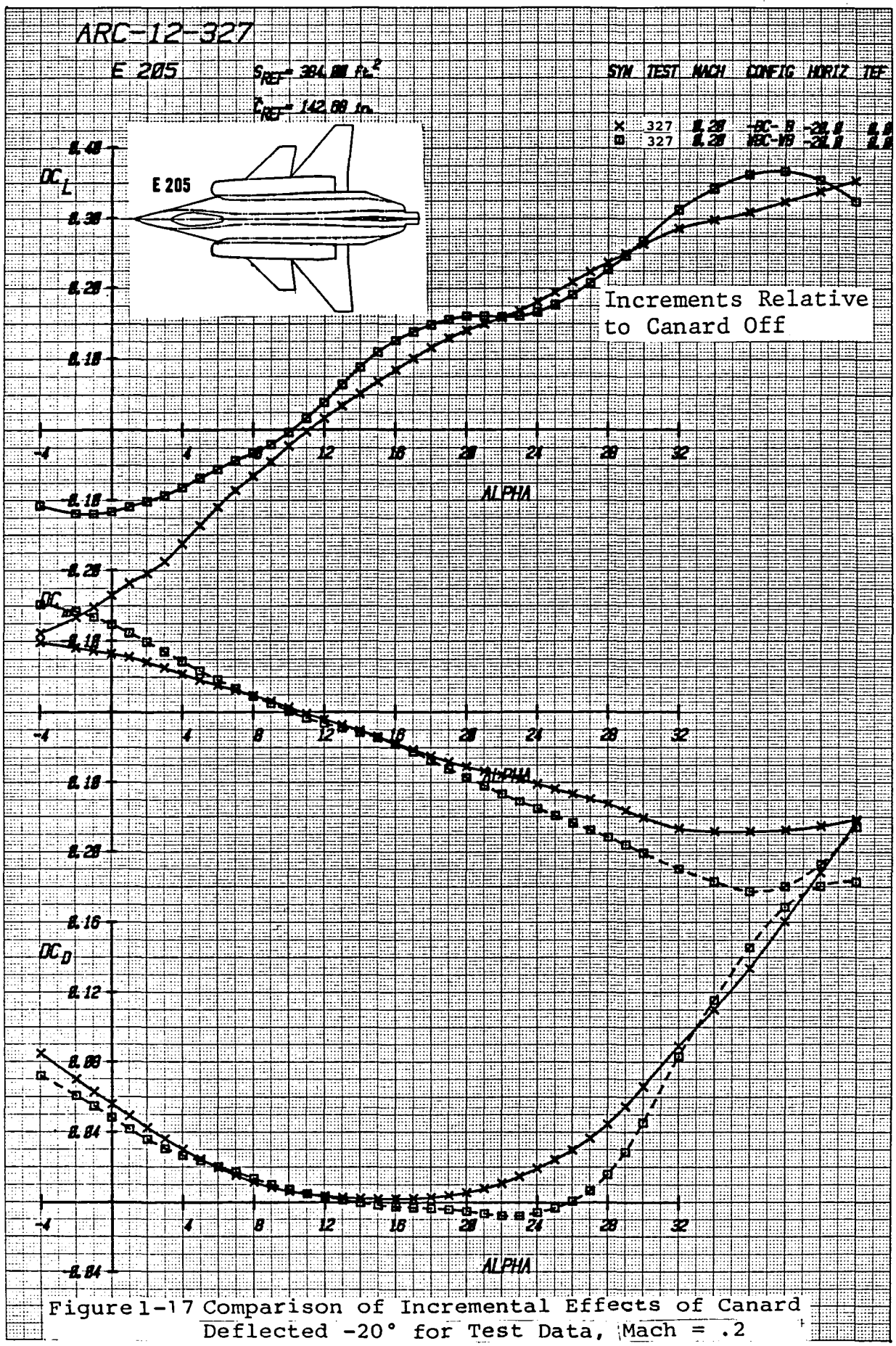

Figure 1-17 Comparison of Incremental Effects of Canard Deflected -20° for Test Data, Mach = .2

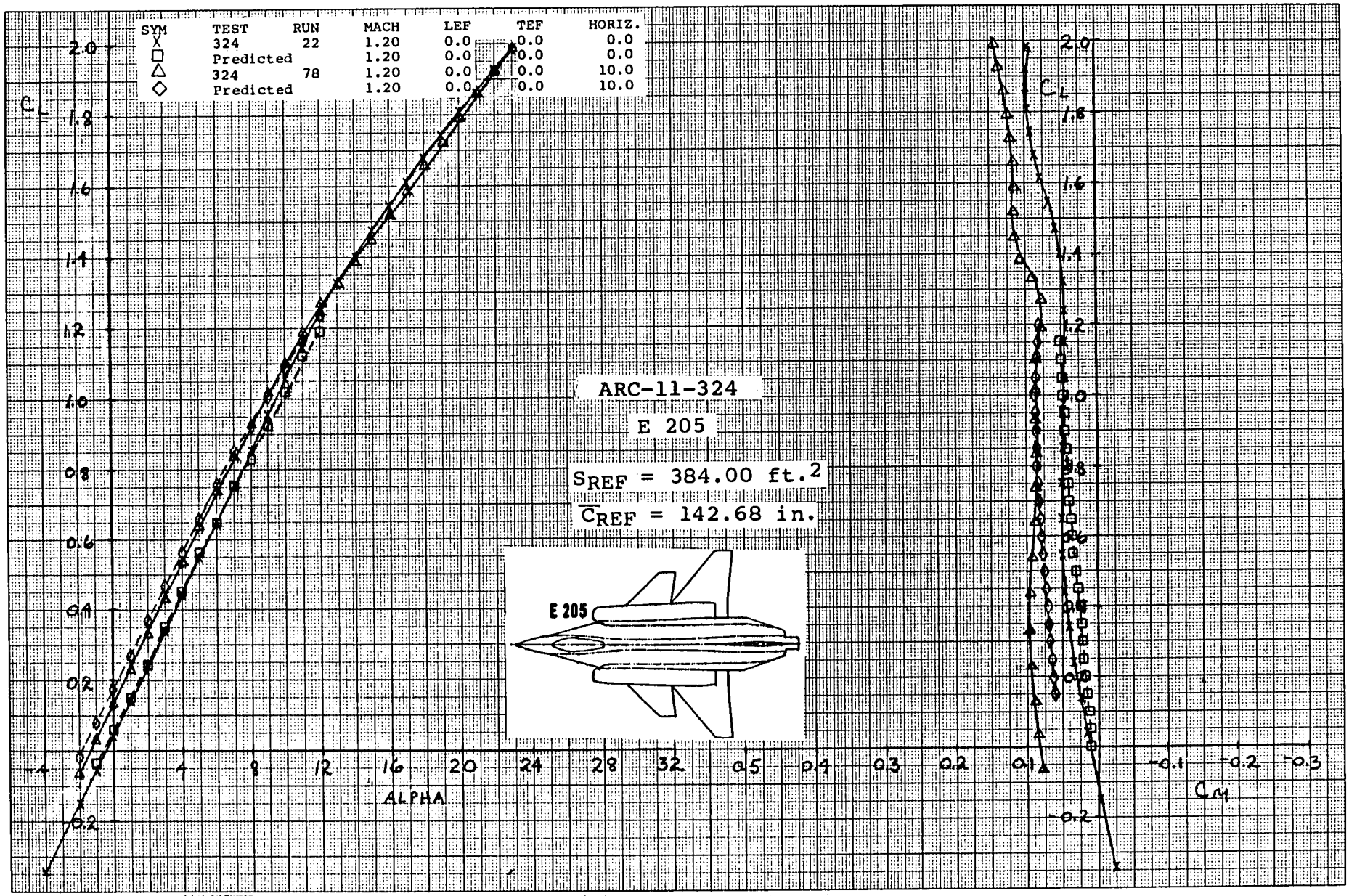

Figure1-18aLift and Moment Comparison of Predicted and Test Longitudinal Aerodynamic Characteristics of Baseline E 205 Configuration, Power-Off, Mach = 1.2

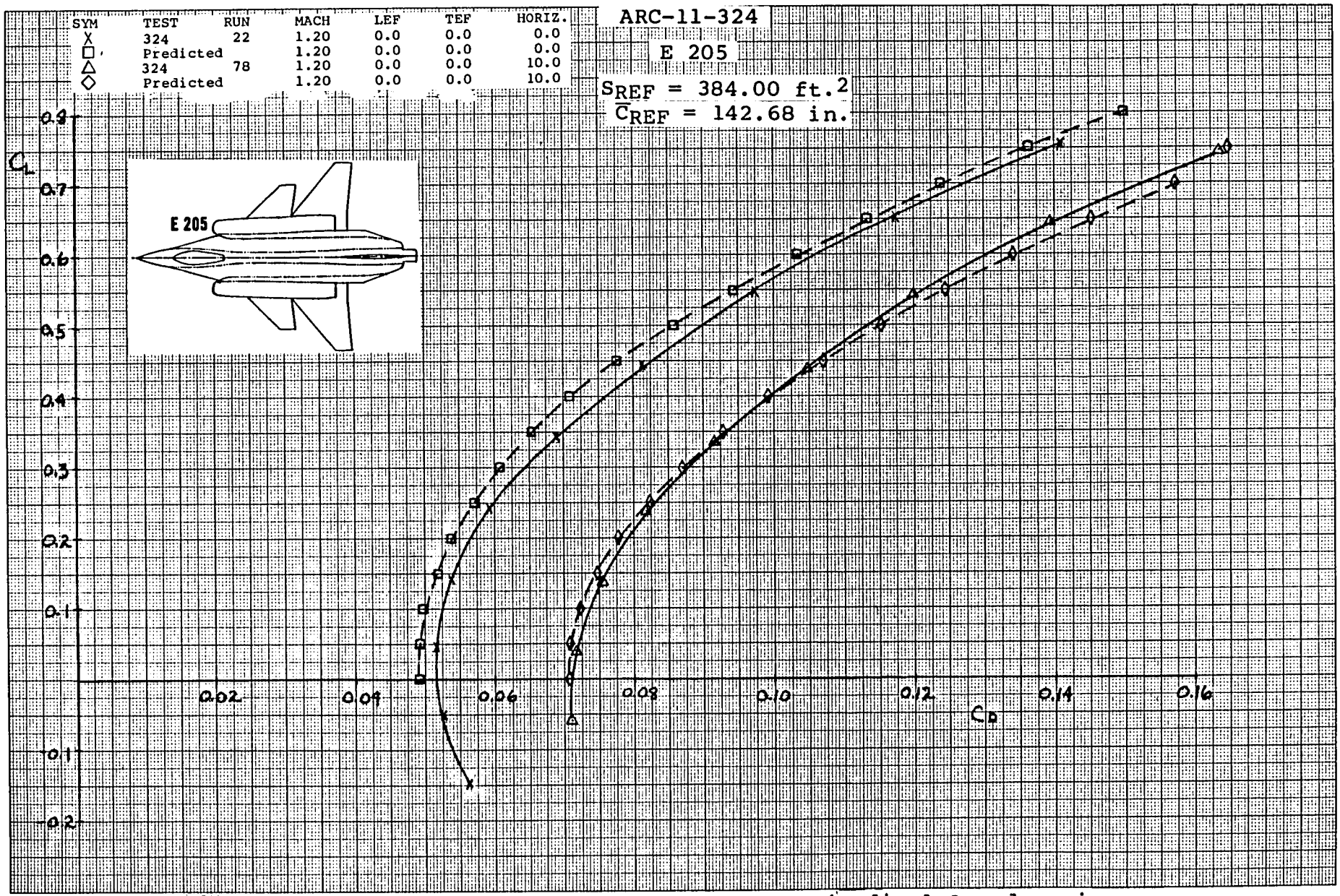

Figurel-18bDrag Comparison of Predicted and Test Longitudinal Aerodynamic Characteristics of Baseline E 205 Configuration, Power-Off, Mach = 1.2

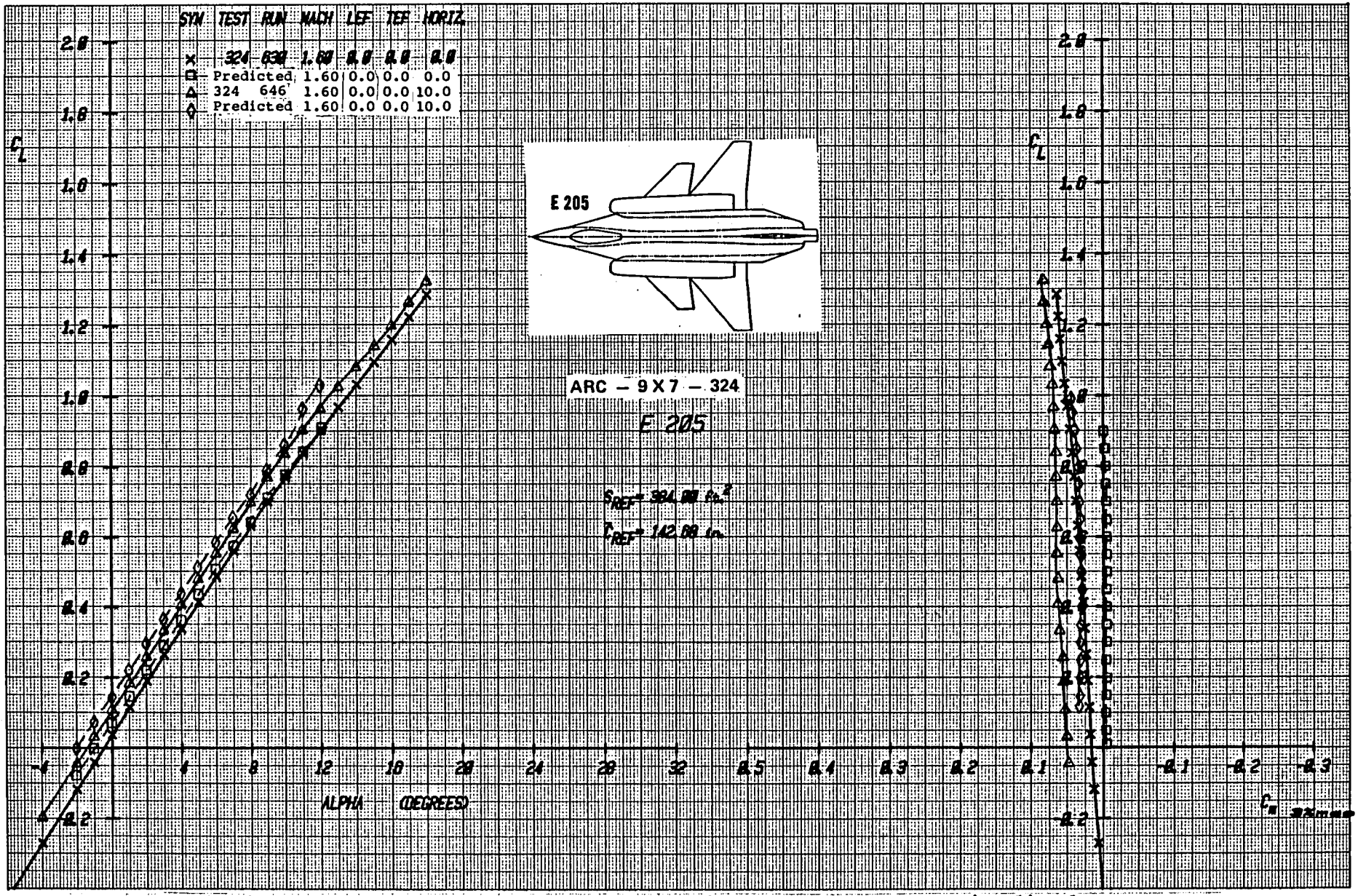

Figurel-19aLift and Moment Comparison of Predicted and Test Longitudinal Aerodynamic Characteristics of Baseline E 205 Configuration, Power-Off, Mach = 1.6

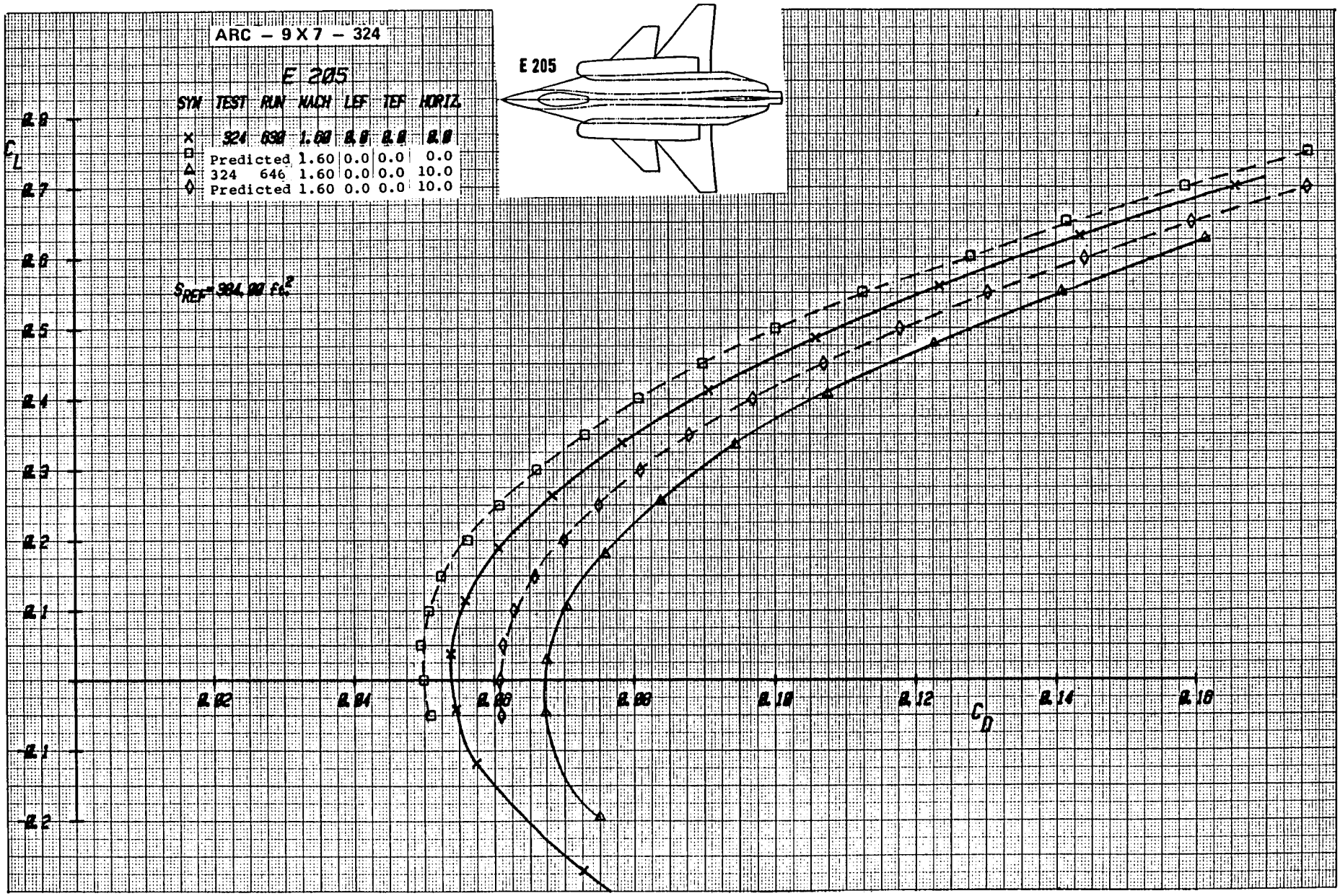

Figurel-19bDrag Comparison of Predicted and Test Longitudinal Aerodynamic Characteristics of Baseline E 205 Configuration, Power-Off, Mach = 1.6

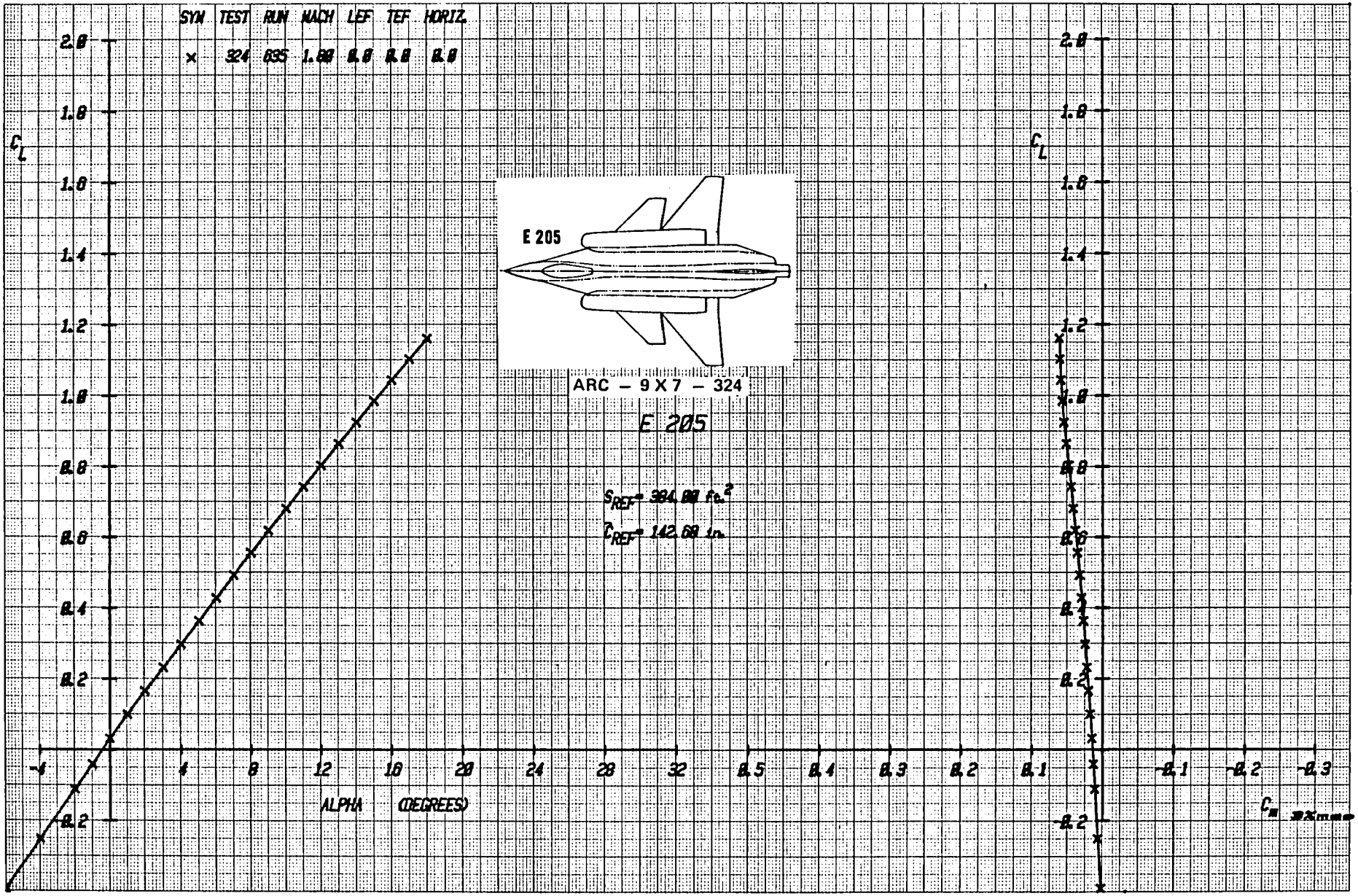

Figurel-20aLift and Moment Data for Baseline E205 Configuration, Mach = 1.8

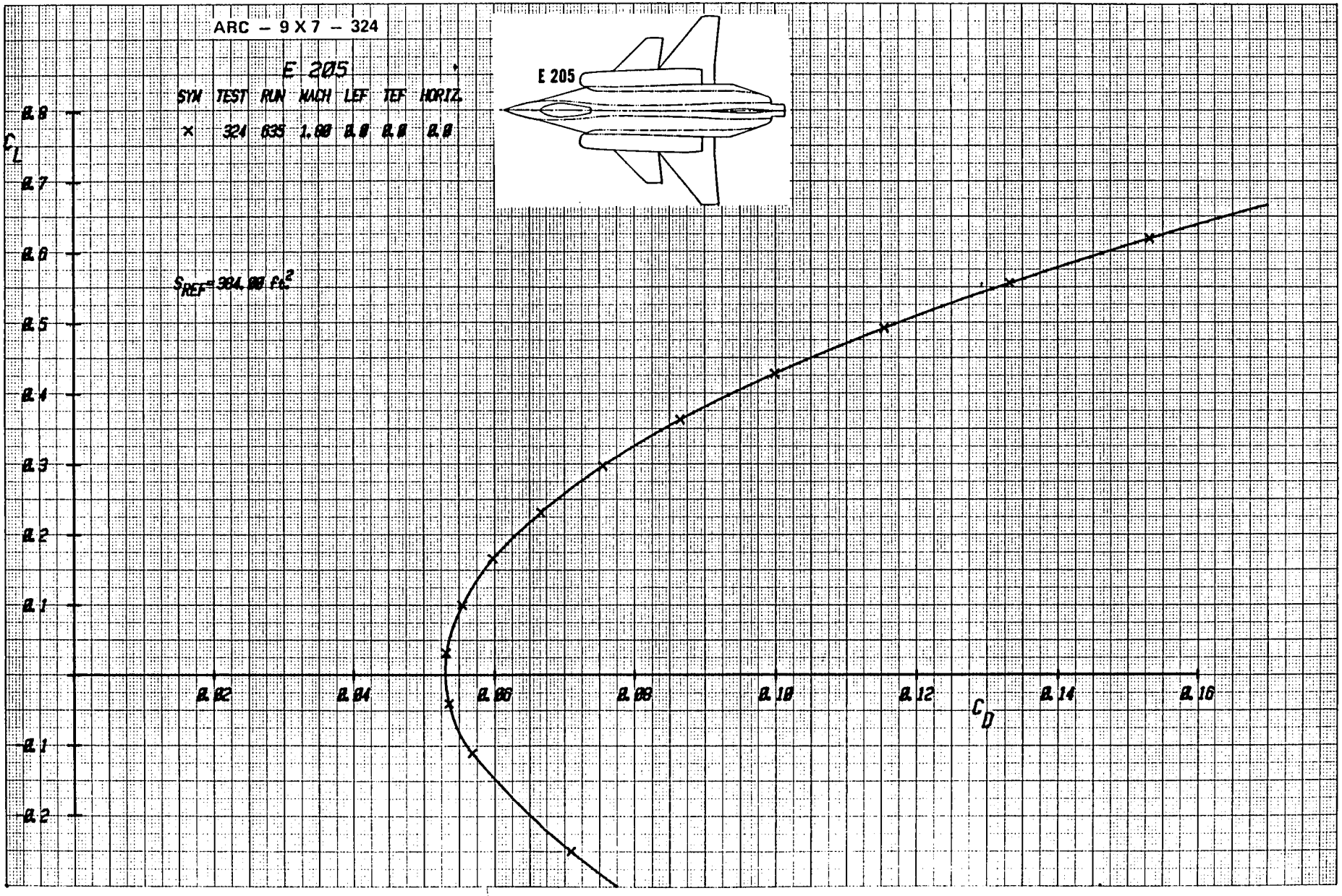

Figurel-20bDrag Data for Baseline E205 Configuration, (Expanded Drag Scale), Mach = 1.8

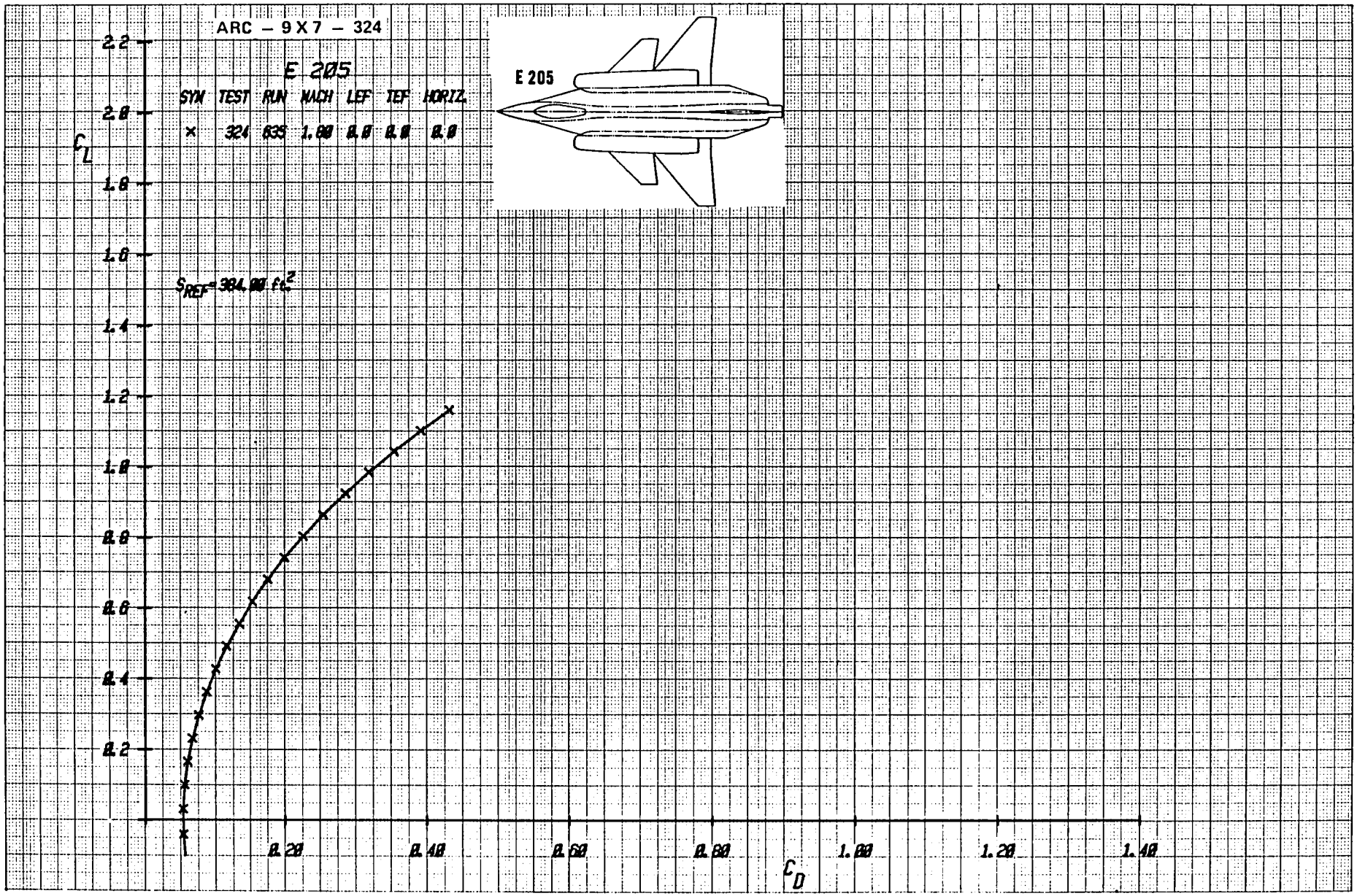

Figurel-20cDrag Data for Baseline E205 Configuration, Mach = 1.8

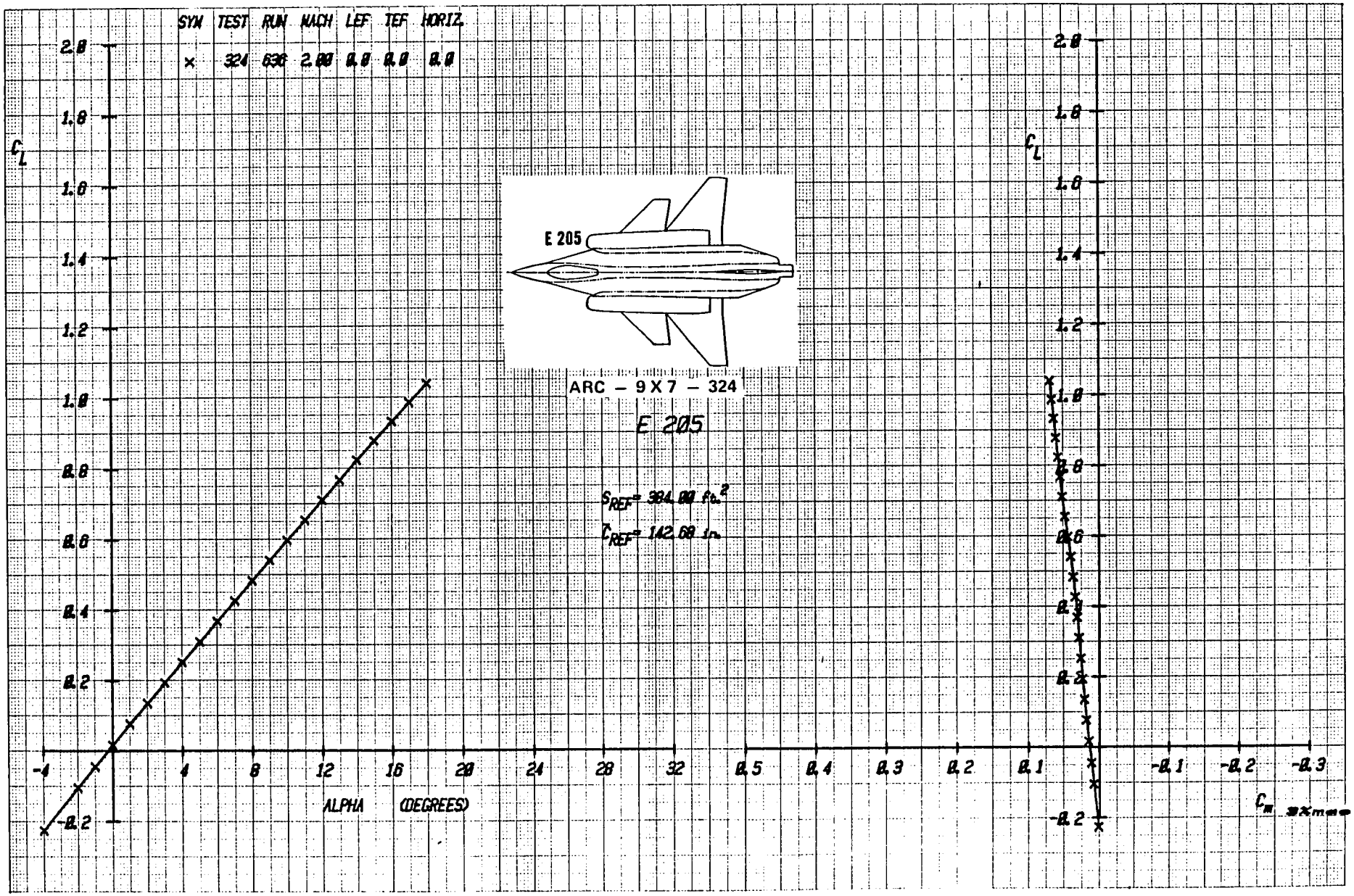

Figurel-21aLift and Moment Data for Baseline E205 Configuration, Mach = 2.0

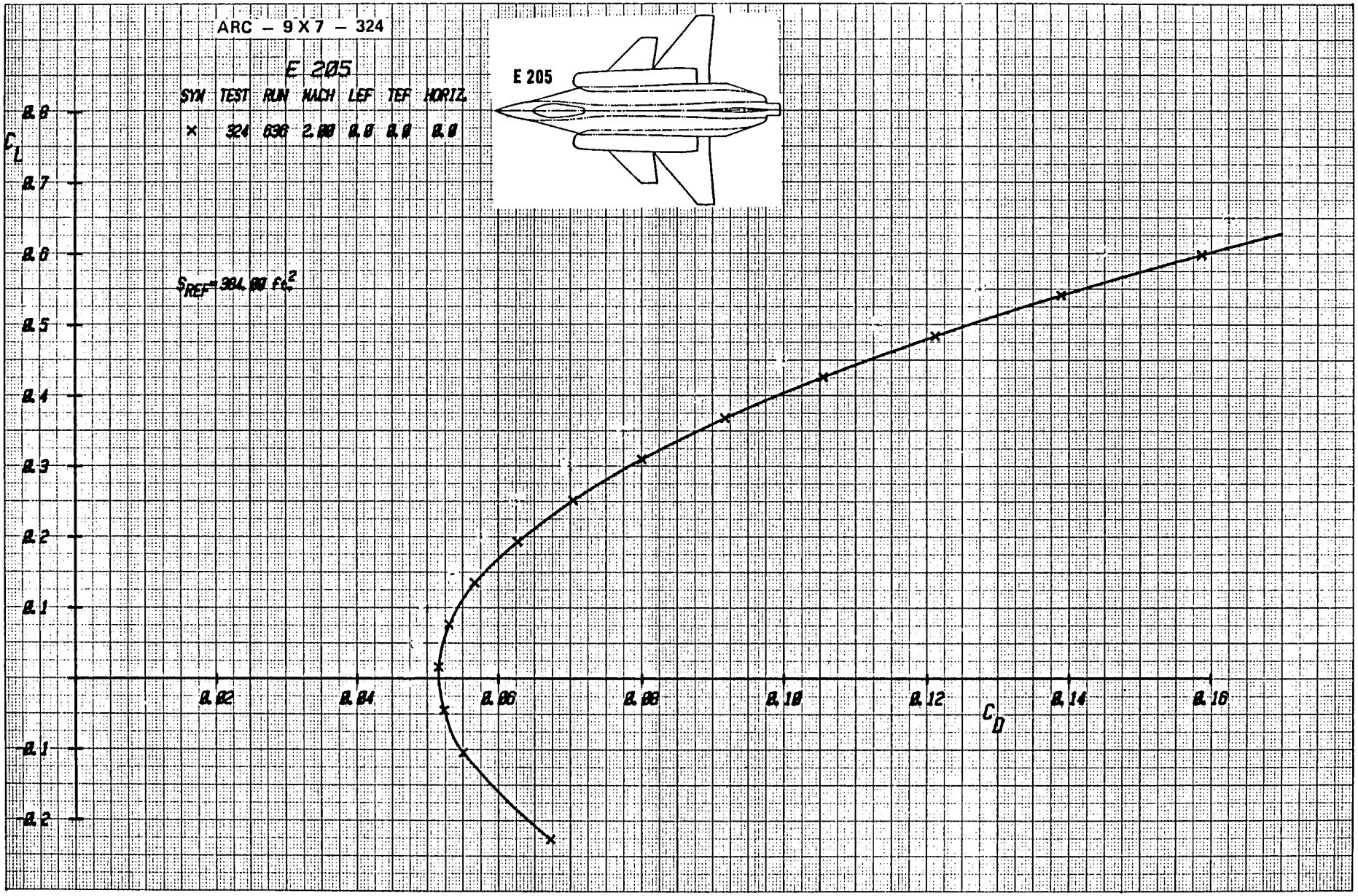

Figurel-21bDrag Data for Baseline E205 Configuration, (Expanded Drag Scale), Mach = 2.0

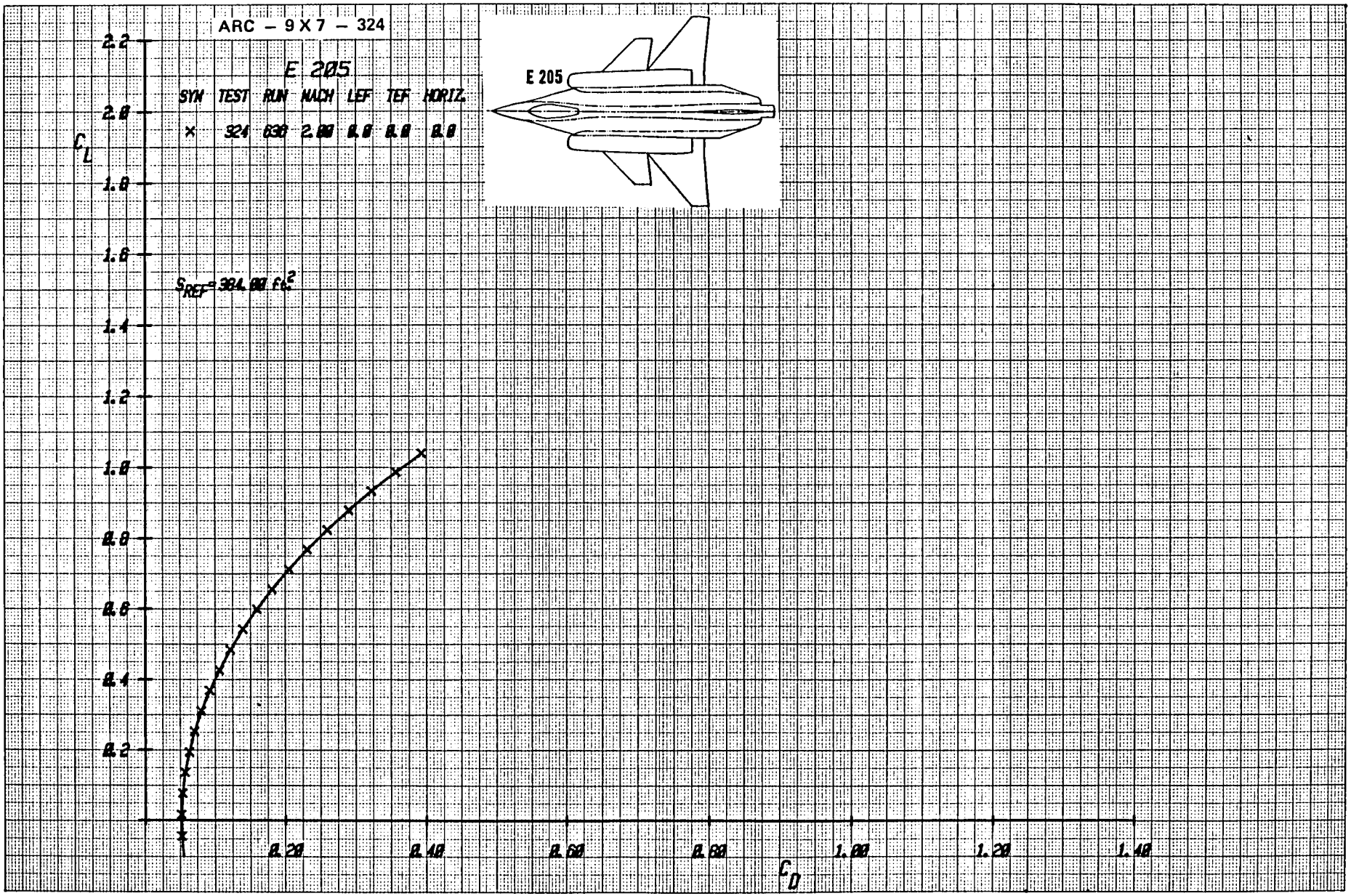

Figurel-21cDrag Data for Baseline E205 Configuration, Mach = 2.0

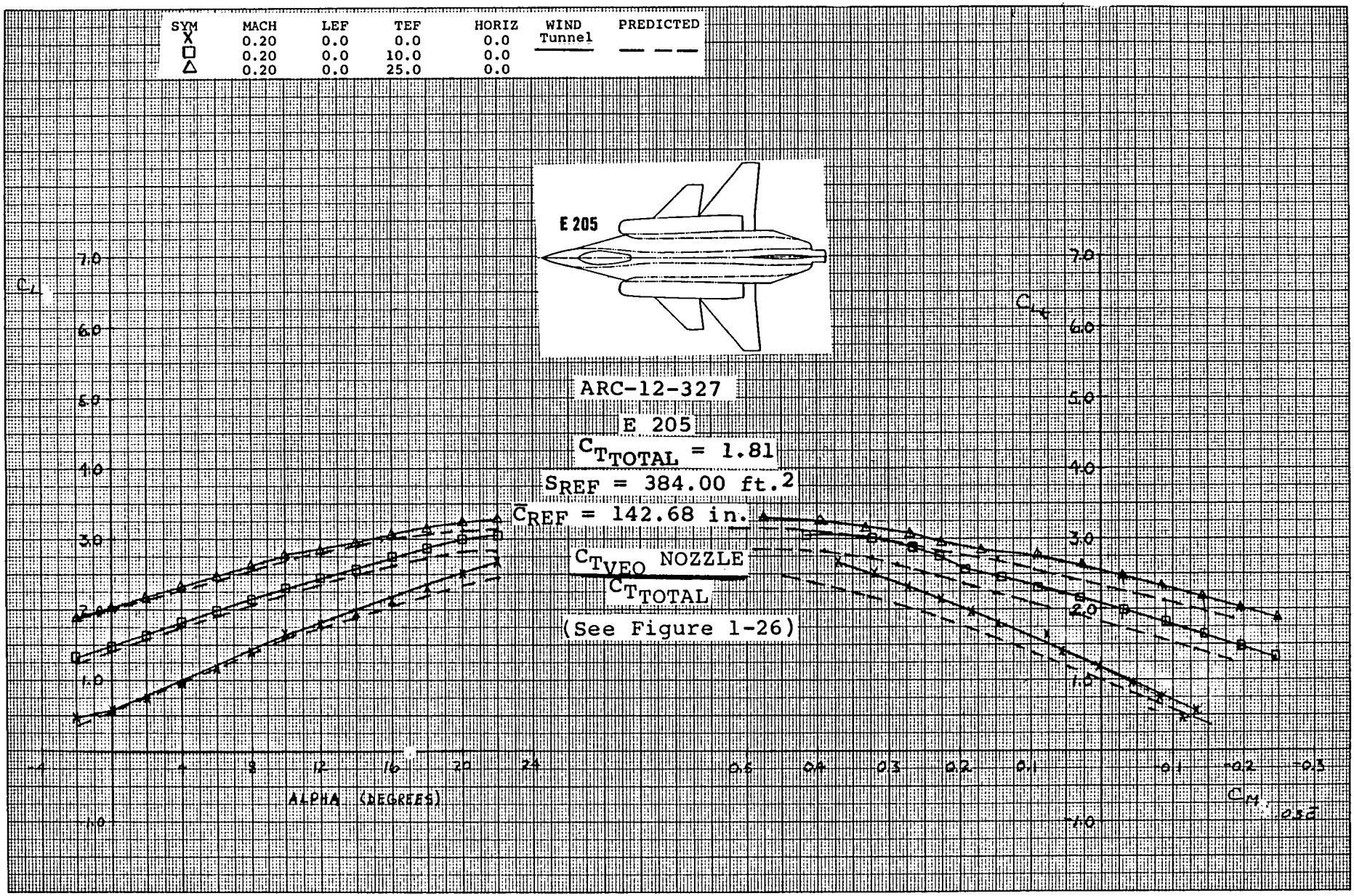

Figure1-22aEffect of Wing Trailing-Edge Flap Deflection on Lift and Moment for Test and Predicted Data, Mach = .2

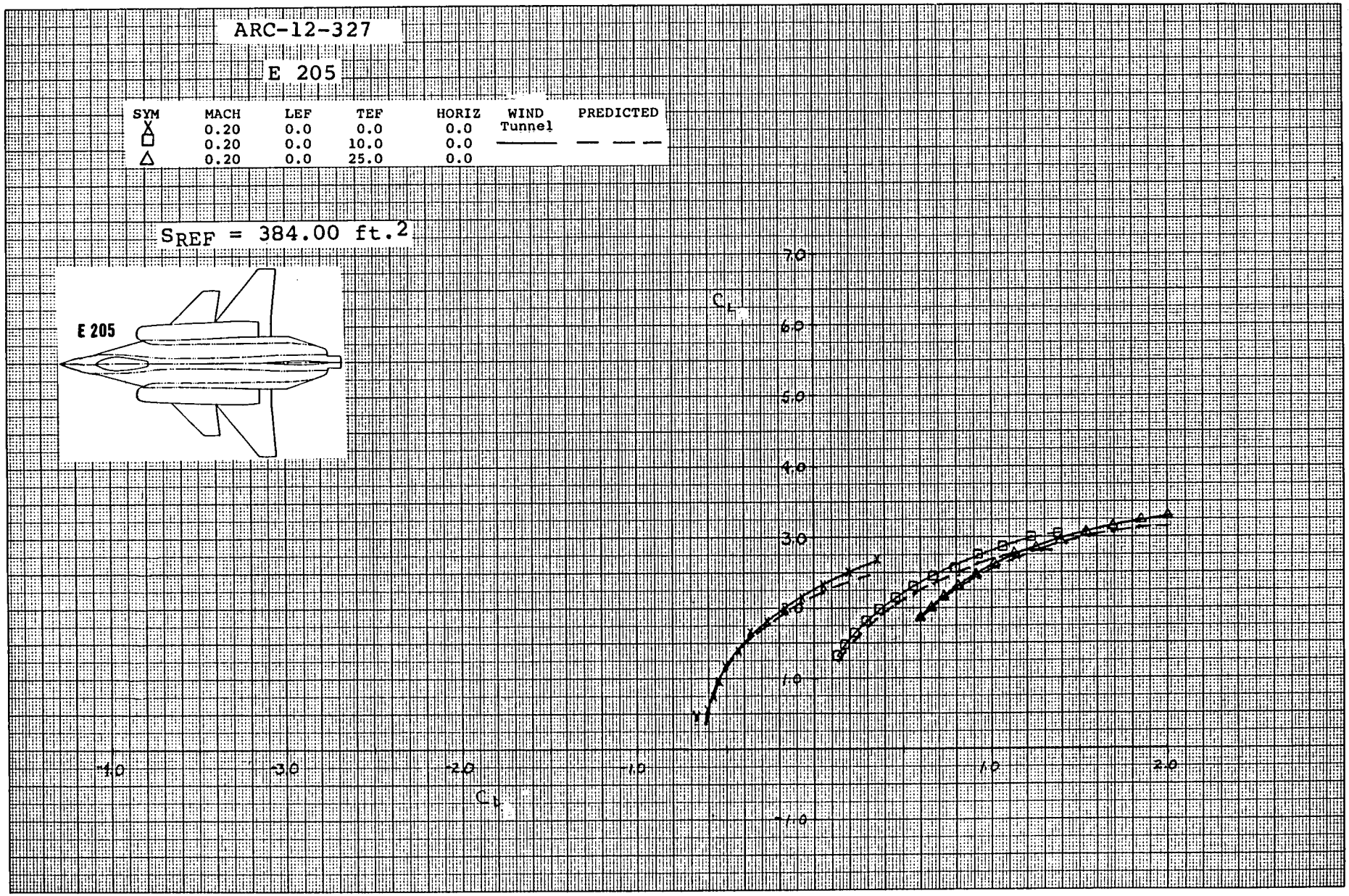

Figurel-22bEffect of Wing Trailing-Edge Flap Deflection on Drag for Test and Predicted Data, Mach = .2

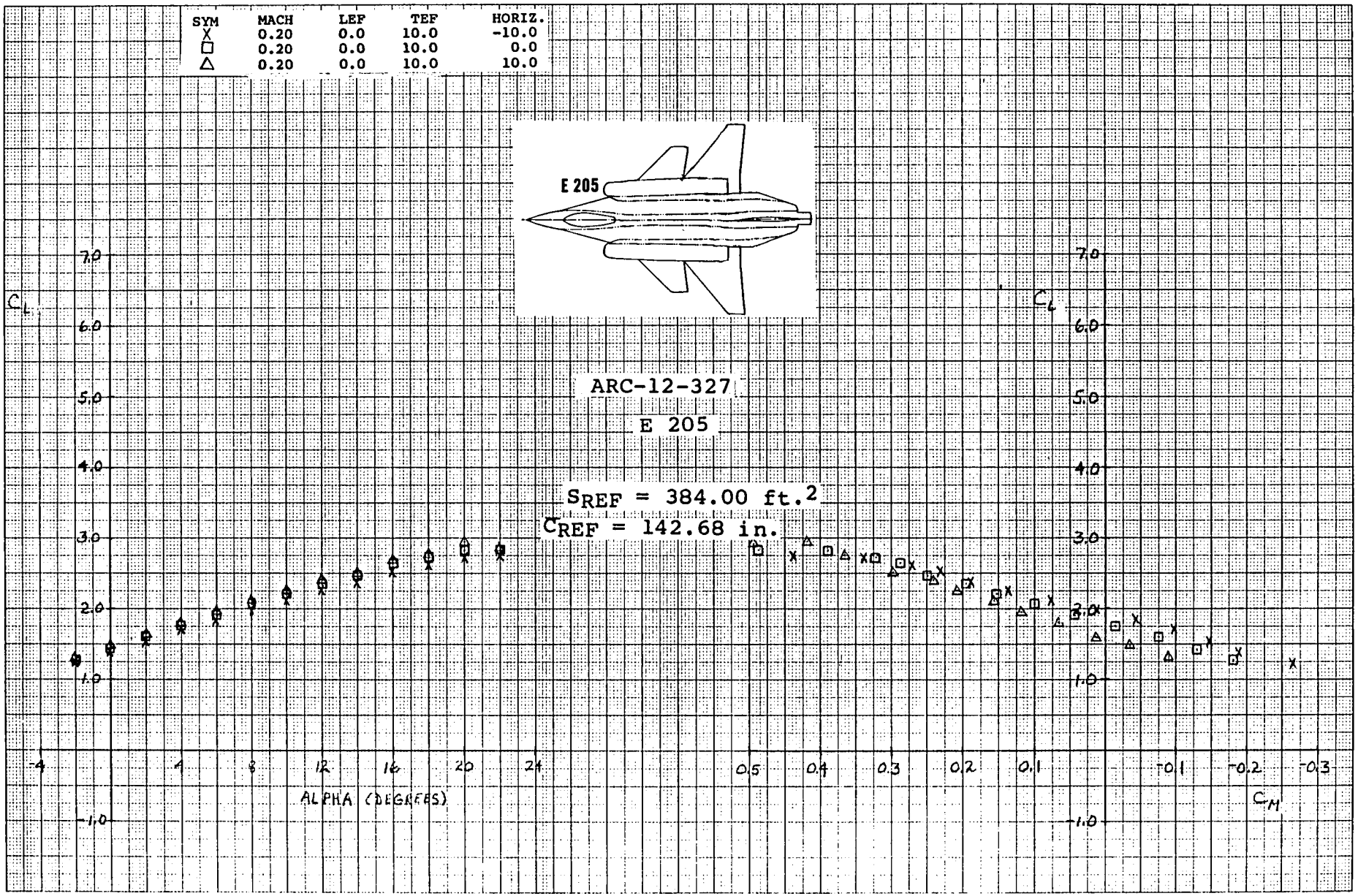

Figure1-23aLift and Moment Predicted Data with Canard Deflections and Wing Trailing-Edge Flap Deflected +10°, Mach = .2 .

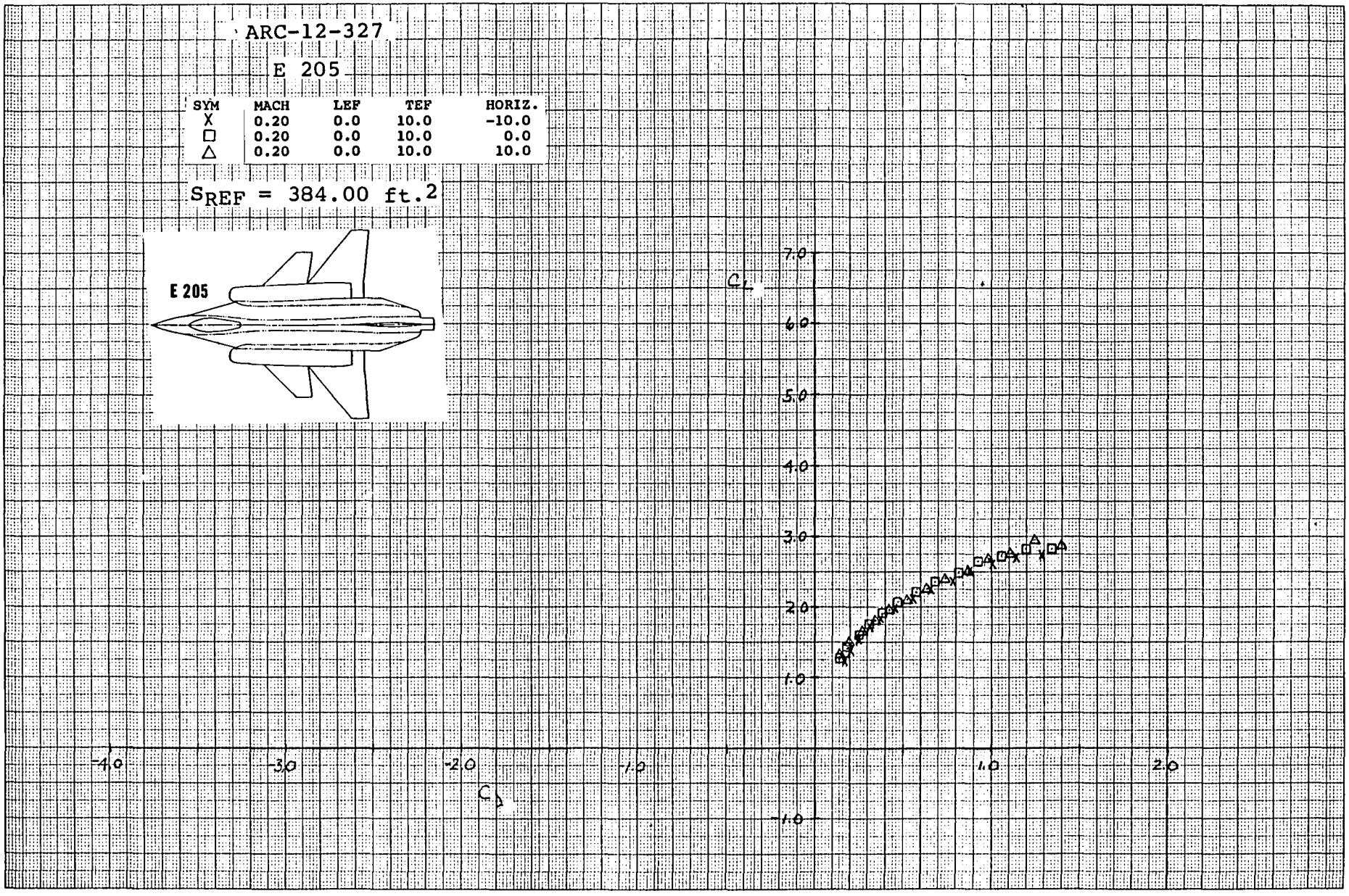

Figurel-23bDrag Predicted Data with Canard Deflections and Wing Trailing-Edge Flap Deflected +10°, Mach = .2

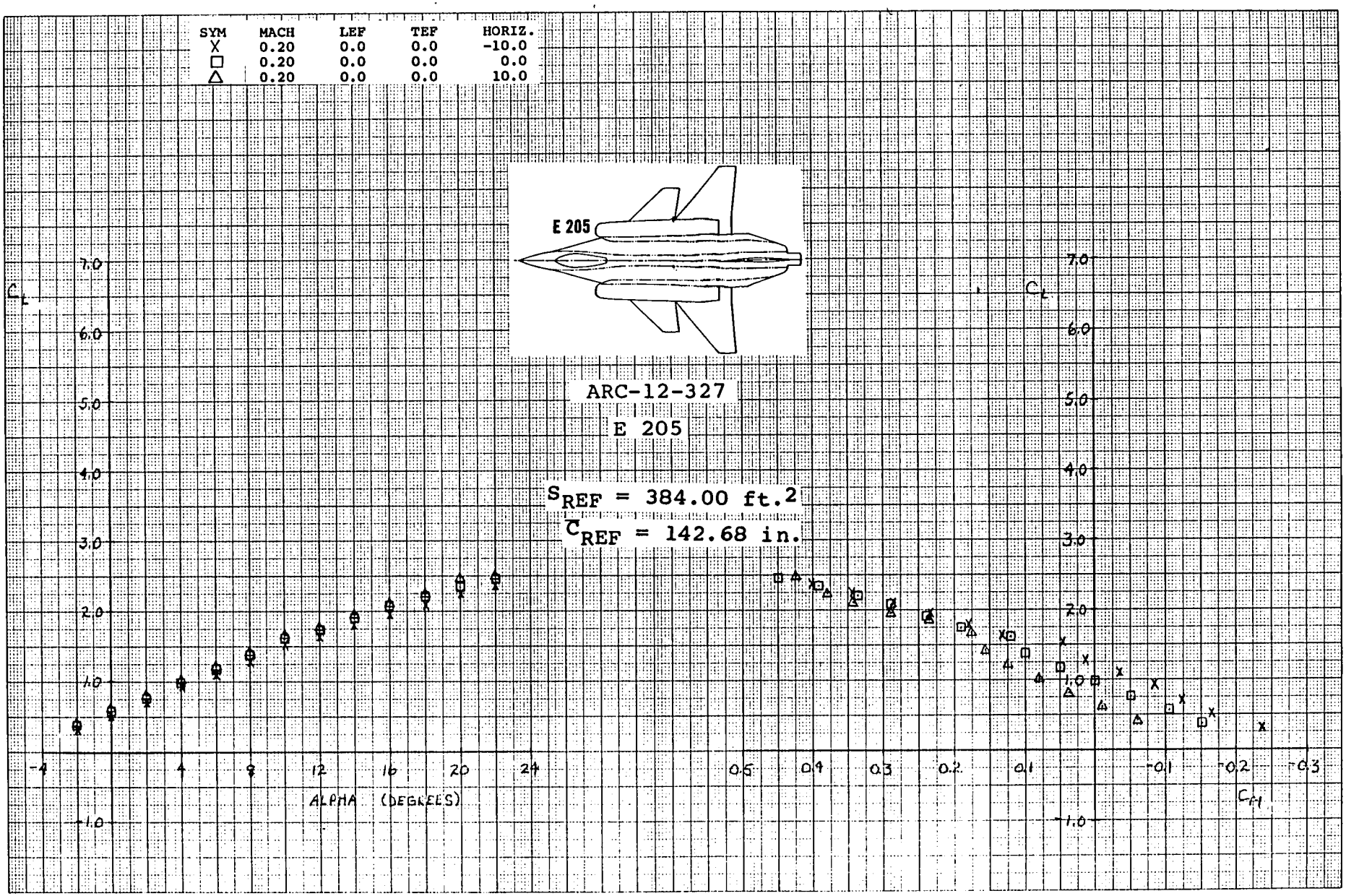

Figure1-24aLift and Moment Predicted Data with Canard Deflections and Wing Trailing-Edge Flap Undeflected, Mach = .2

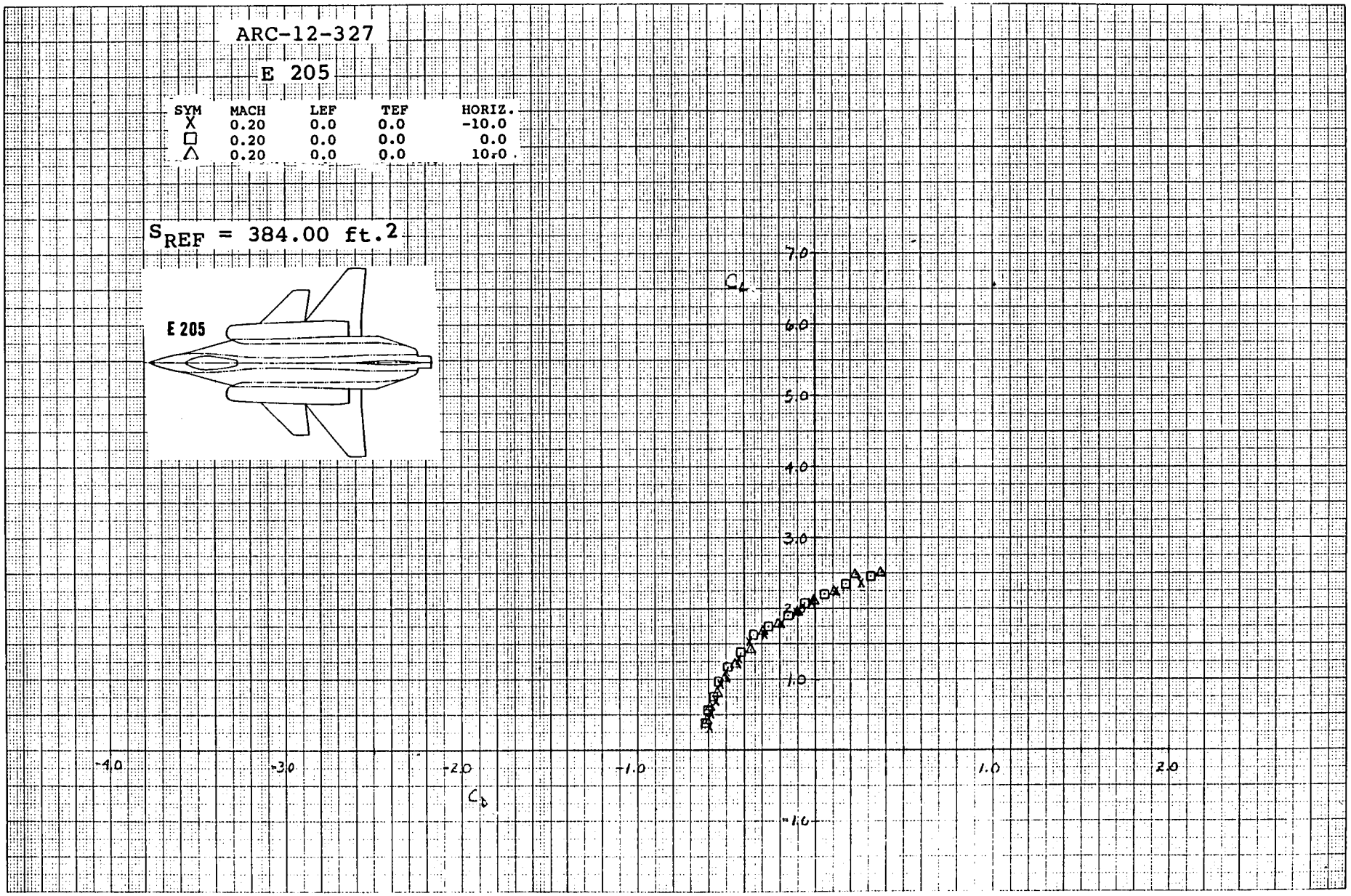

Figurel-24bDrag Predicted Data with Canard Deflections and Wing Trailing-Edge Flap Undeflected, Mach = .2

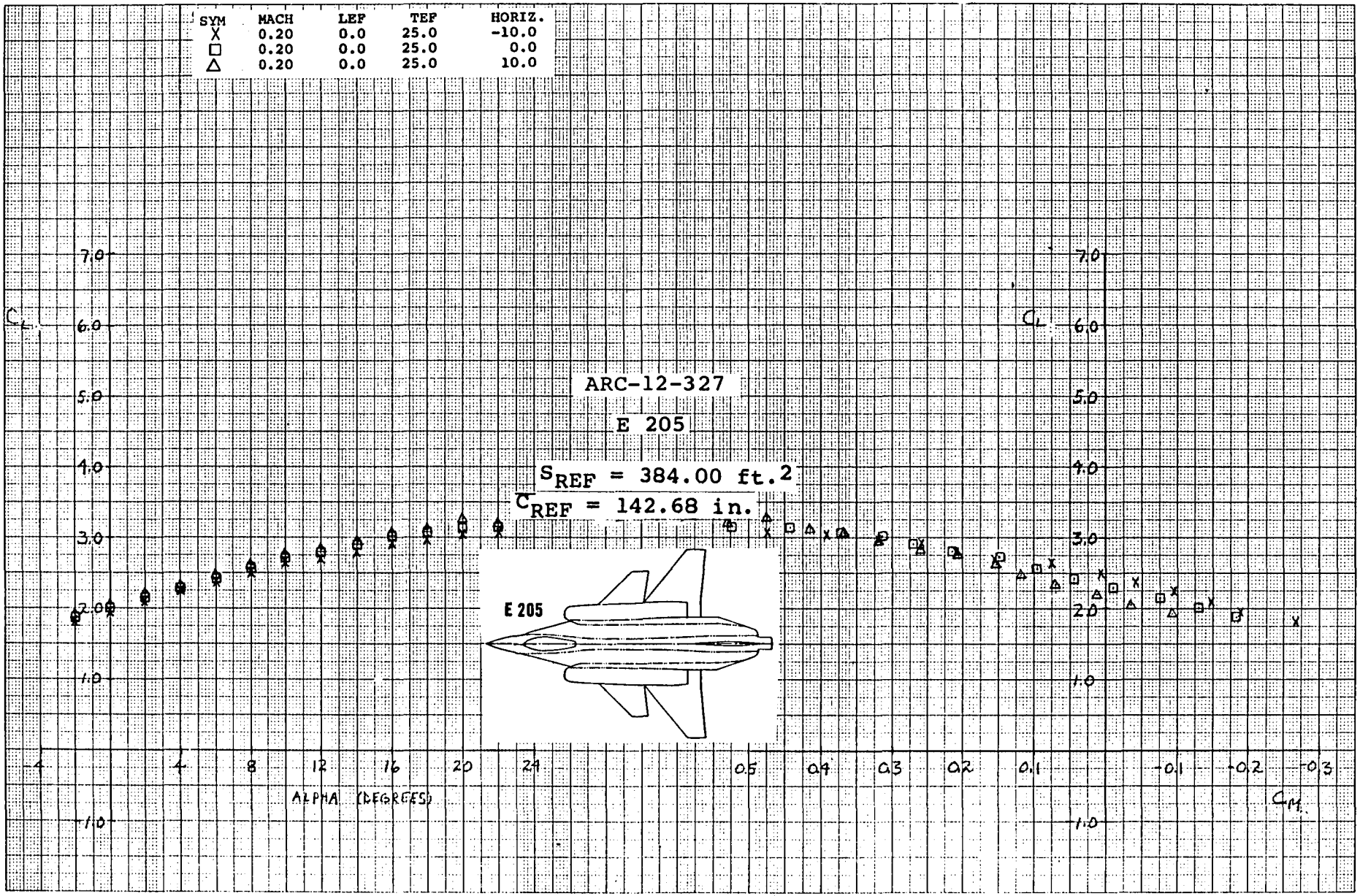

Figurel-25aLift and Moment Predicted Data with Canard Deflections and Wing Trailing-Edge Flap Deflected +25°, Mach = .2

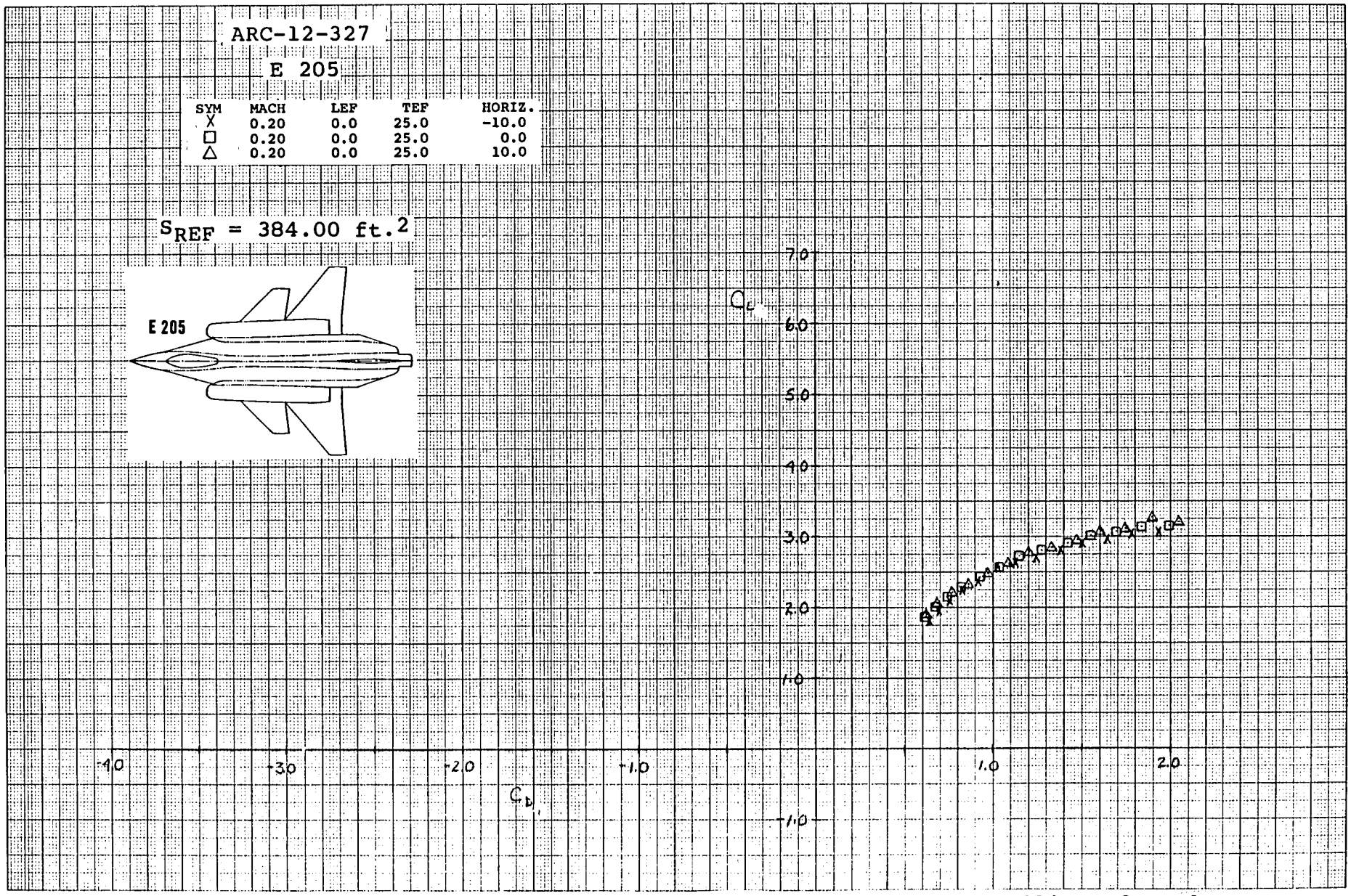

Figurel-25bDrag Predicted Data with Canard Deflections and Wing Trailing-Edge Flap Deflected +25°, Mach = .2

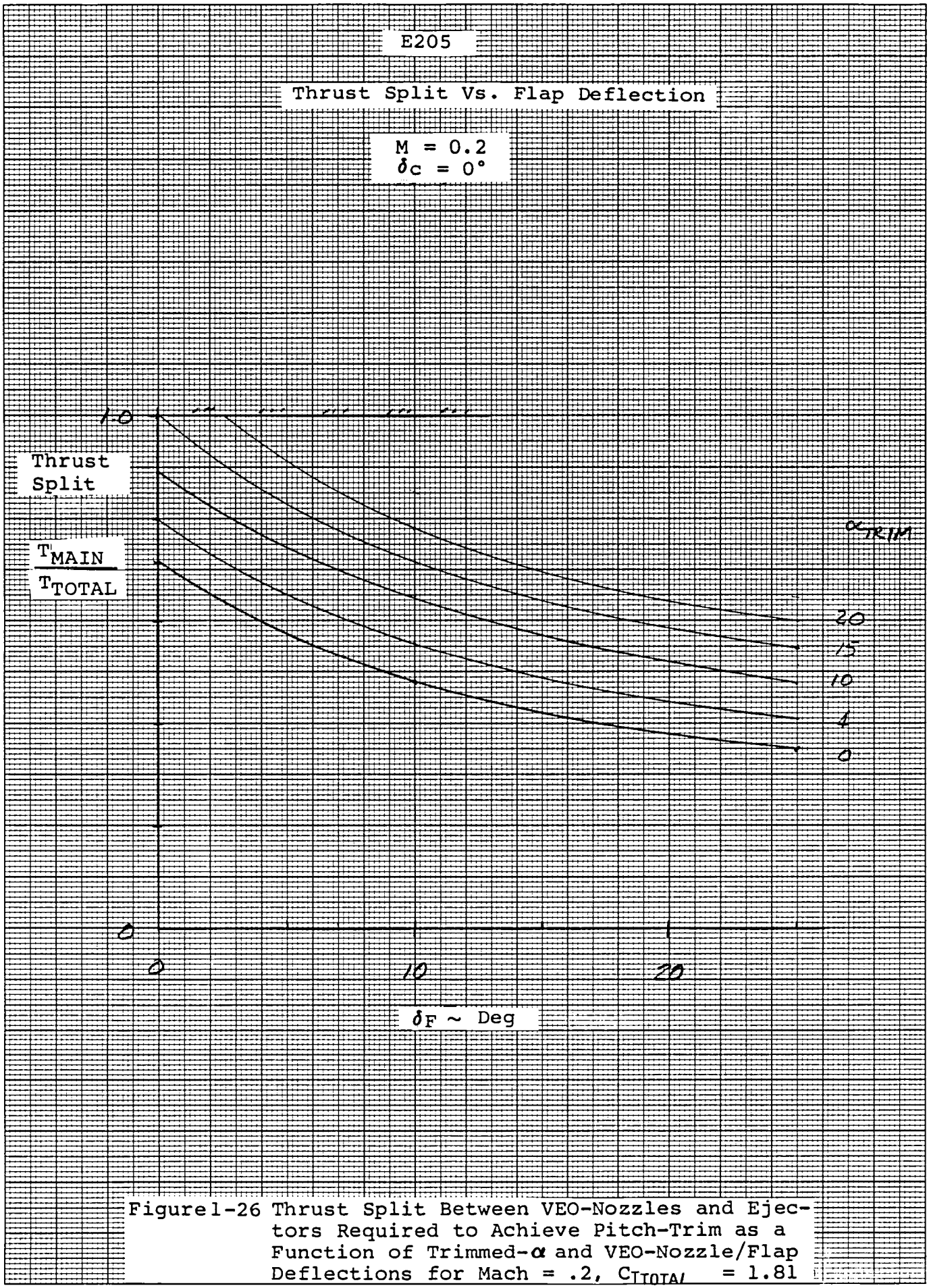

Figure1-26 Thrust Split Between VEO-Nozzles and Ejectors Required to Achieve Pitch-Trim as a Function of Trimmed-α and VEO-Nozzle/Flap Deflections for Mach = .2, $C_{T_{TOTAL}}$ = 1.81

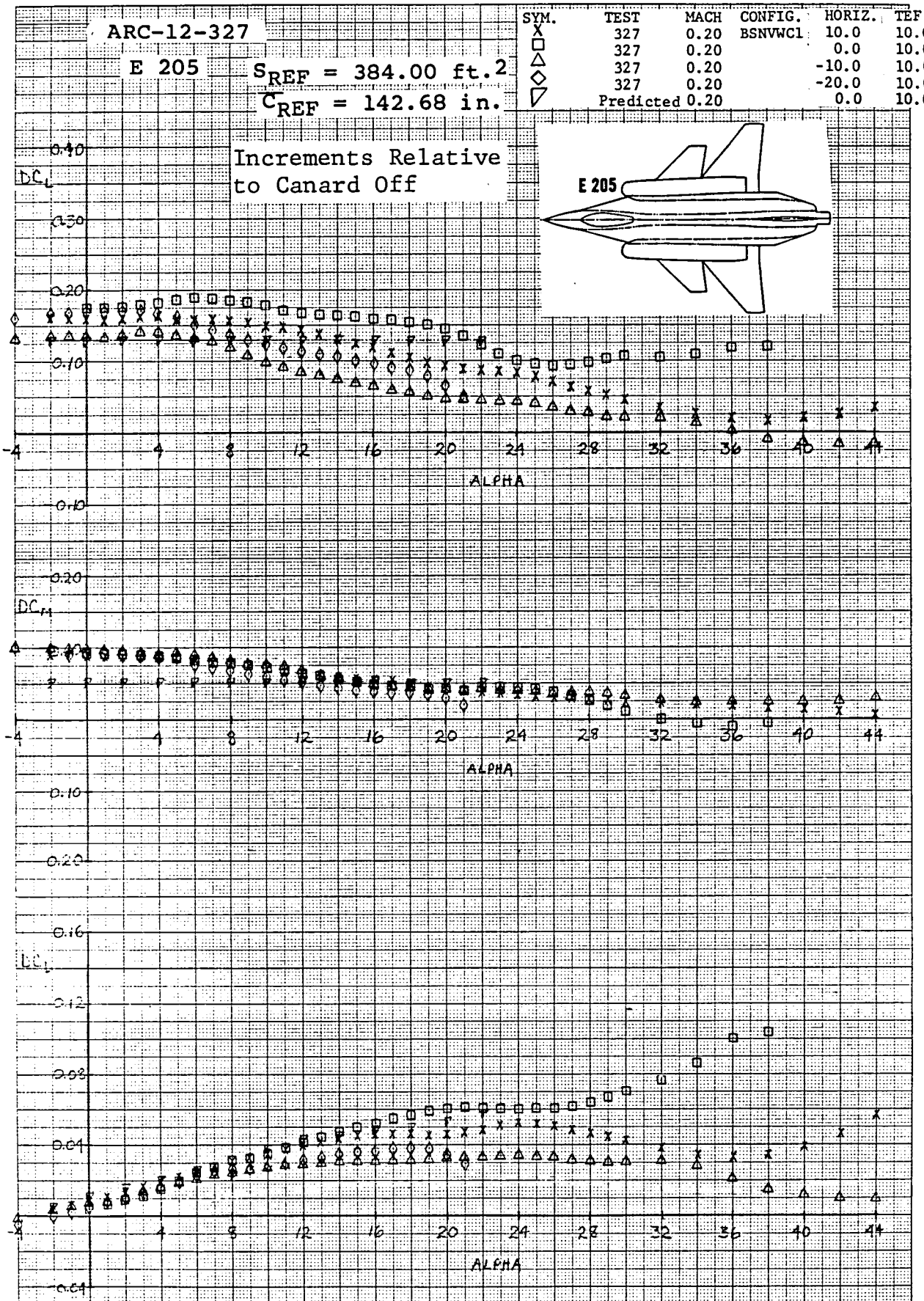

Figure 1-27 Incremental Effects of Canard Deflection with Wing Trailing-Edge Flap Deflected +10° for Test and Predicted Data, Mach = .2

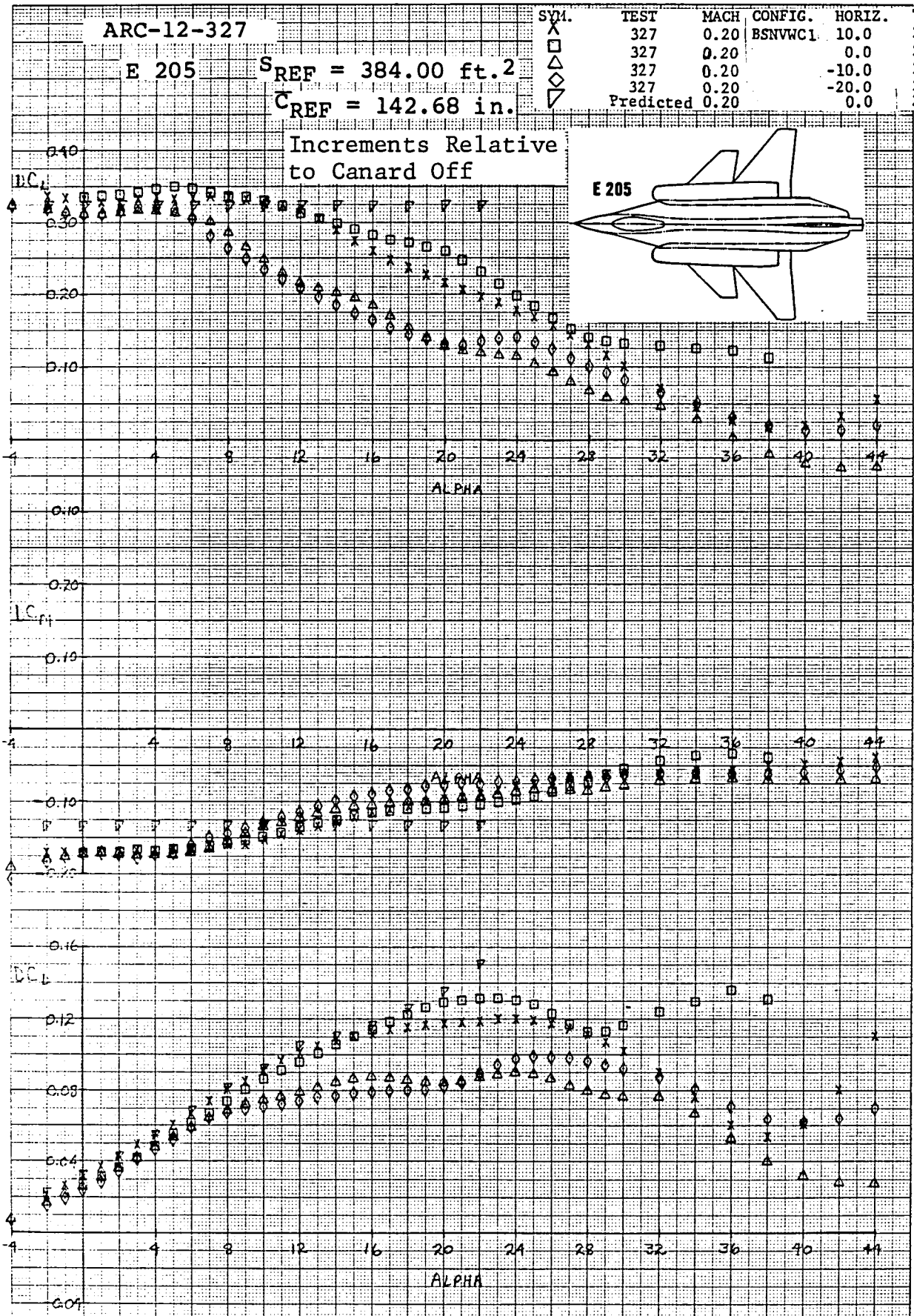

Figure1-28 Incremental Effects of Canard Deflection with Wing Trailing-Edge Flap Deflected +25° for Test and Predicted Data, Mach = .2

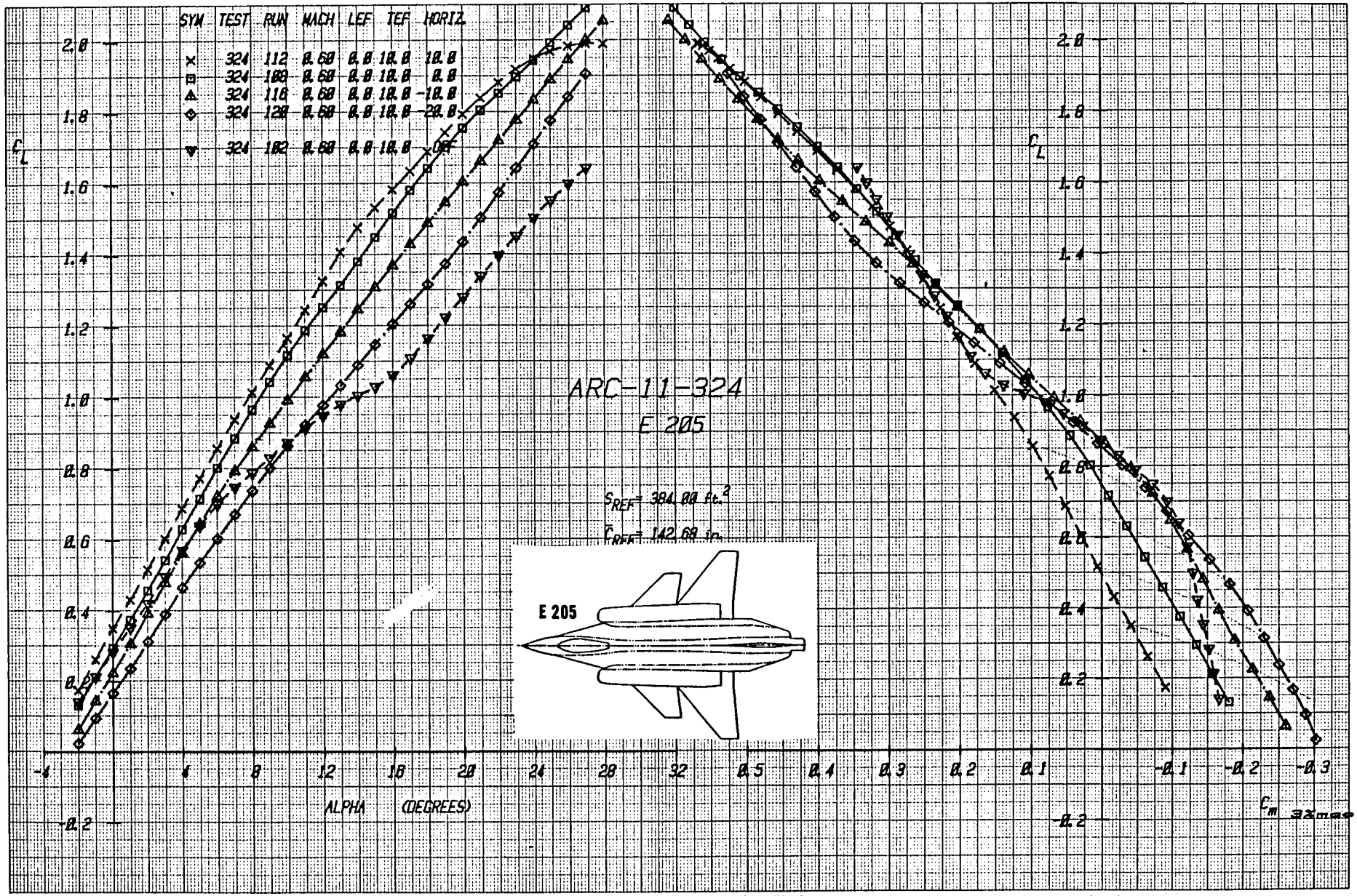

Figure1-29aEffect of Canard Deflection on Lift and Moment With Wing Trailing-Edge Flap Deflected +10°, Mach = .6

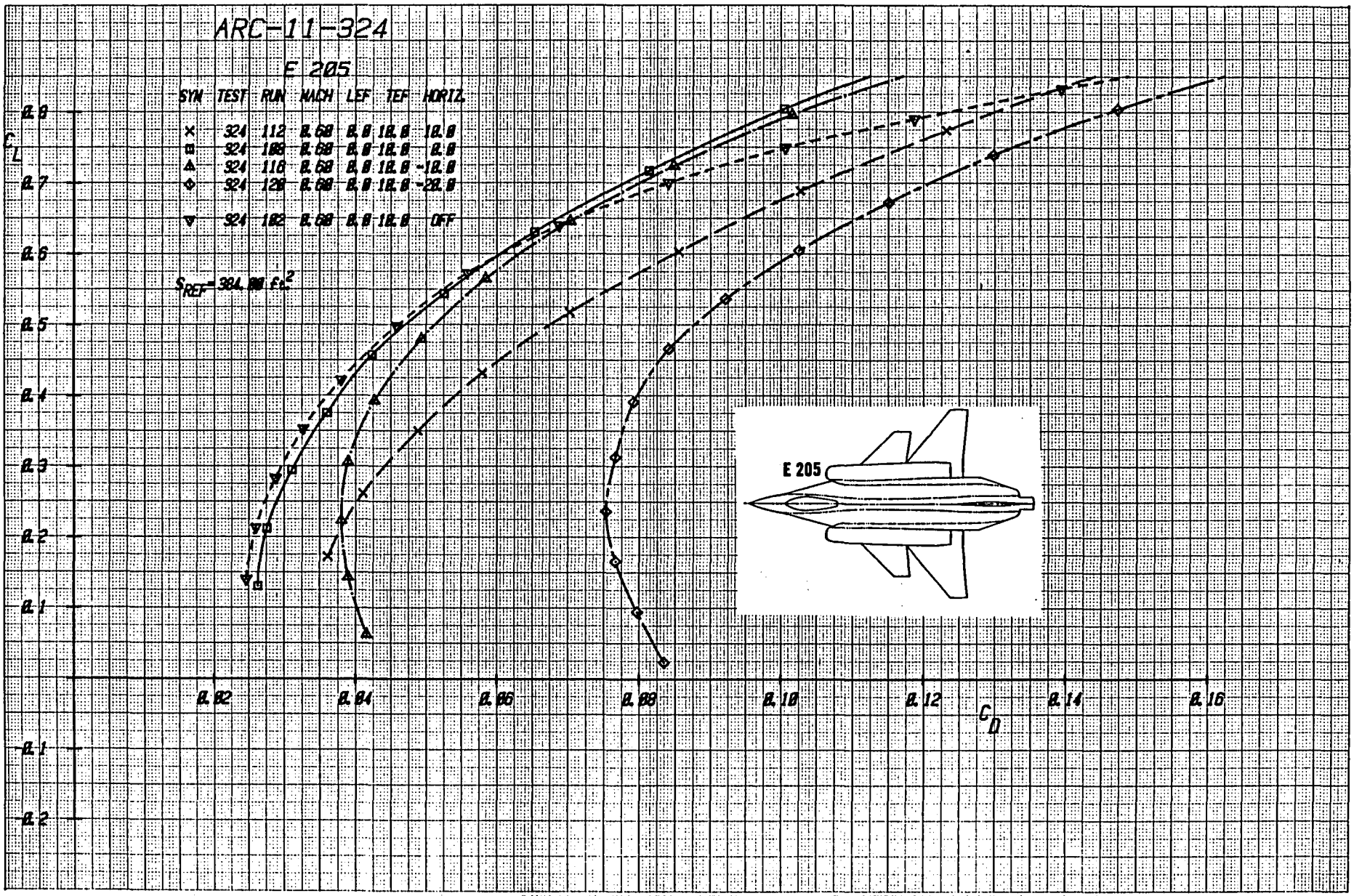

Figure1-29bEffect of Canard Deflection on Drag With Wing Trailing-Edge Flap Deflected +10°, Mach = .6

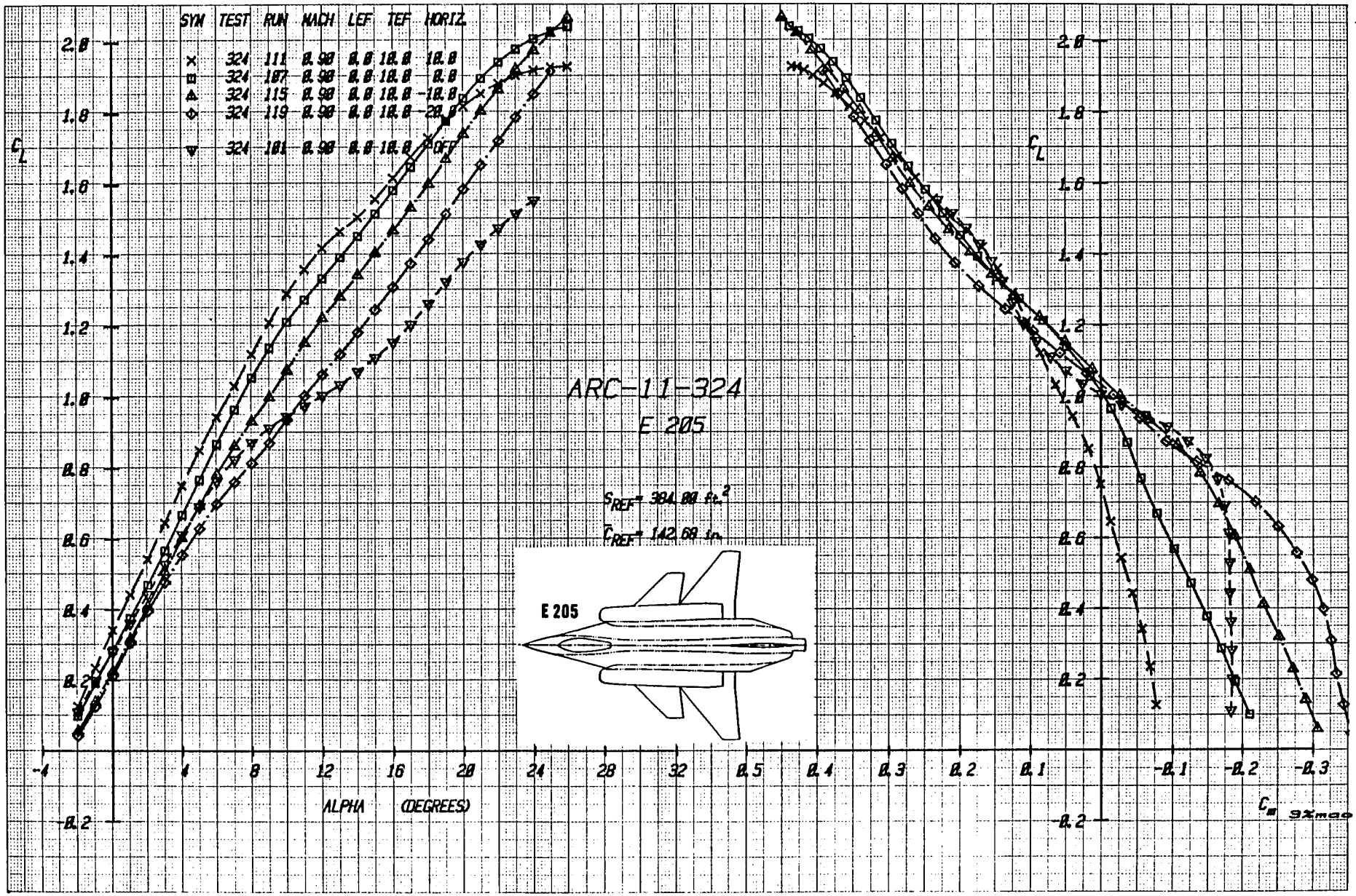

Figurel-30aEffect of Canard Deflection on Lift and Moment With Wing Trailing-Edge Flap Deflected +10°, Mach = .9

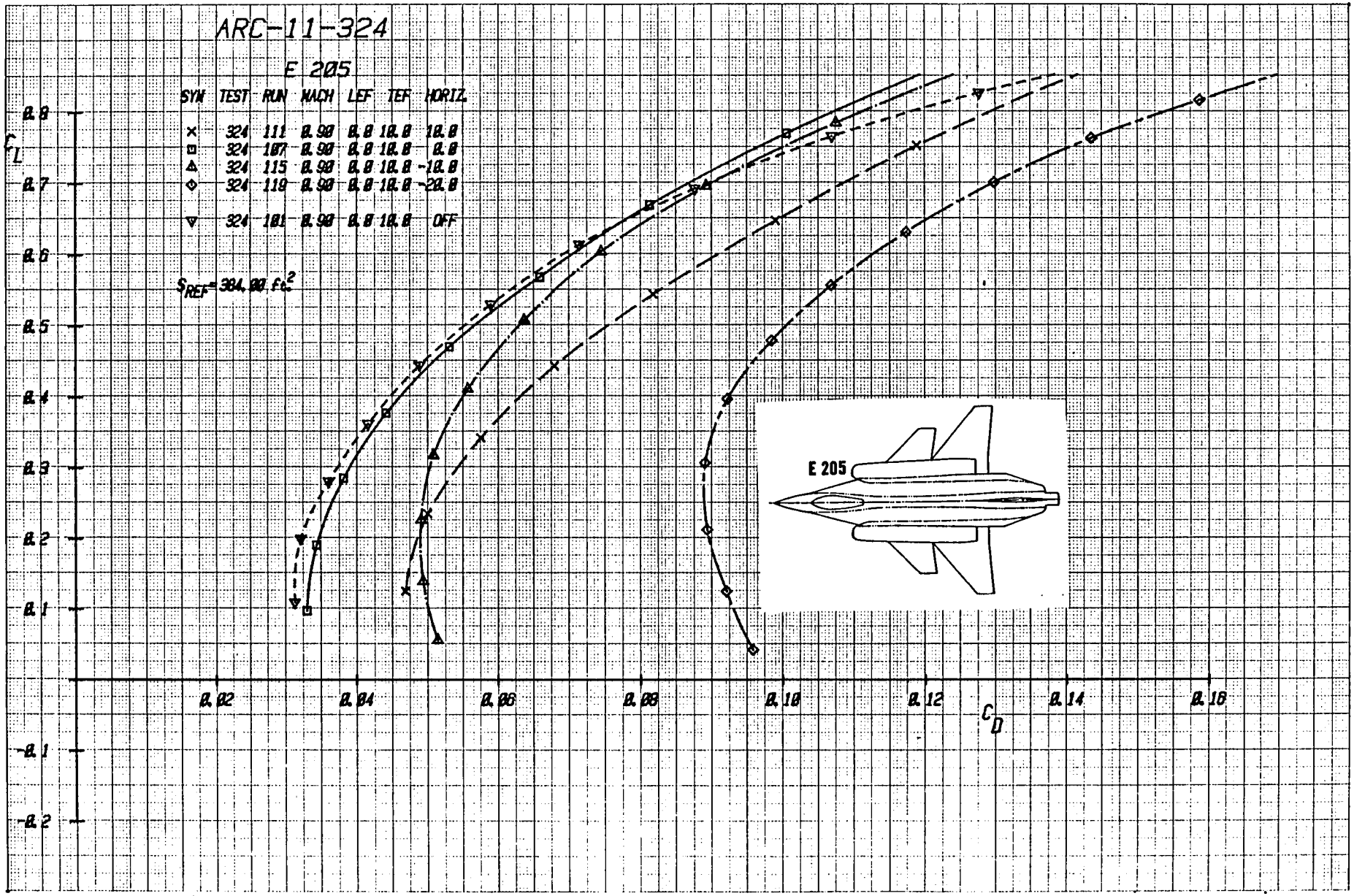

Figure1-30bEffect of Canard Deflection on Drag With Wing Trailing-Edge Flap Deflected +10°, Mach = .9

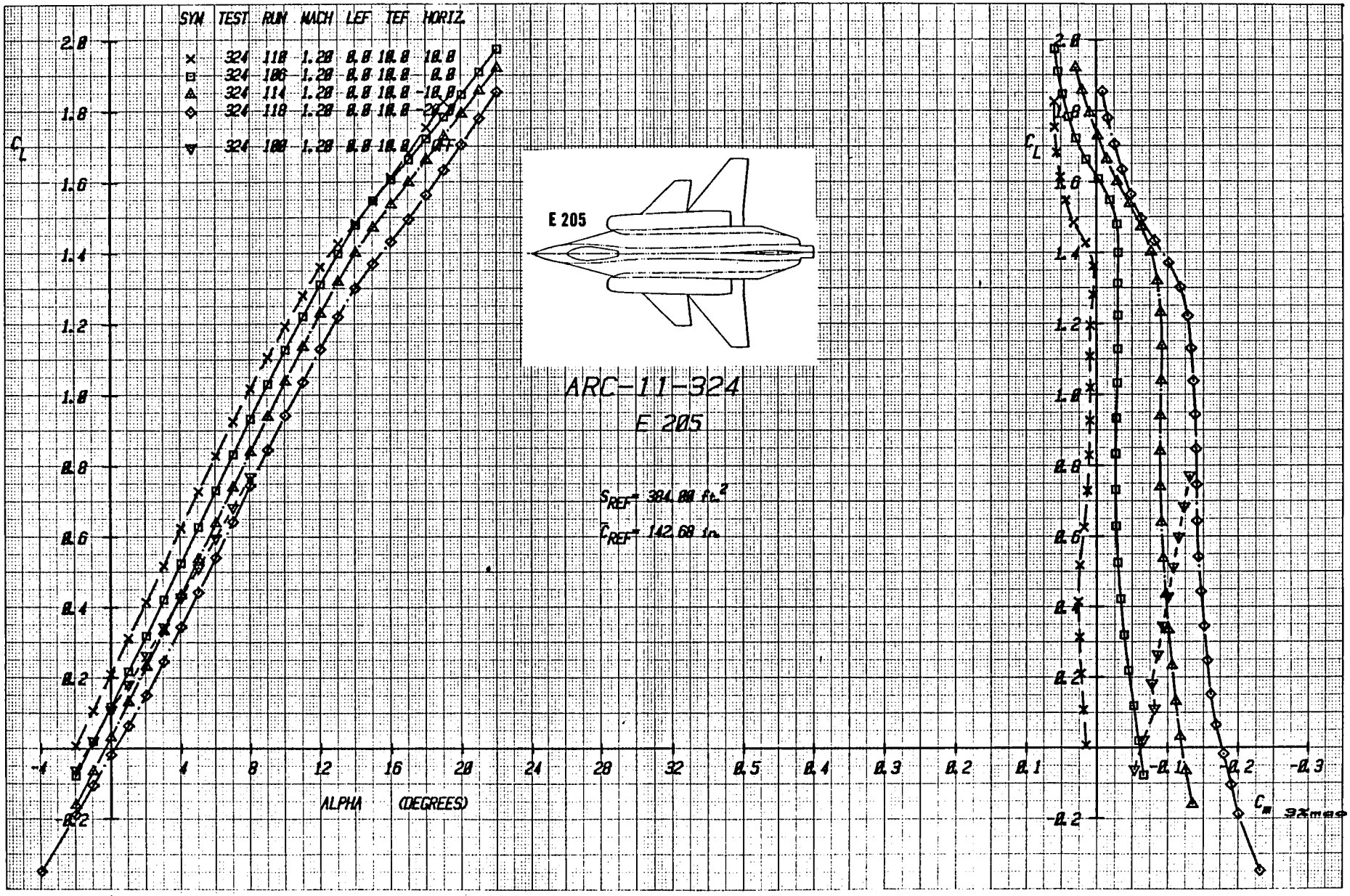

Figurel-3laEffect of Canard Deflection on Lift and Moment With Wing Trailing-Edge Flap Deflected +10°, Mach = 1.2

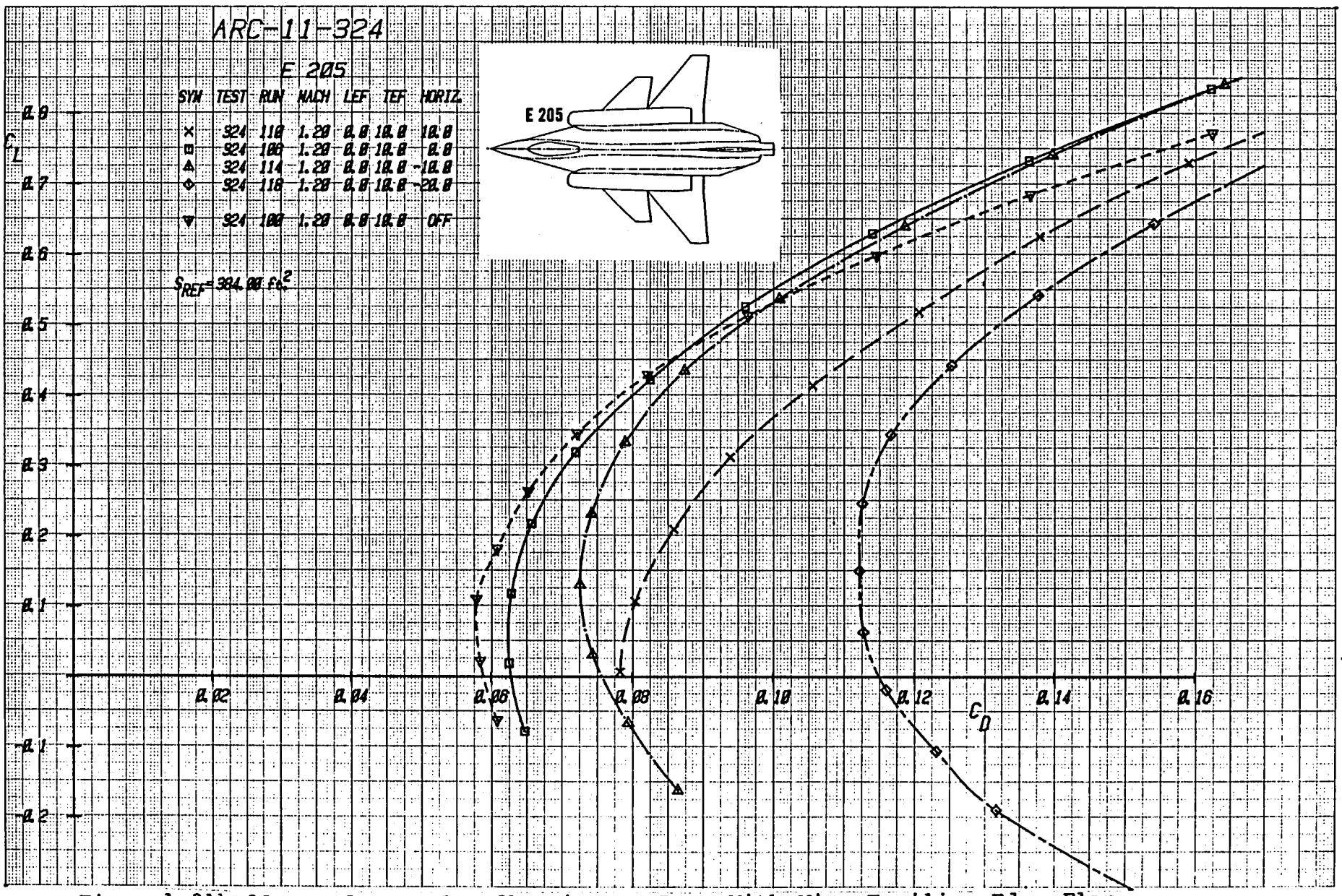

Figurel-31bEffect of Canard Deflection on Drag With Wing Trailing-Edge Flap Deflected +10°, Mach = 1.2

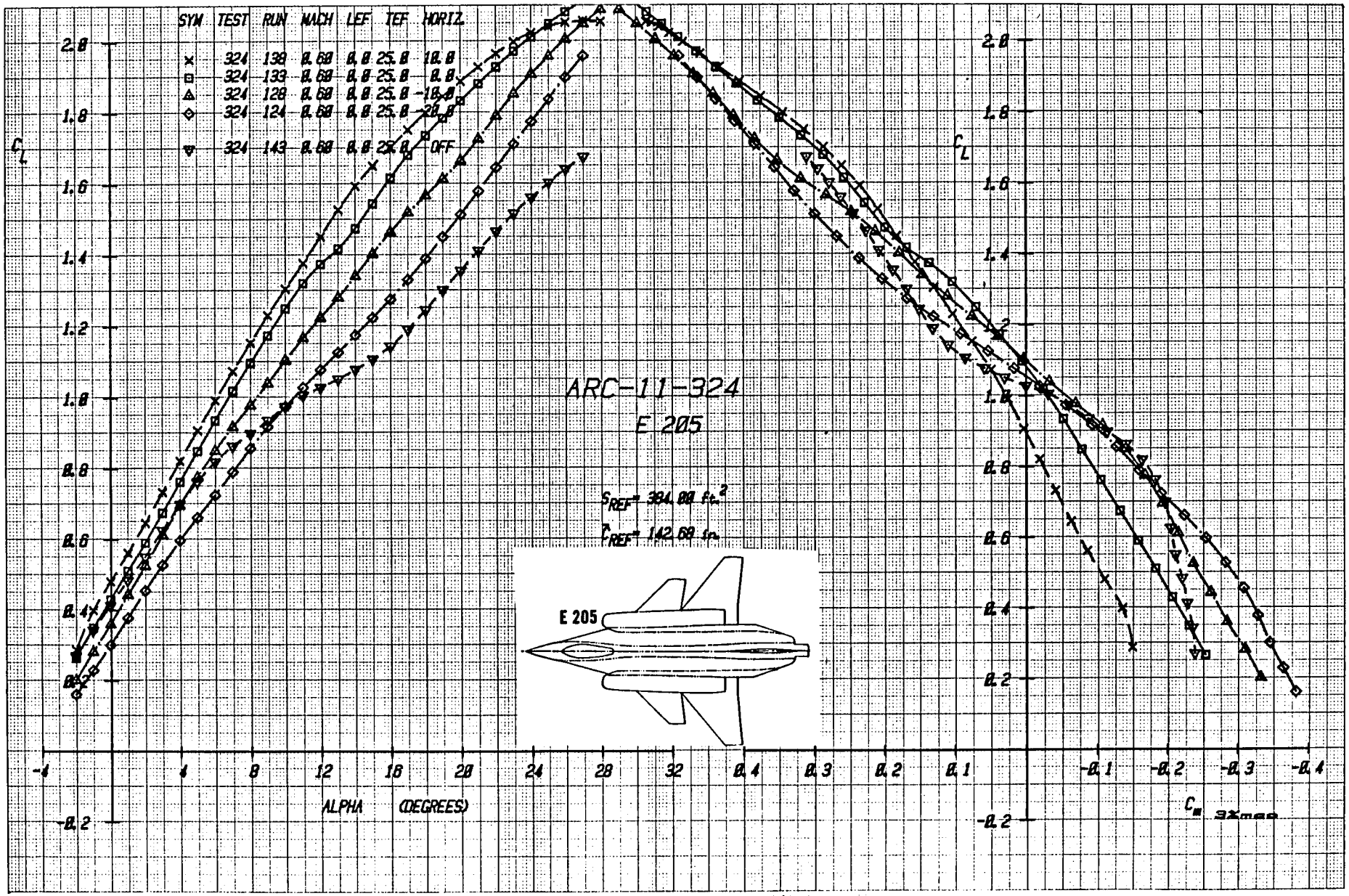

Figurel-32aEffect of Canard Deflection on Lift and Moment With Wing Trailing-Edge Flap Deflected +25°, Mach = .6

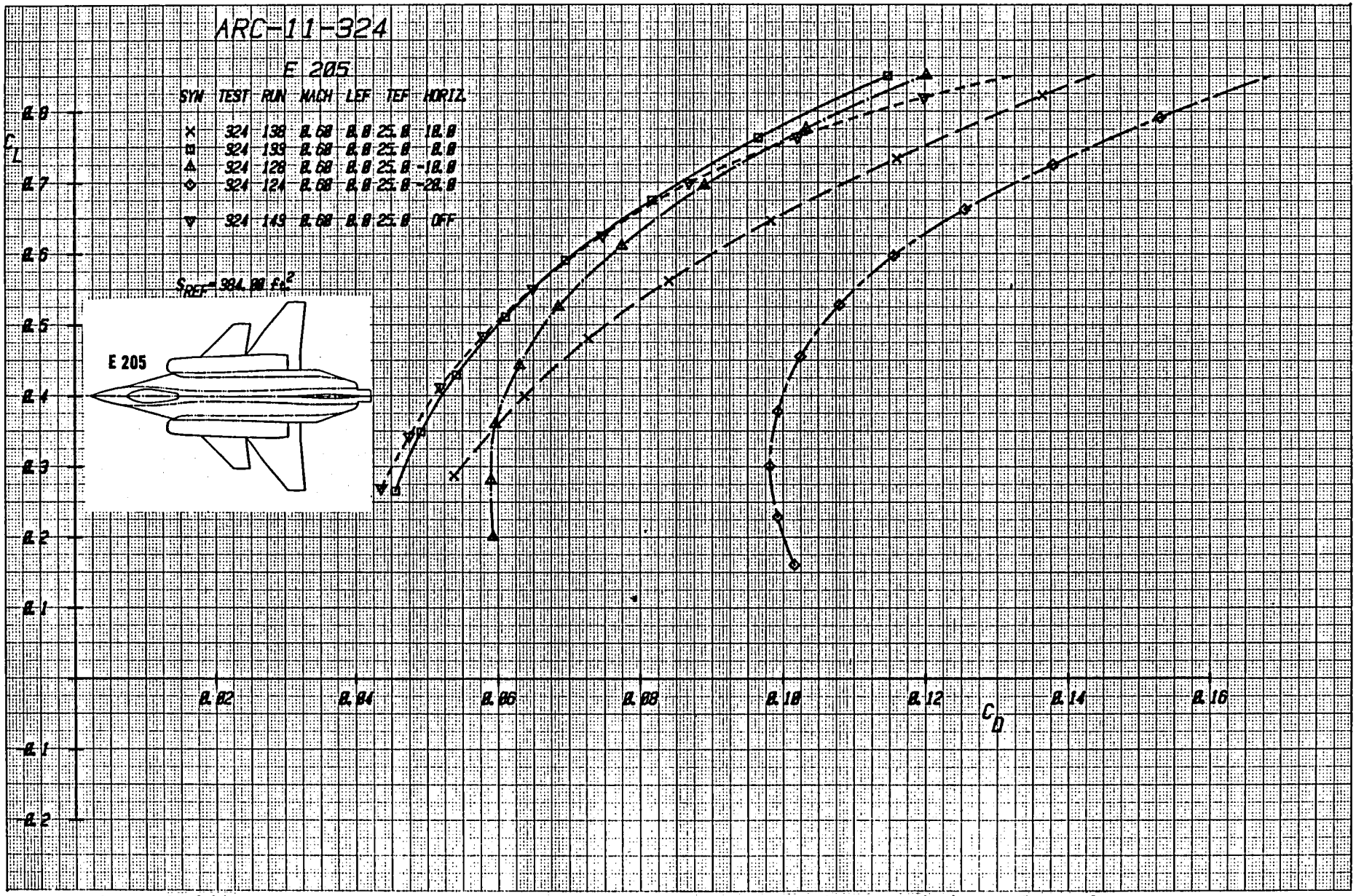

Figurel-32bEffect of Canard Deflection on Drag With Wing Trailing-Edge Flap Deflected +25°, Mach = .6

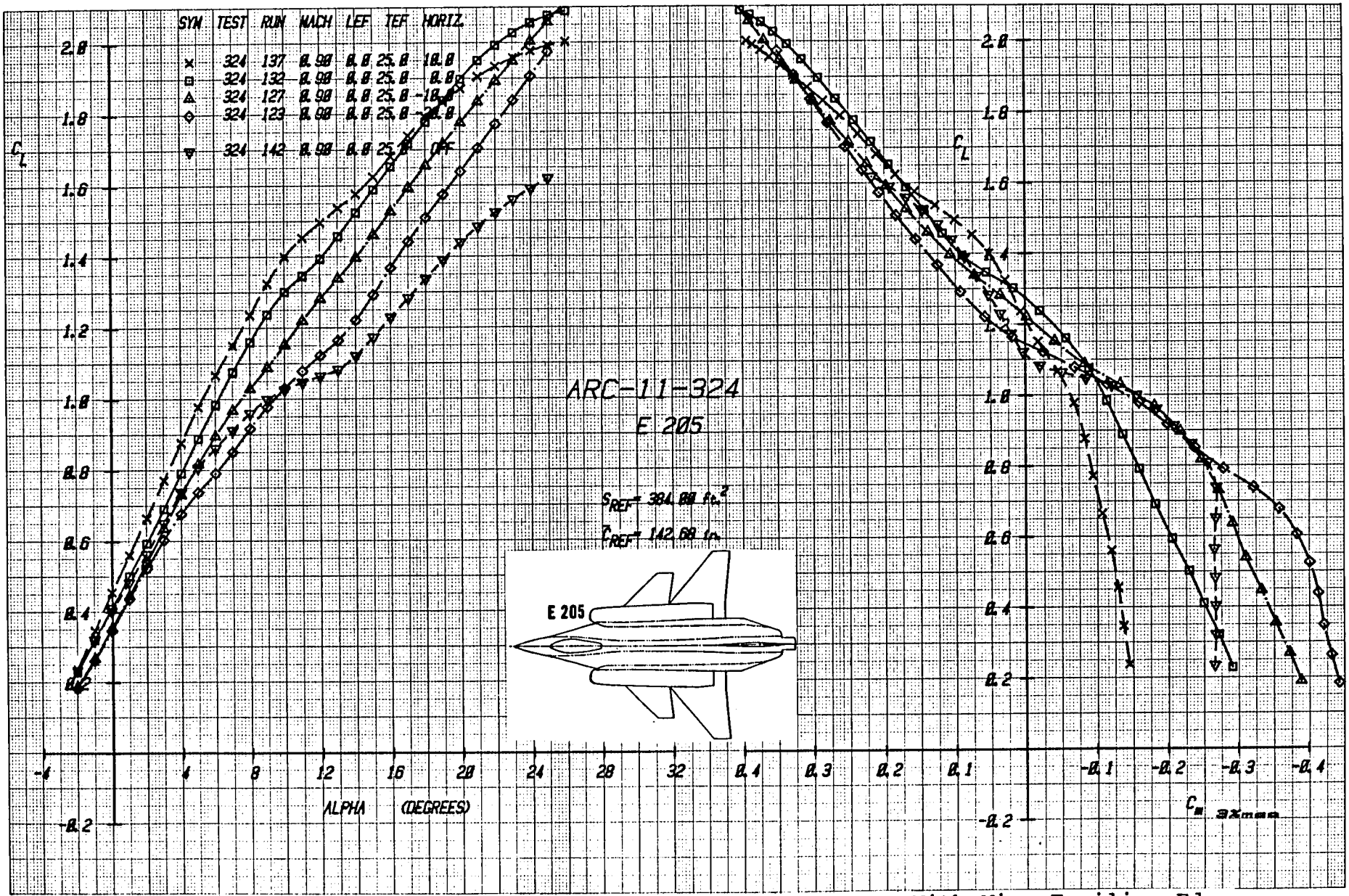

Figure1-33aEffect of Canard Deflection on Lift and Moment With Wing Trailing-Edge Flap Deflected +25°, Mach = .9

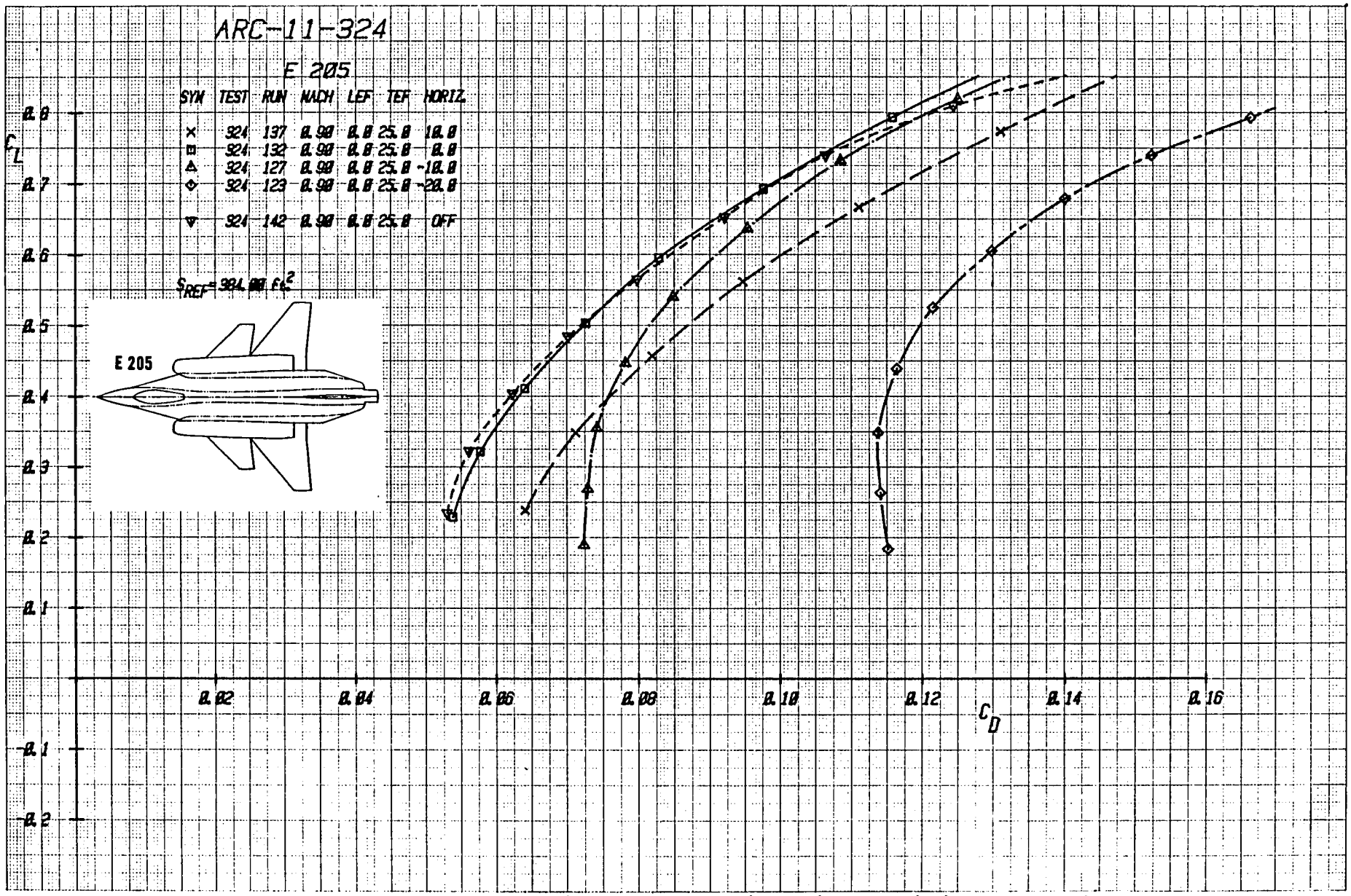

Figurel-33bEffect of Canard Deflection on Drag With Wing Trailing-Edge Flap Deflected +25°, Mach = .9

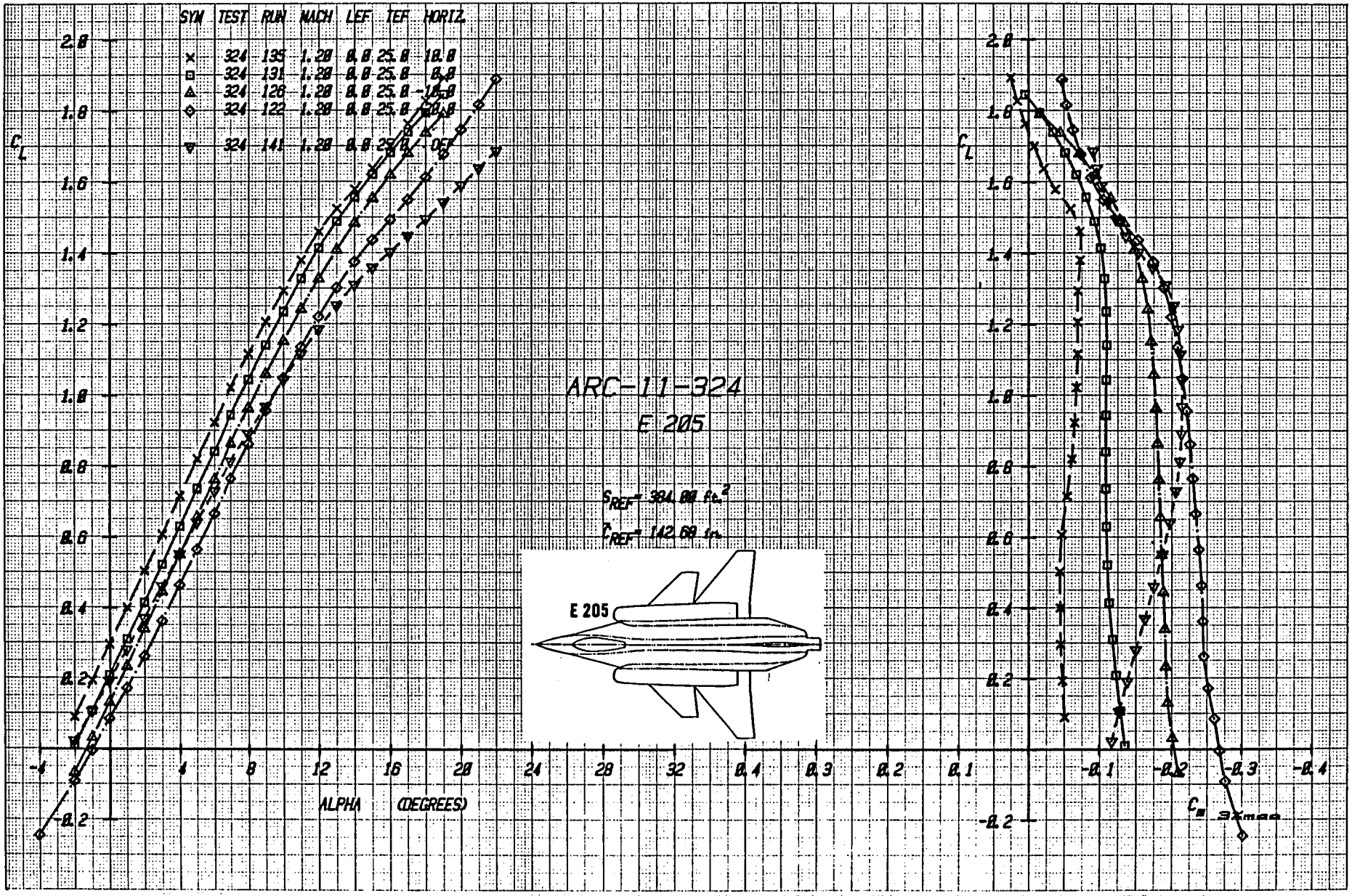

Figurel-34aEffect of Canard Deflection on Lift and Moment With Wing Trailing-Edge Flap Deflected +25°, Mach = 1.2

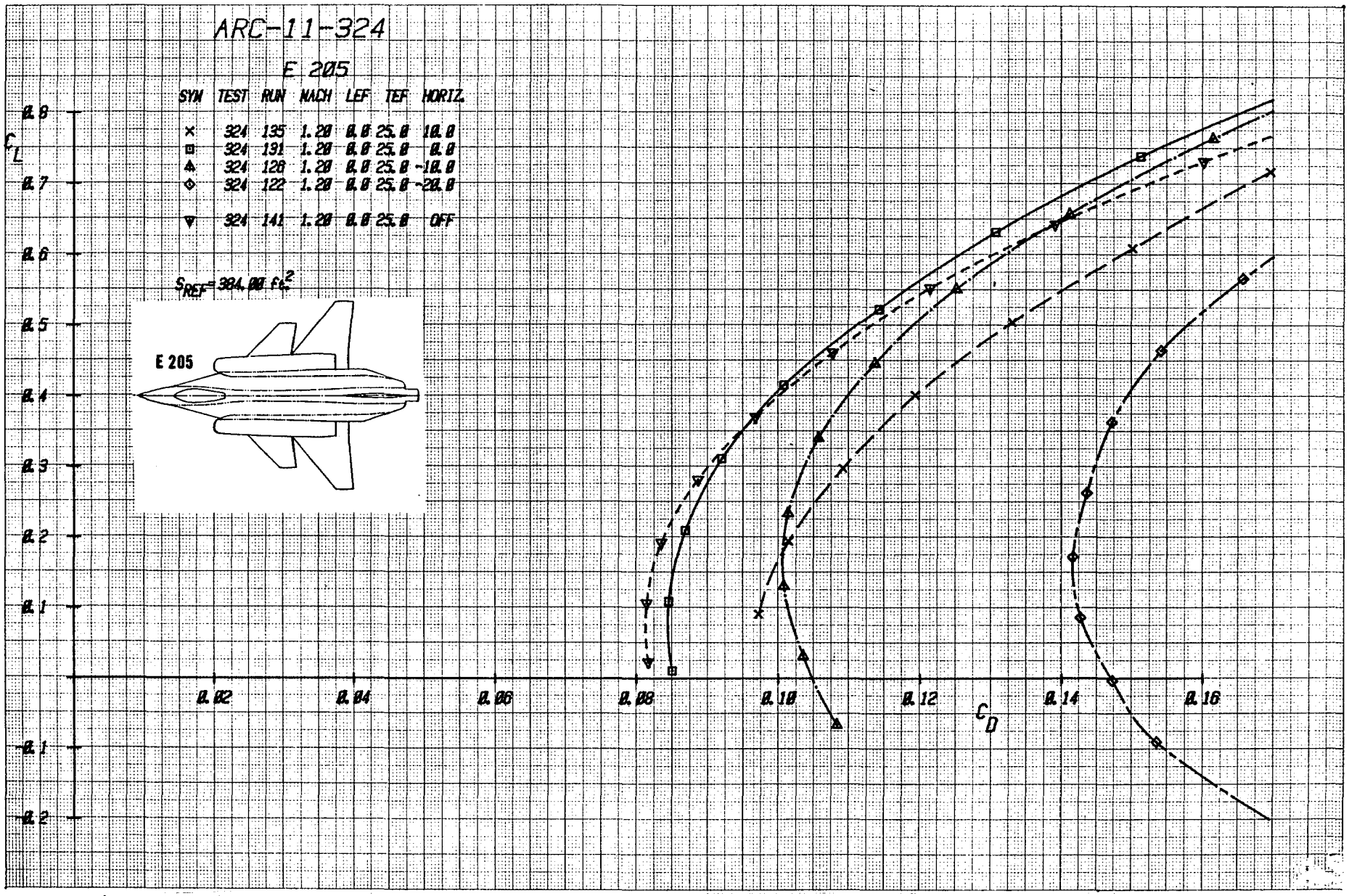

Figure1-34bEffect of Canard Deflection on Drag With Wing Trailing-Edge Flap Deflected +25°, Mach = 1.2

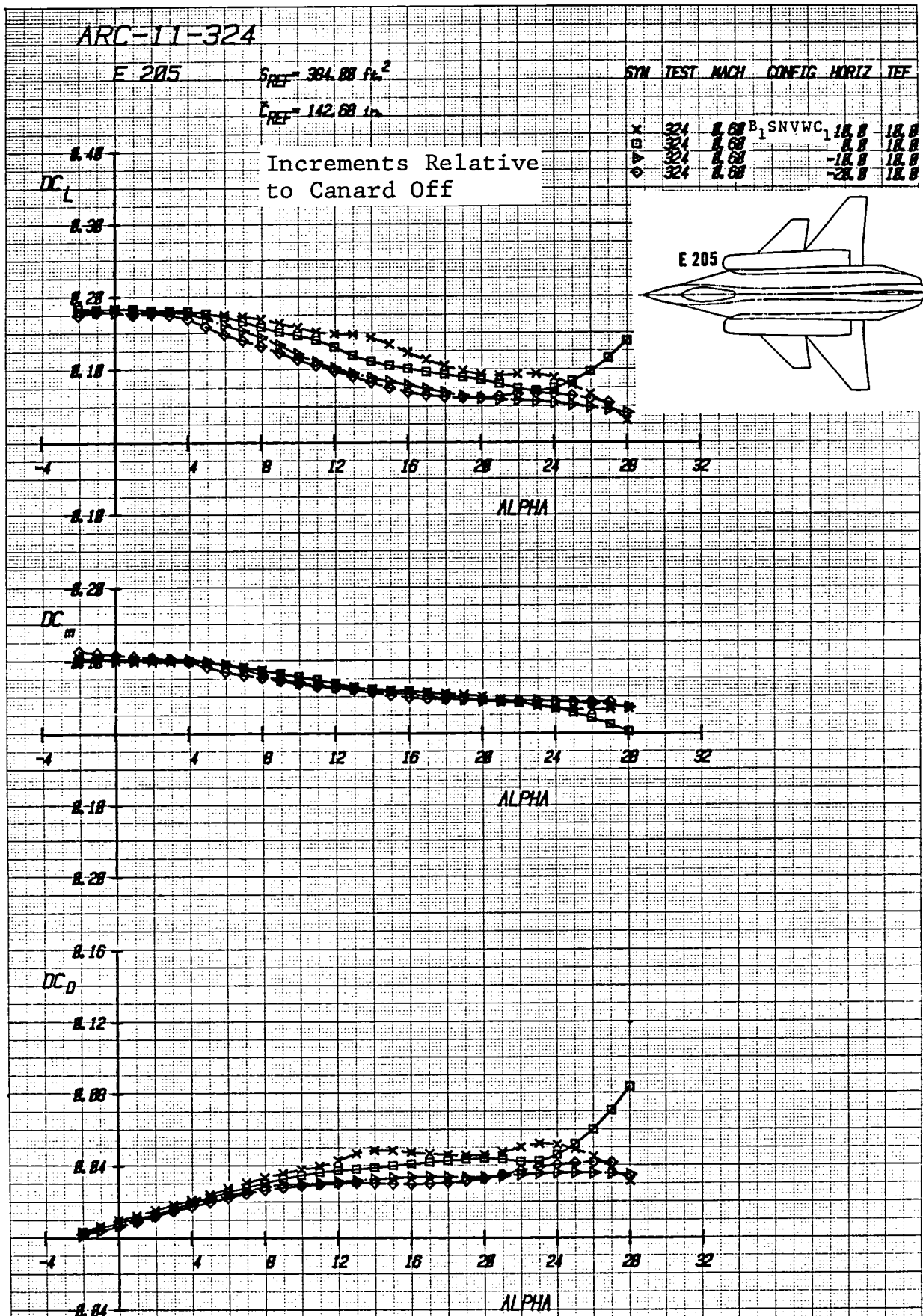

Figure 1-35 Incremental Effects Due to Deflecting the Wing Trailing-Edge Flaps +10° while in Presence of Various Canard Deflections for Baseline E205 Configuration, Mach = .6

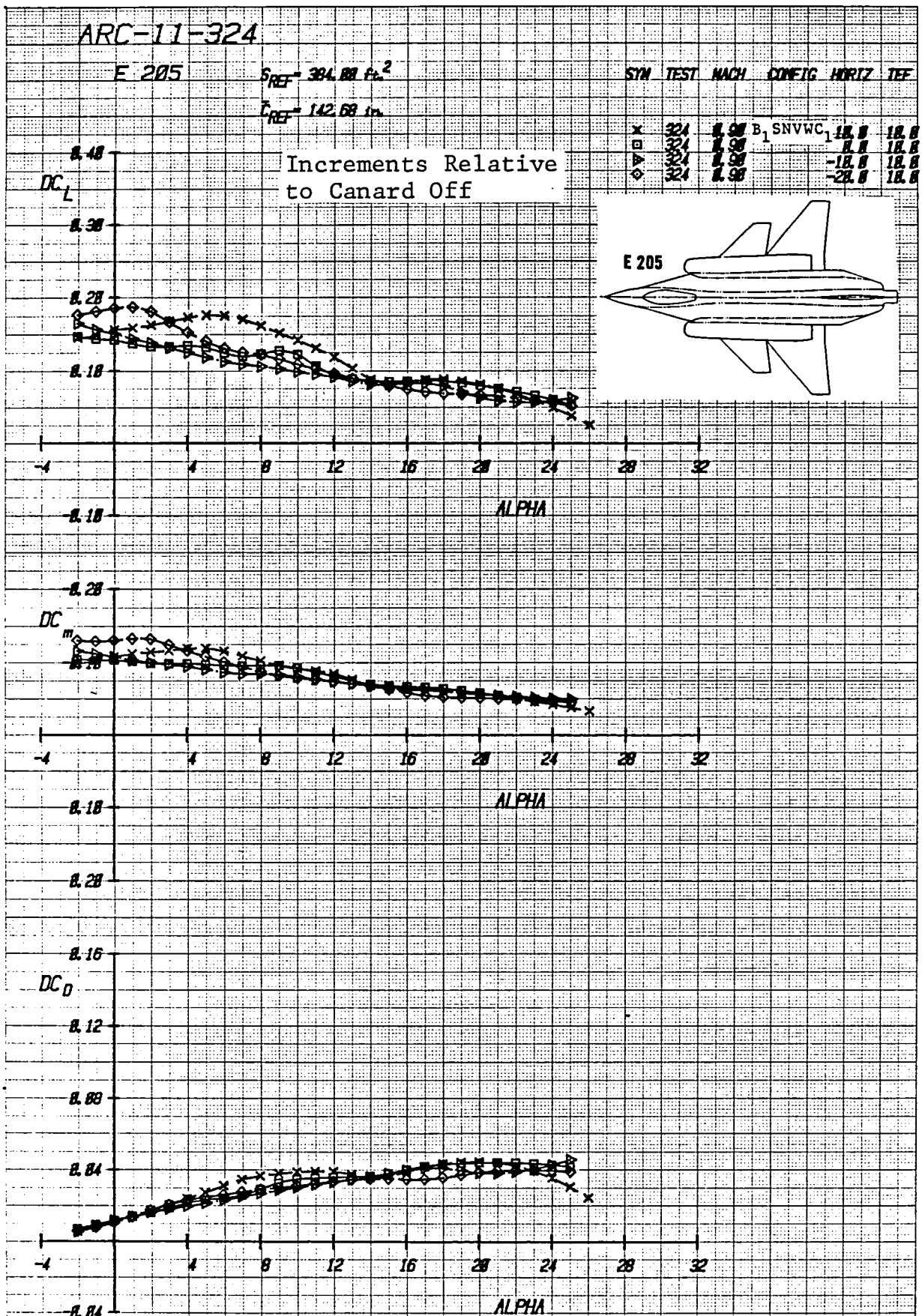

Figure 1-36 Incremental Effects Due to Deflecting the Wing Trailing-Edge Flaps +10° while in Presence of Various Canard Deflections for Baseline E205 Configuration, Mach = .9

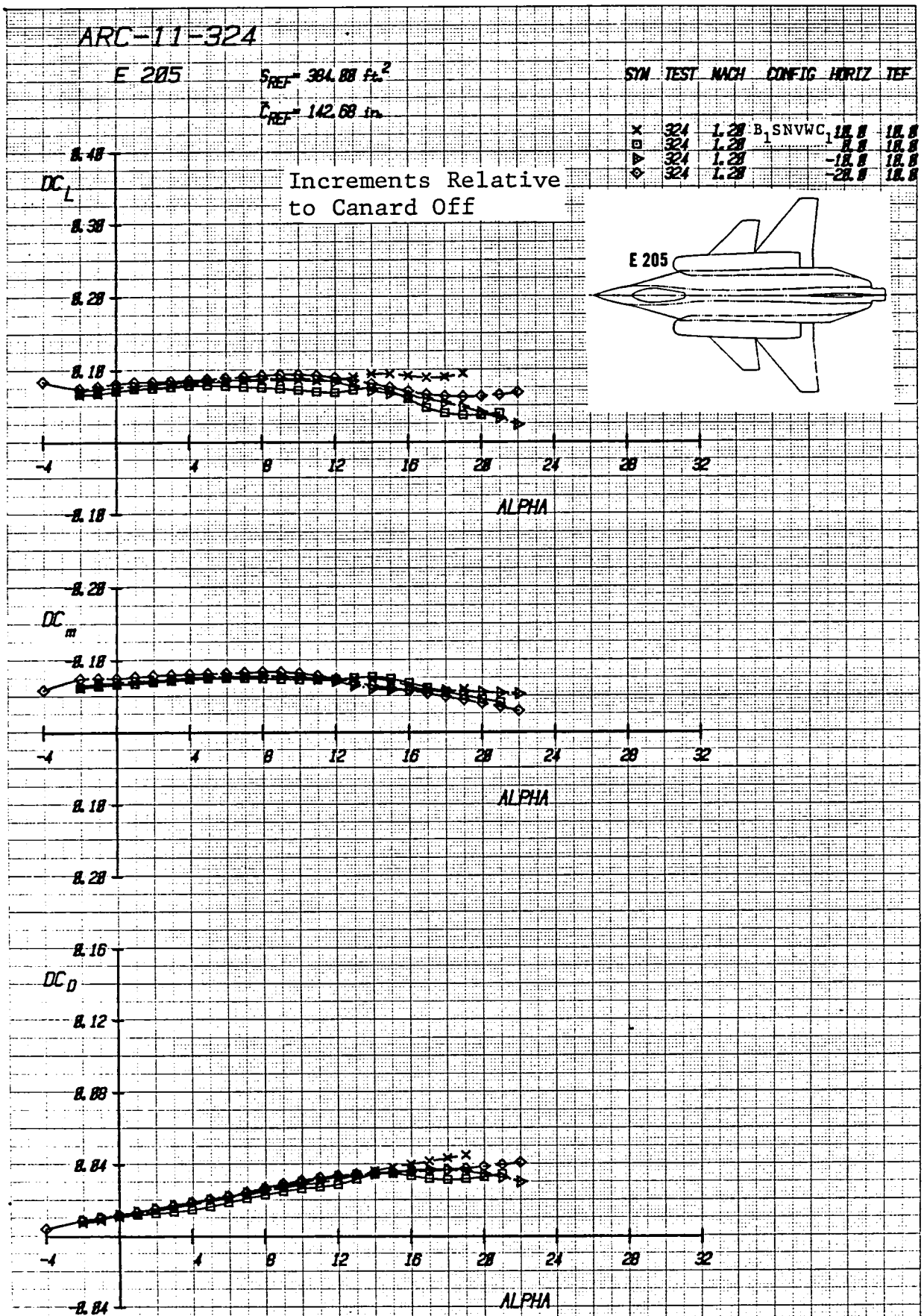

Figure 1-37 Incremental Effects Due to Deflecting the Wing Trailing-Edge Flaps +10° while in Presence of Various Canard Deflections for Baseline E205 Configuration, Mach = 1.2

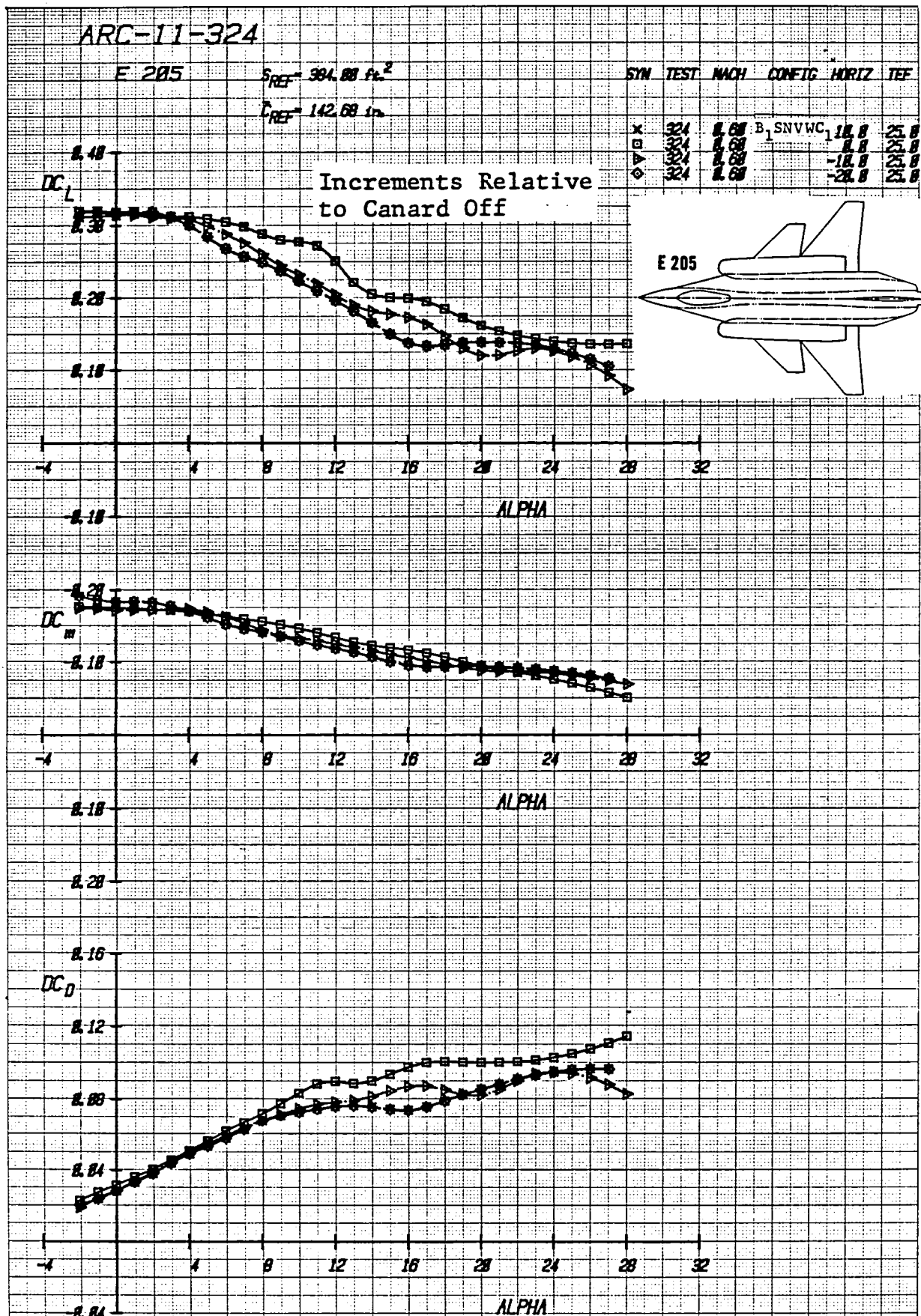

Figure 1-38 Incremental Effects Due to Deflecting the Wing Trailing-Edge Flaps +25° while in Presence of Various Canard Deflections for Baseline E205 Configuration, Mach = .6

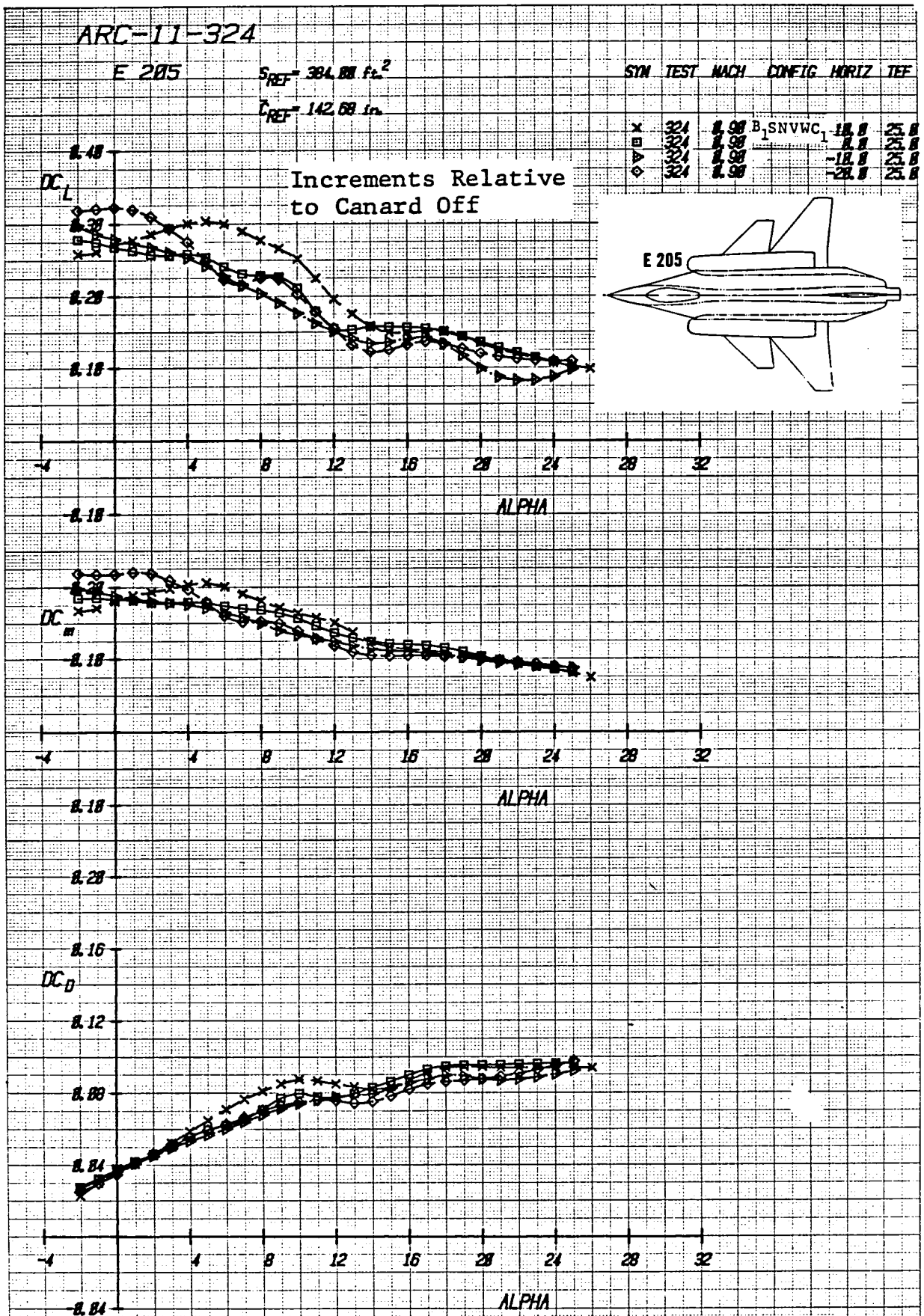

Figure1-39 Incremental Effects Due to Deflecting the Wing Trailing-Edge Flaps +25° while in Presence of Various Canard Deflections for Baseline E205 Configuration, Mach = .9

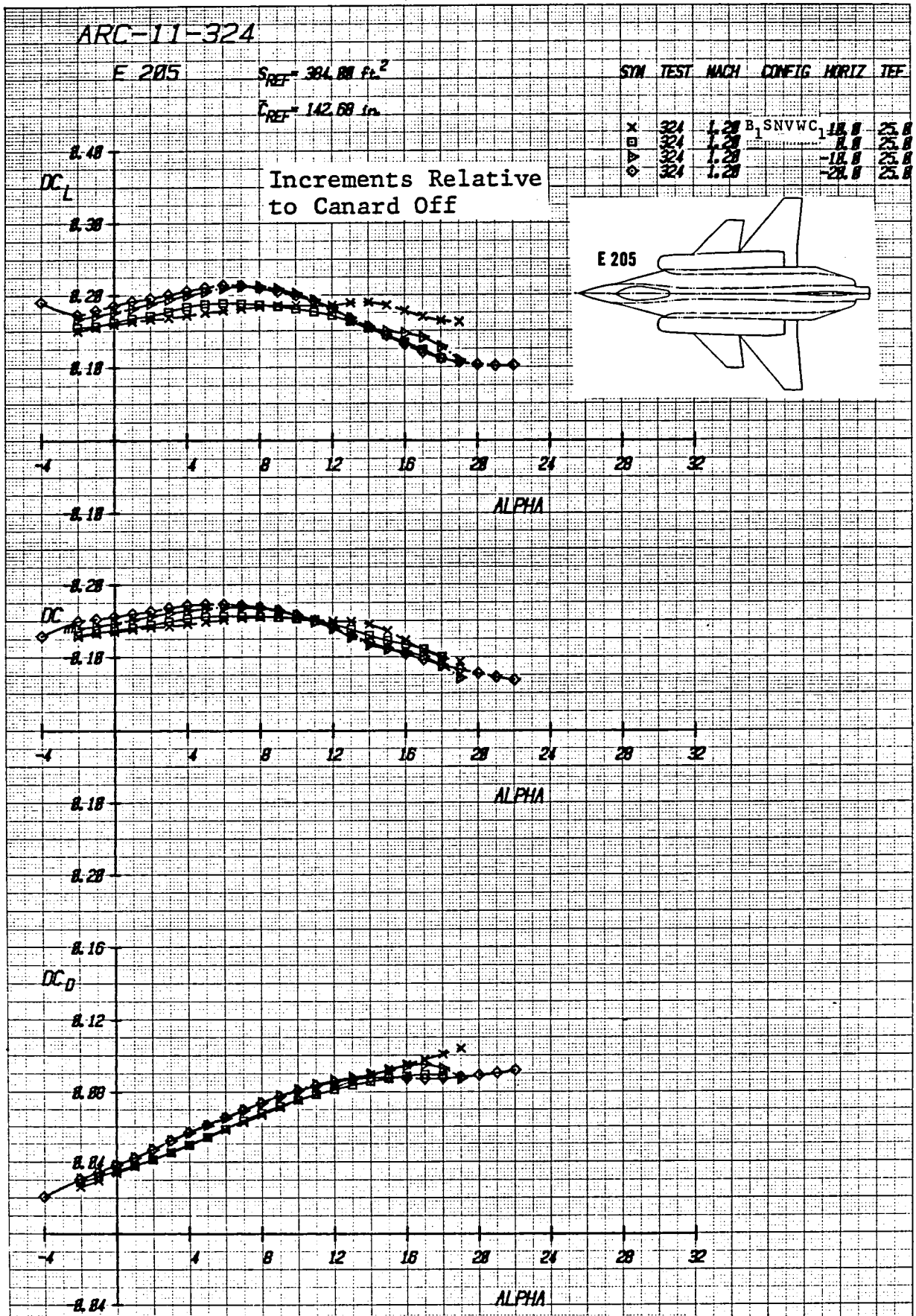

Figure 1-40 Incremental Effects Due to Deflecting the Wing Trailing-Edge Flaps +25° while in Presence of Various Canard Deflections for Baseline E205 Configuration, Mach = 1.2

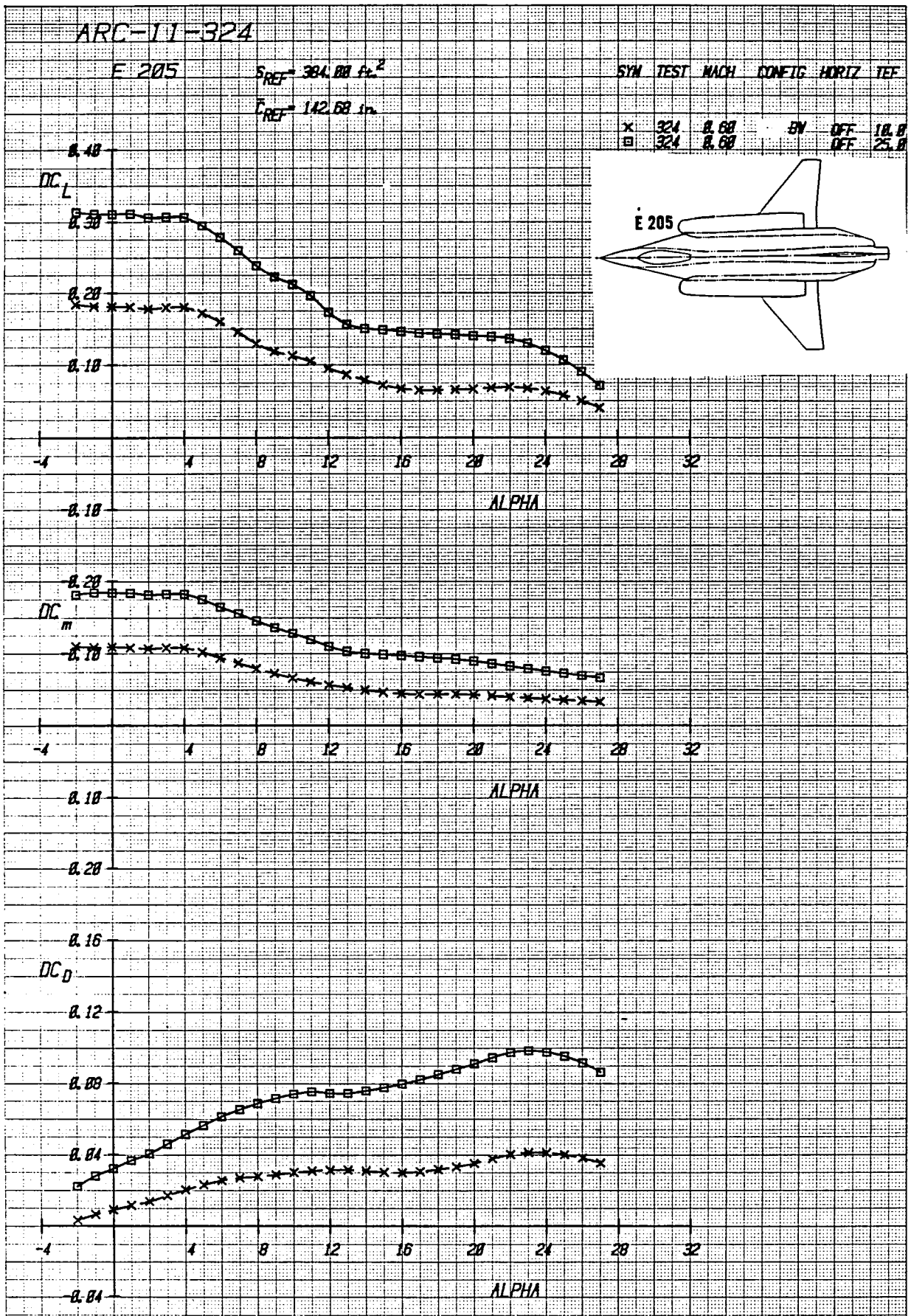

Figure 1-41 Incremental Effects of Trailing-Edge Flap Deflection With Canard Off, Mach = .6

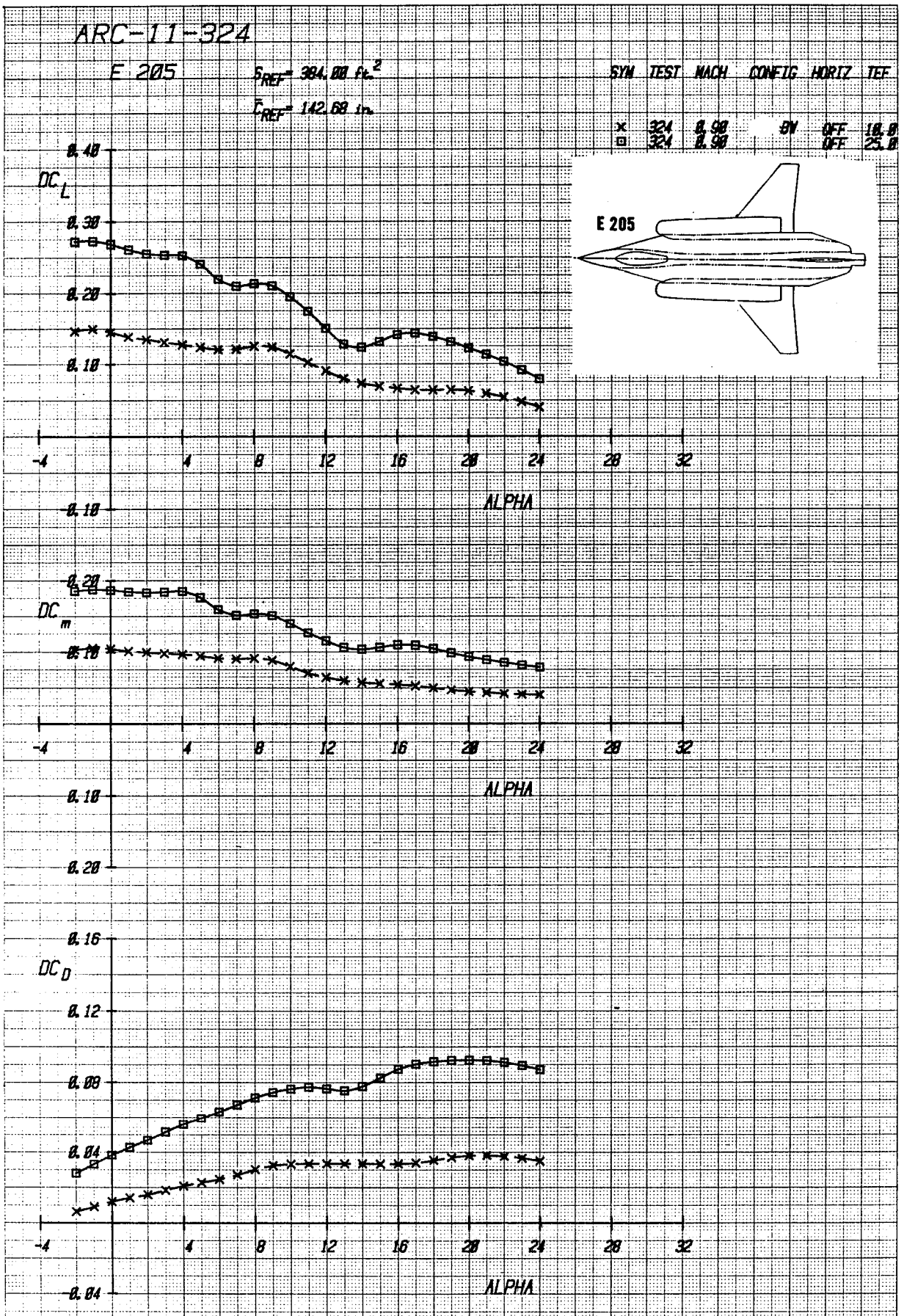

Figure 1-42 Incremental Effects of Trailing-Edge Flap Deflection With Canard Off, Mach = .9

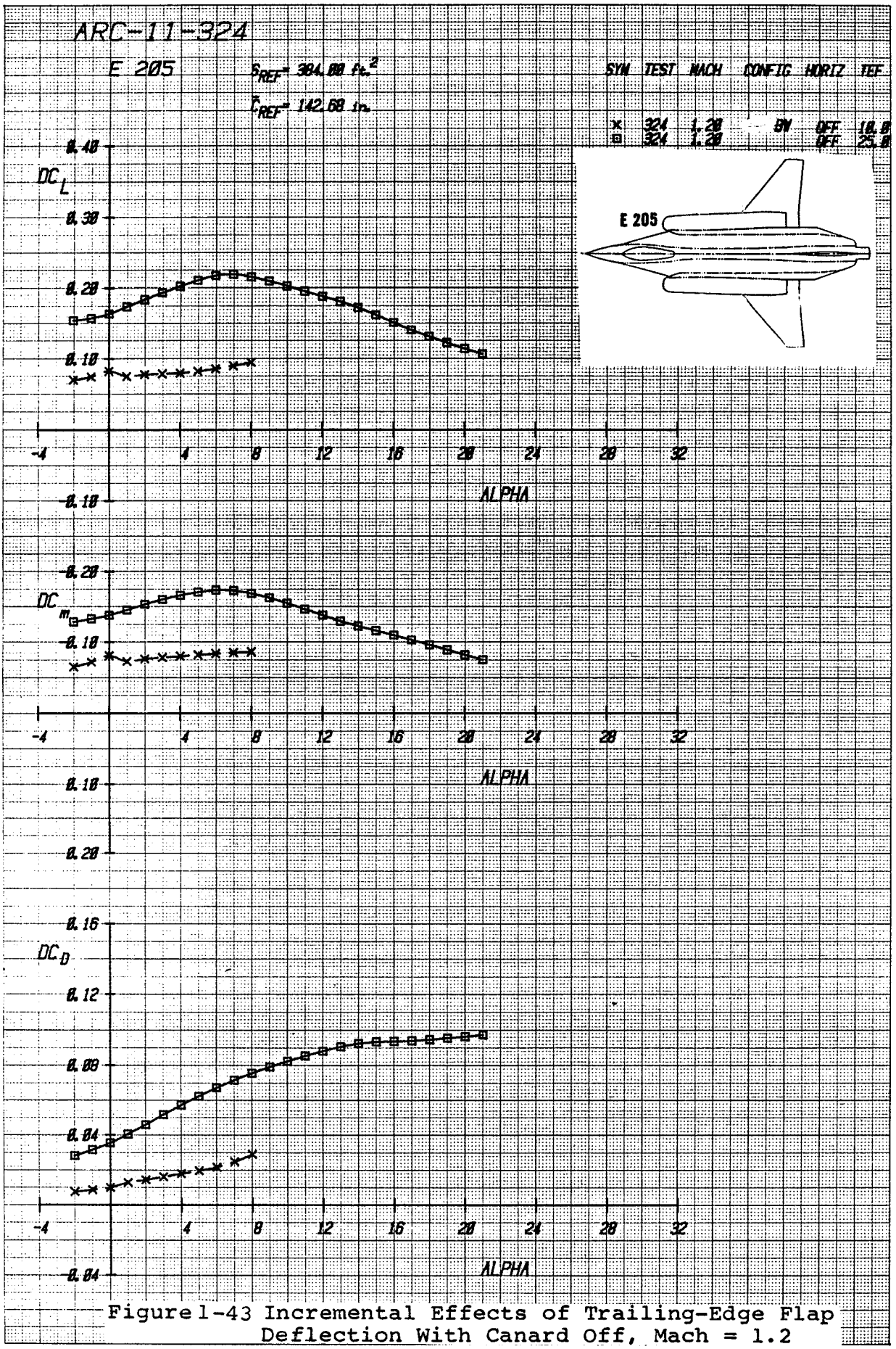

Figure 1-43 Incremental Effects of Trailing-Edge Flap Deflection With Canard Off, Mach = 1.2

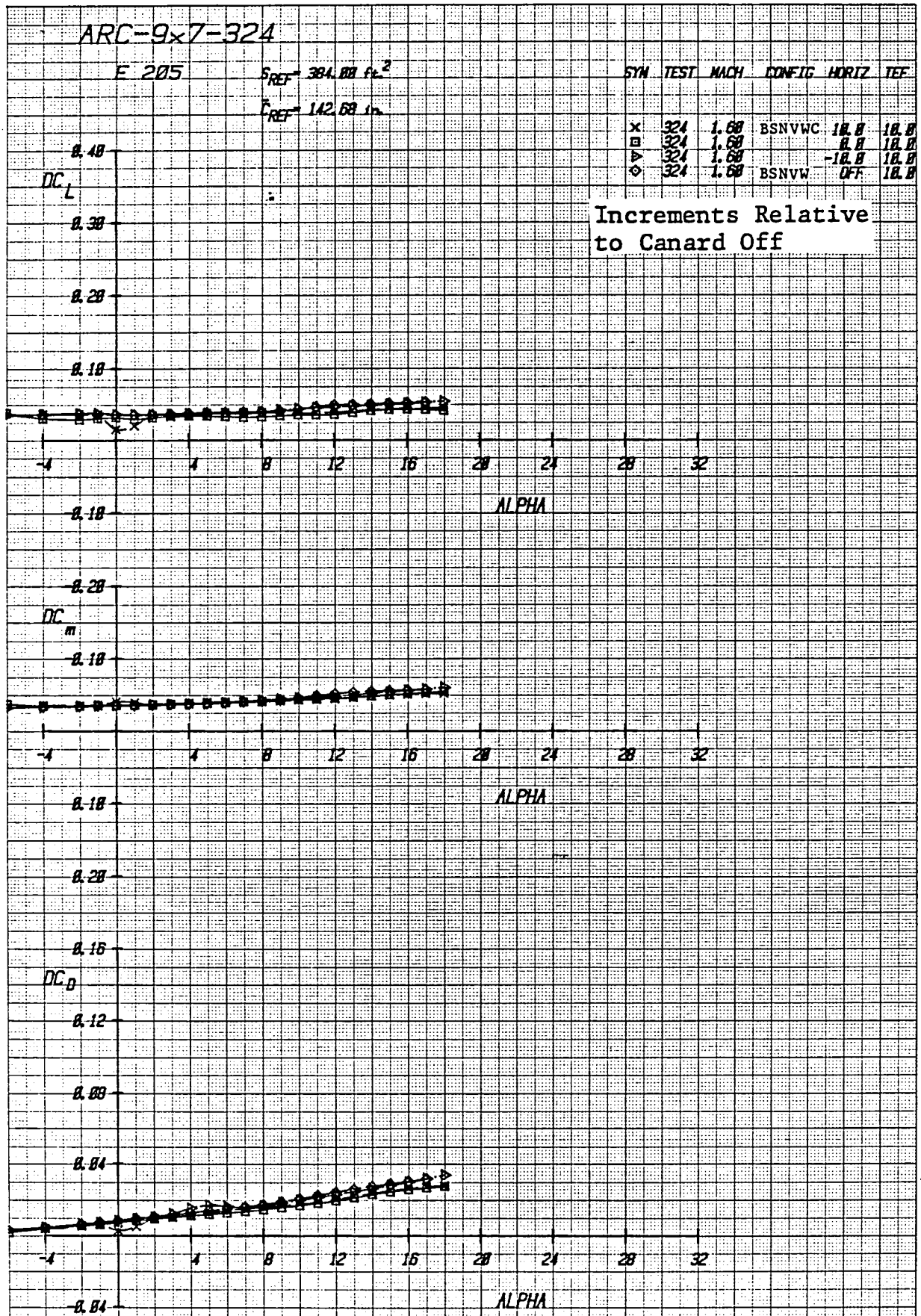

Figure1-44 Incremental Effects of Canard Deflection with Wing Trailing-Edge Flap Deflected +10°, Mach = 1.6

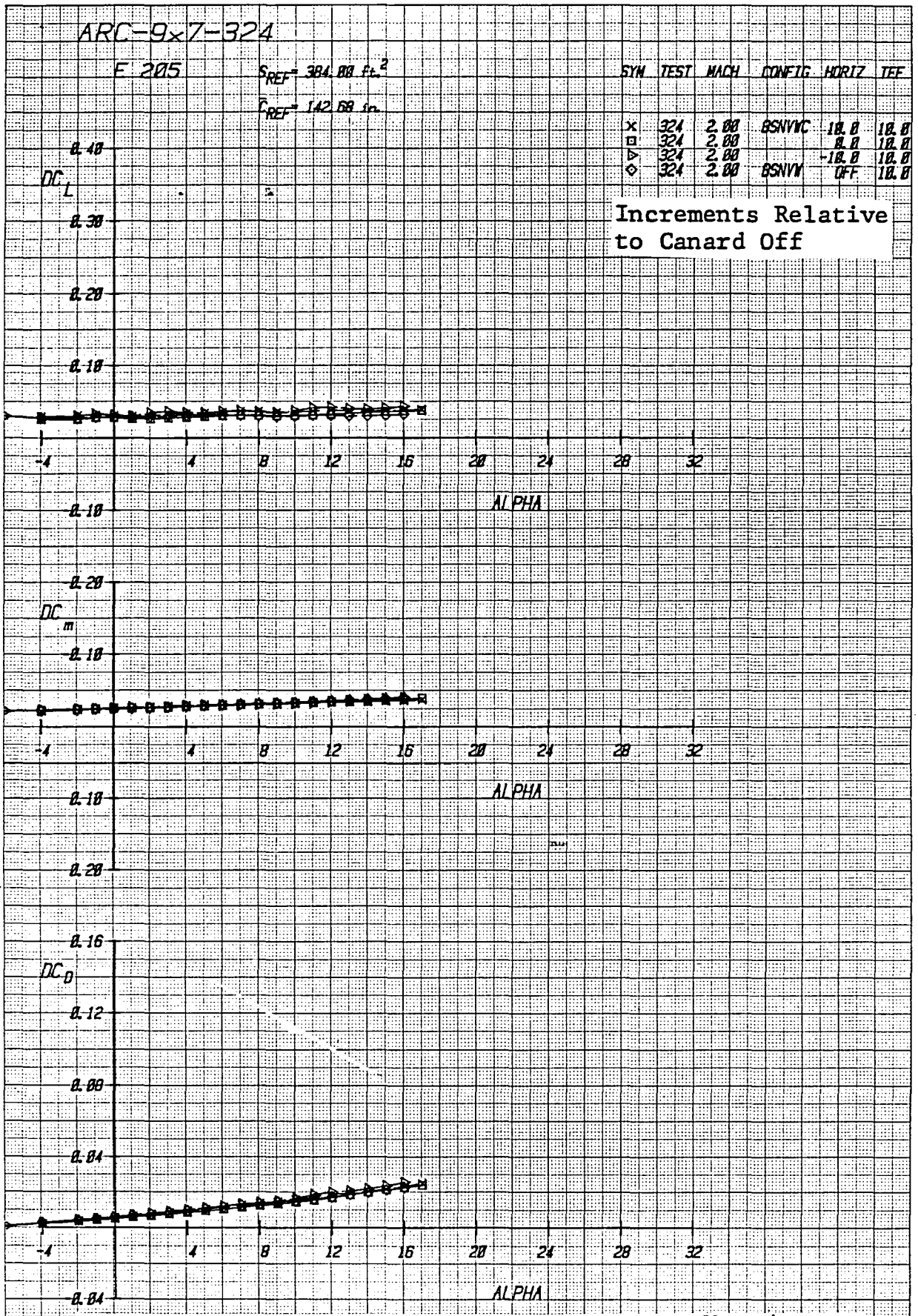

Figure 1-45 Incremental Effects of Canard Deflection with Wing Trailing-Edge Flap Deflected +10°, Mach = 2.0

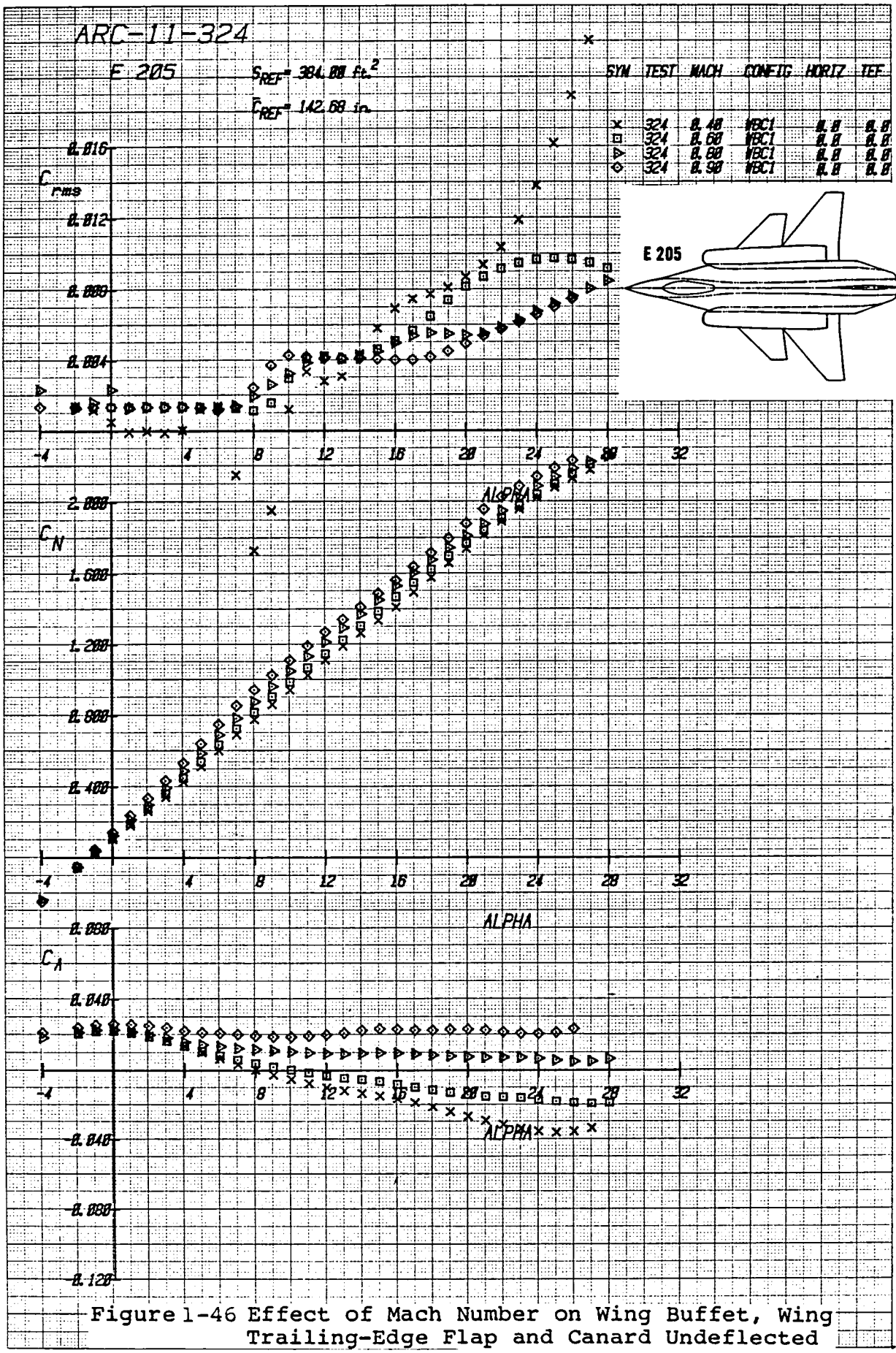

Figure 1-46 Effect of Mach Number on Wing Buffet, Wing Trailing-Edge Flap and Canard Undeflected

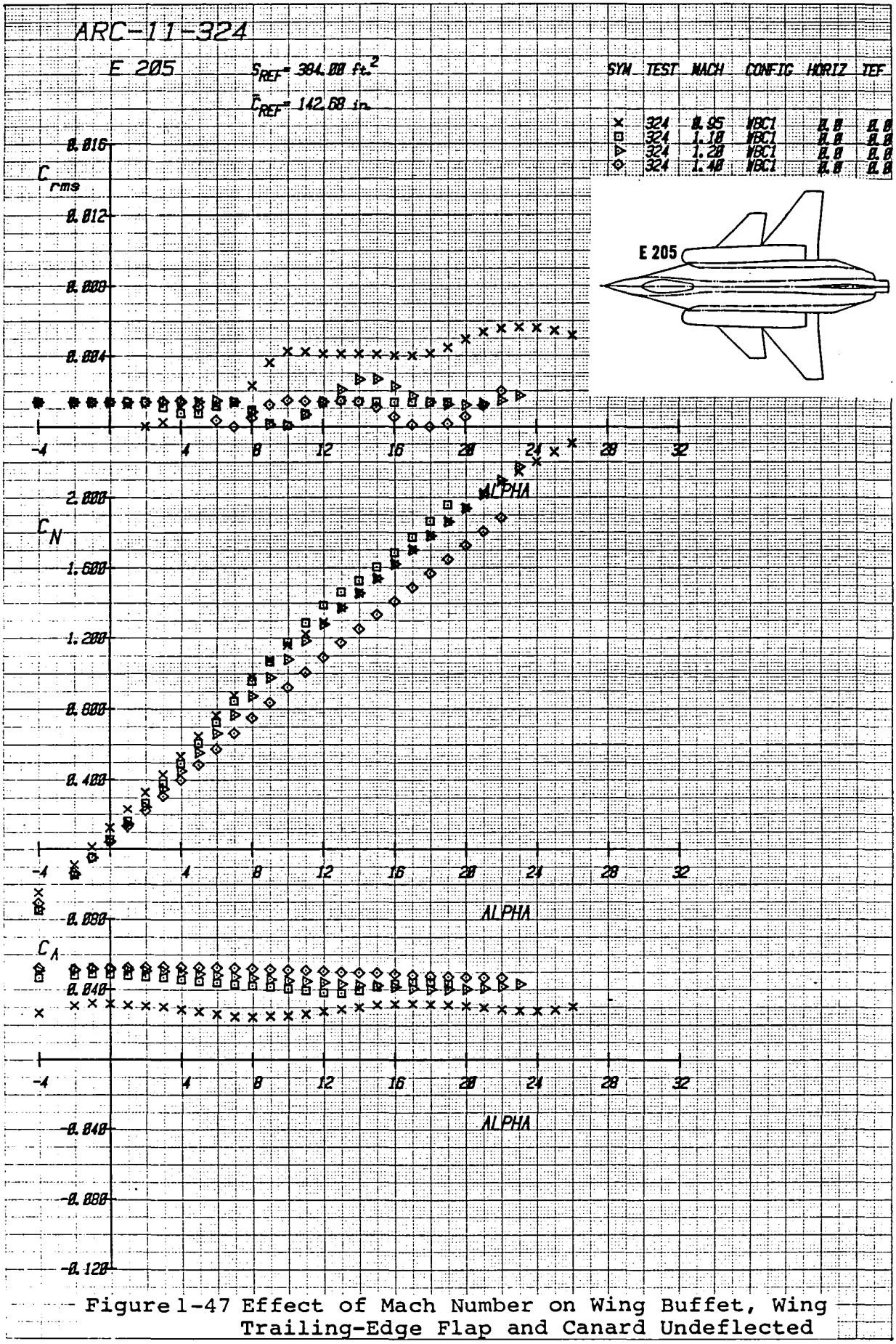

Figure 1-47 Effect of Mach Number on Wing Buffet, Wing Trailing-Edge Flap and Canard Undeflected

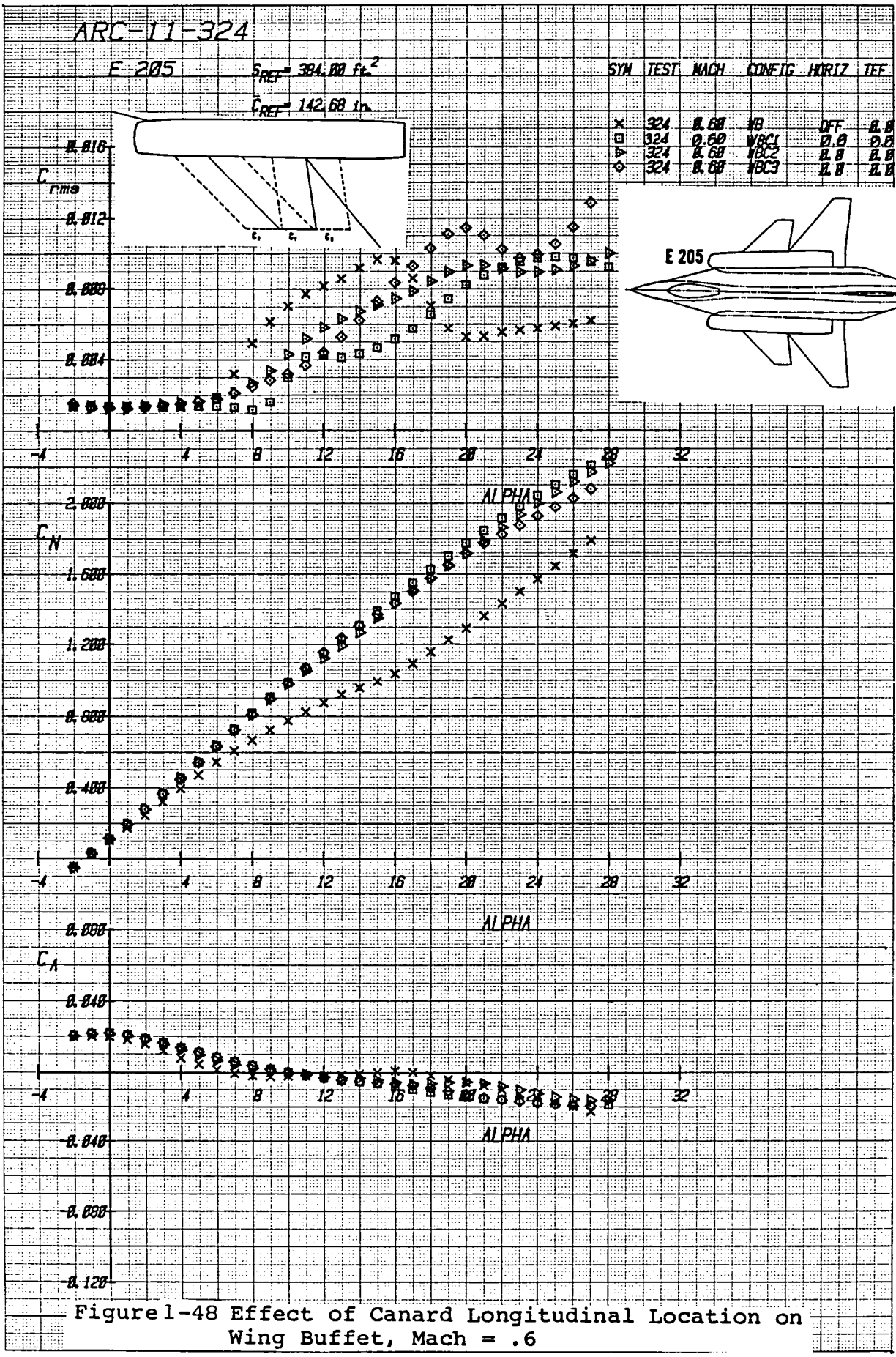

Figure 1-48 Effect of Canard Longitudinal Location on Wing Buffet, Mach = .6

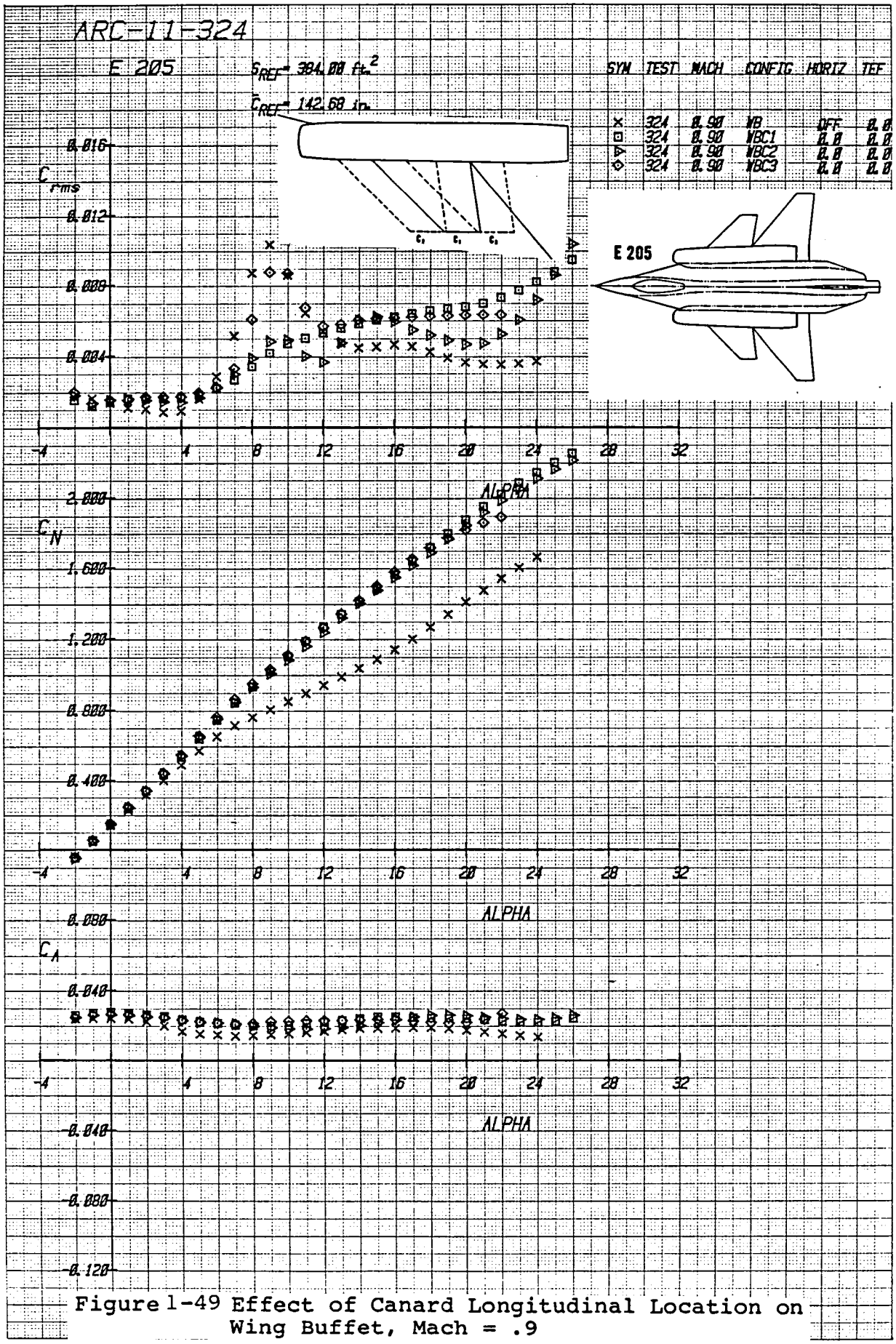

Figure 1-49 Effect of Canard Longitudinal Location on Wing Buffet, Mach = .9

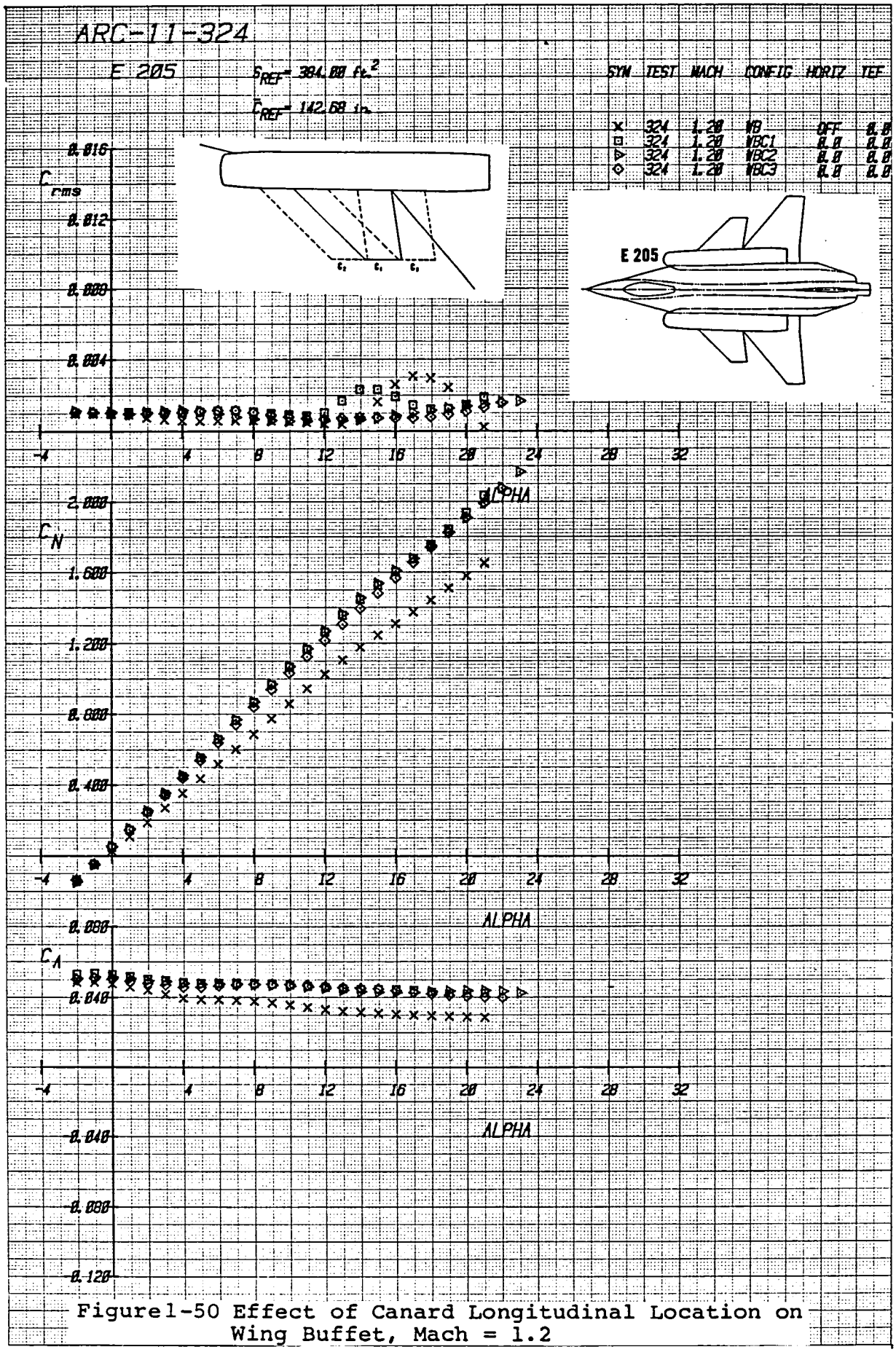

Figure1-50 Effect of Canard Longitudinal Location on Wing Buffet, Mach = 1.2

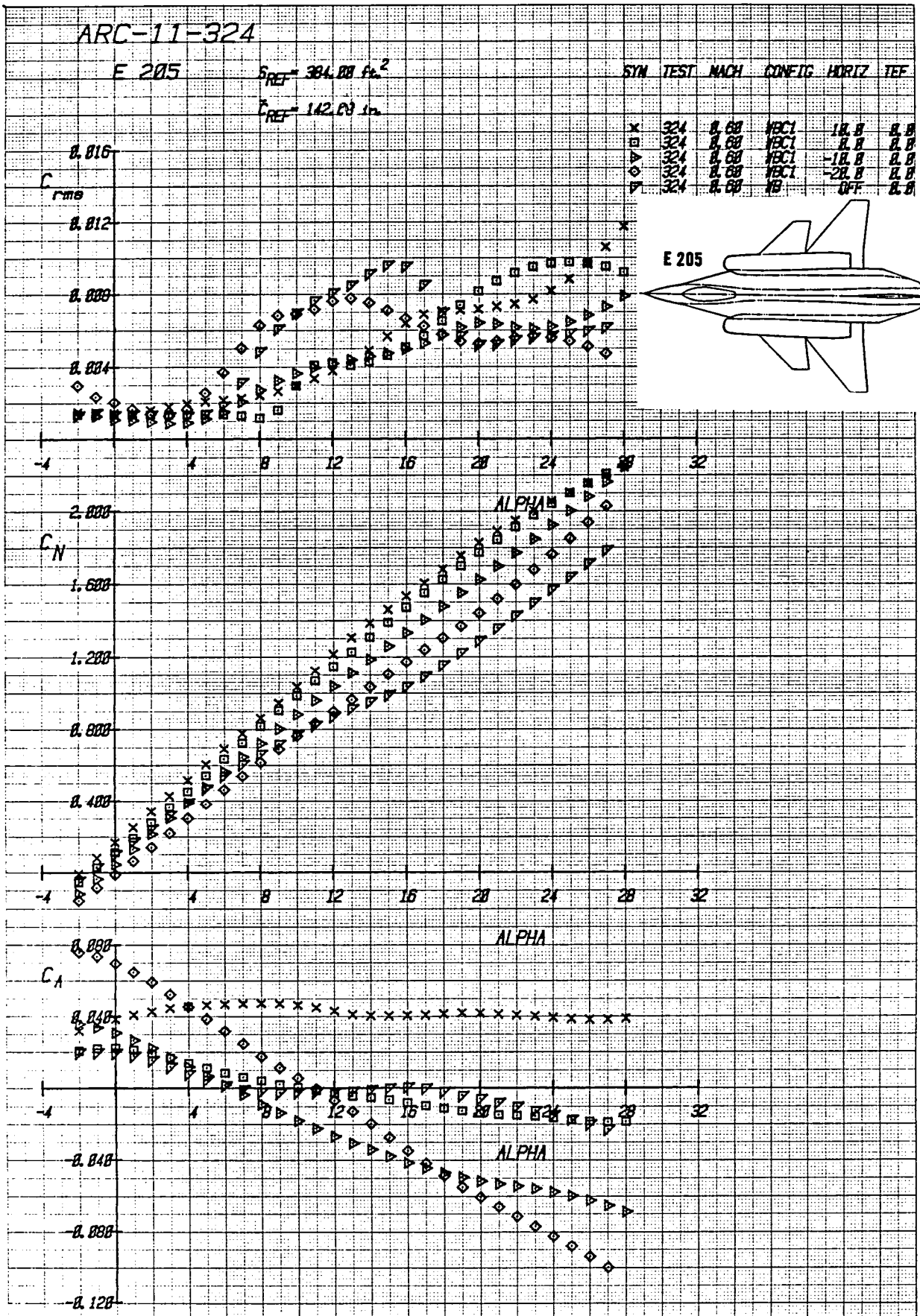

Figure 1-51 Effect of Canard Deflection on Wing Buffet, Mach = .6

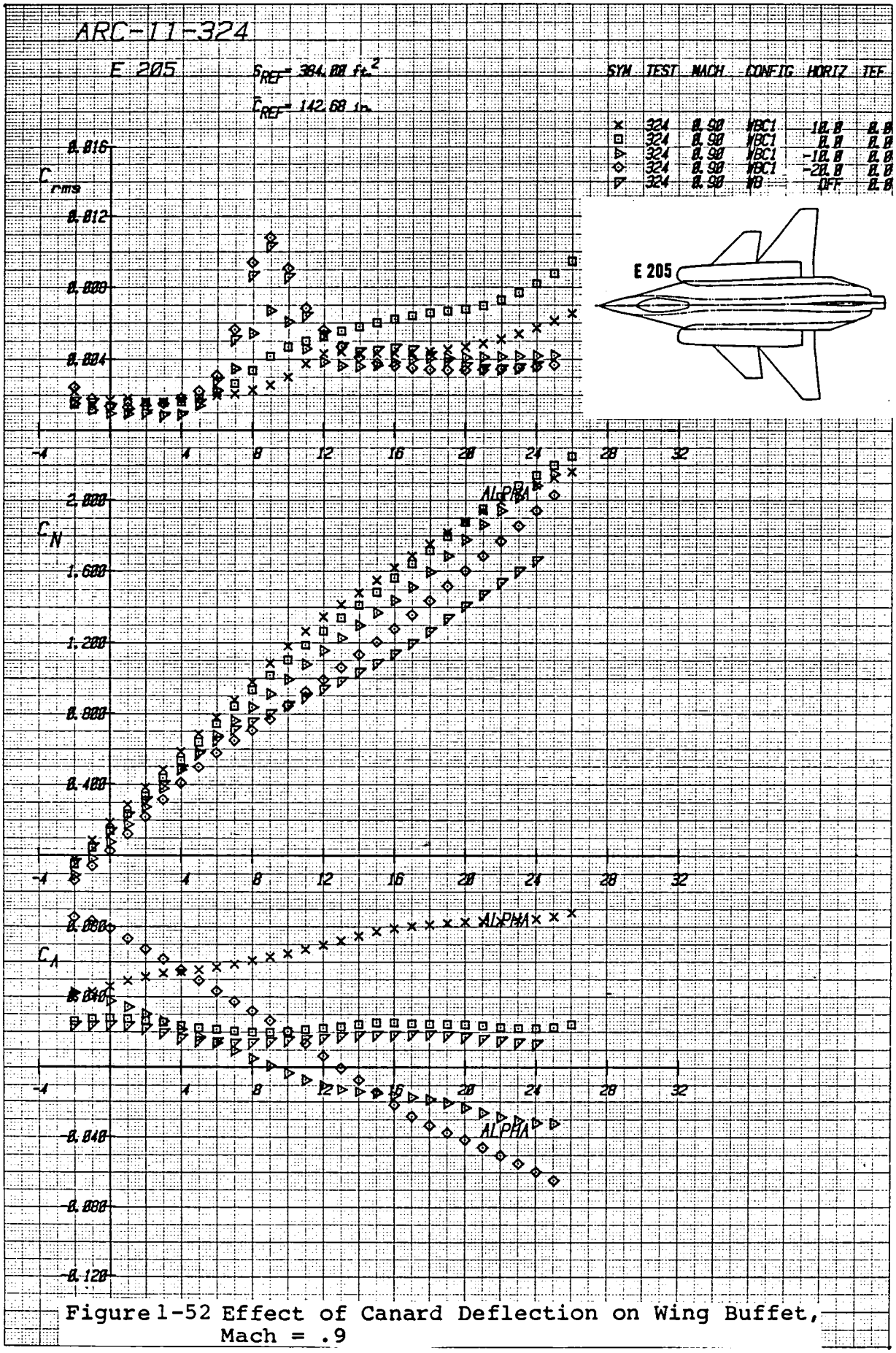

Figure 1-52 Effect of Canard Deflection on Wing Buffet, Mach = .9

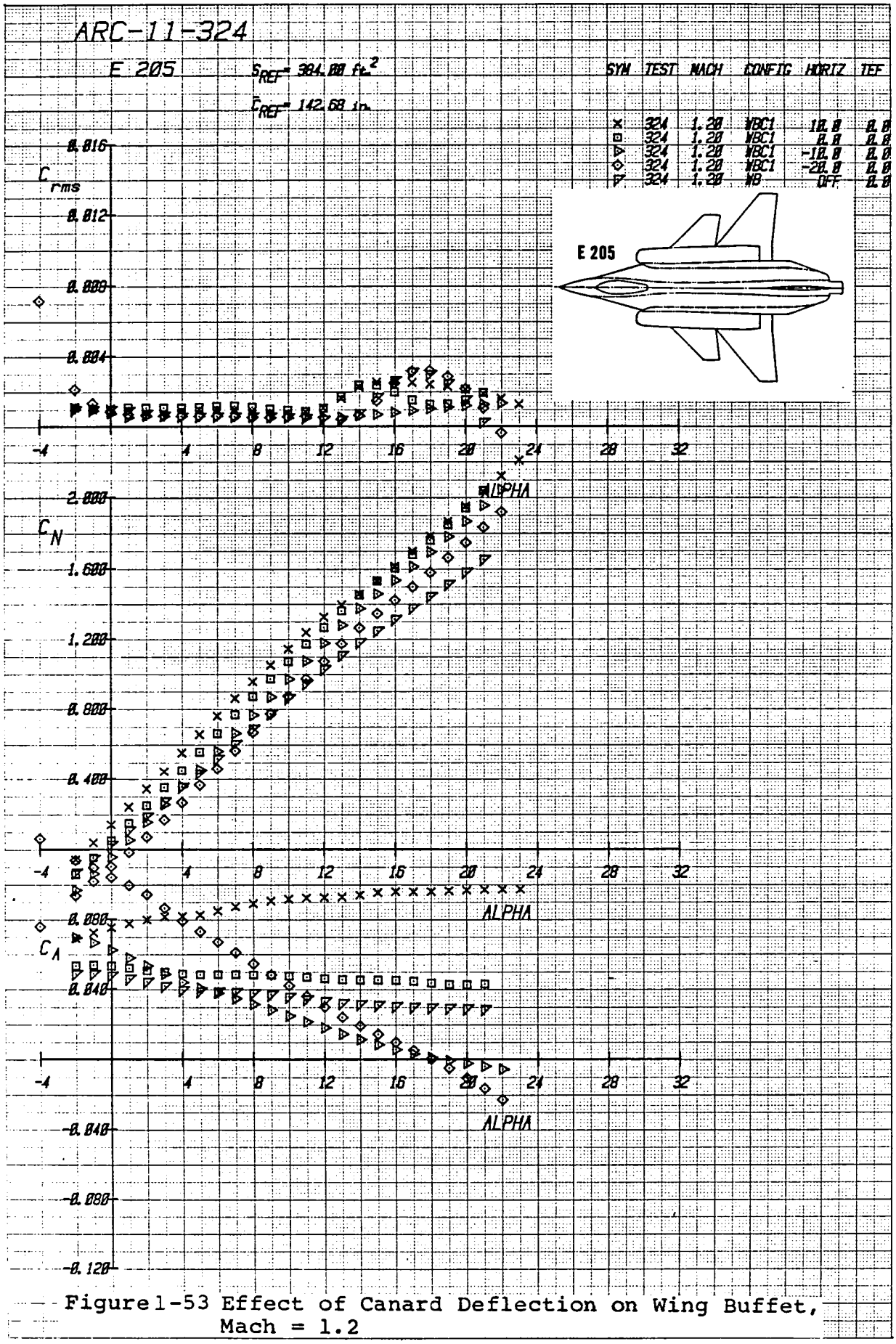

Figure 1-53 Effect of Canard Deflection on Wing Buffet, Mach = 1.2

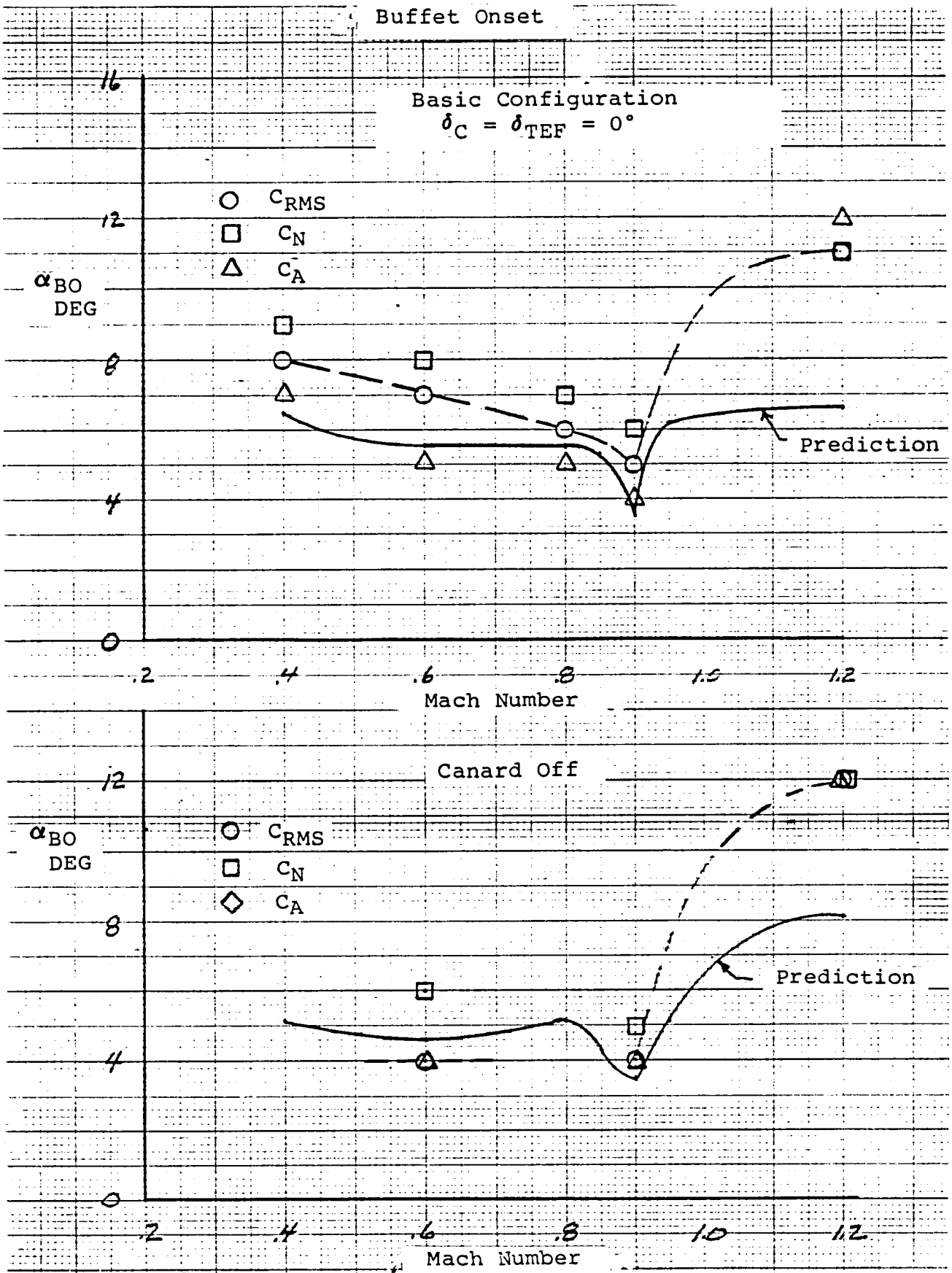

Figure 1-54 Comparison of Predicted-$\alpha_{B.O.}$ with $\alpha_{B.O.}$ - Indicators C_{RMS}, C_N, and C_A from Test Data

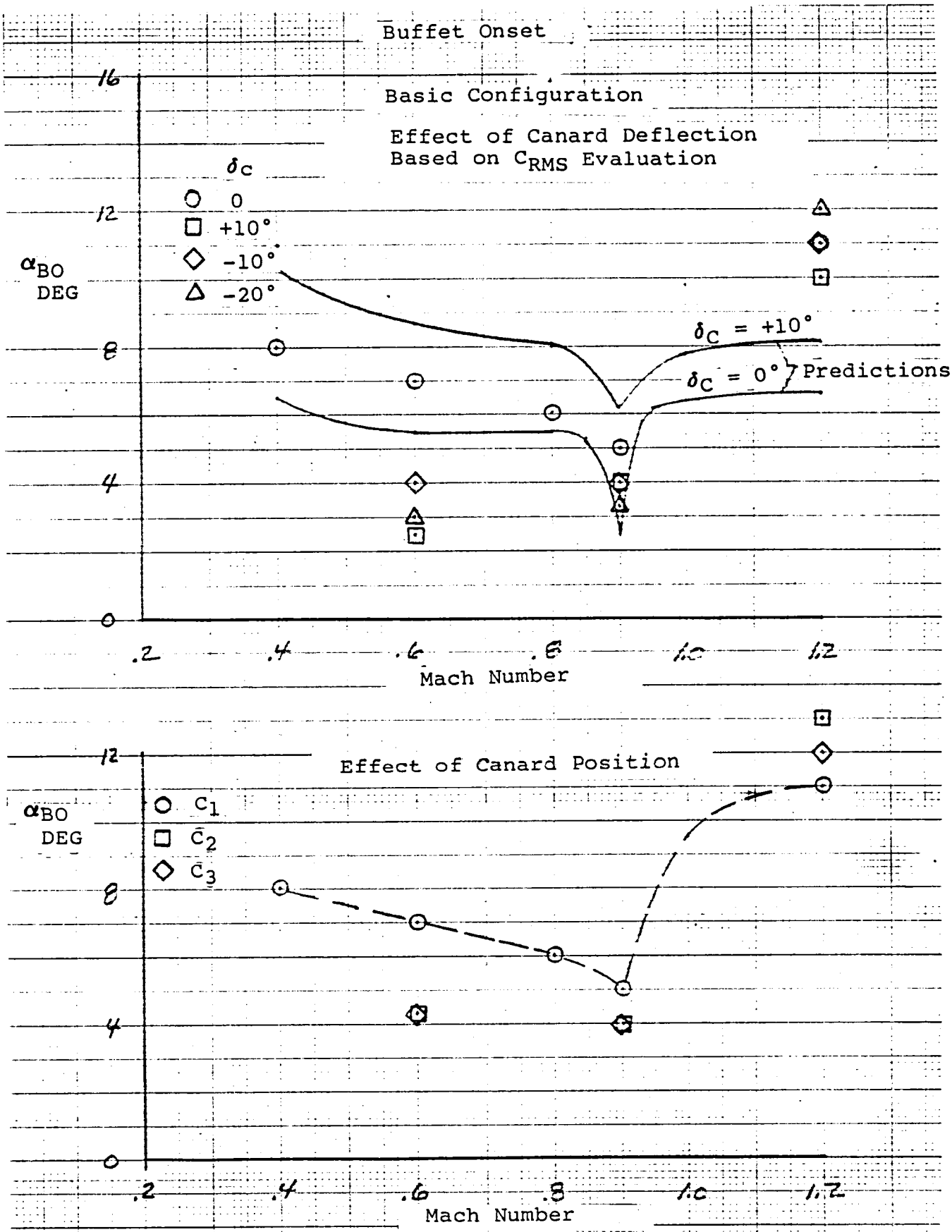

Figure 1-55 Effect of Canard Deflection and Canard Location on $\alpha_{B.O.}$

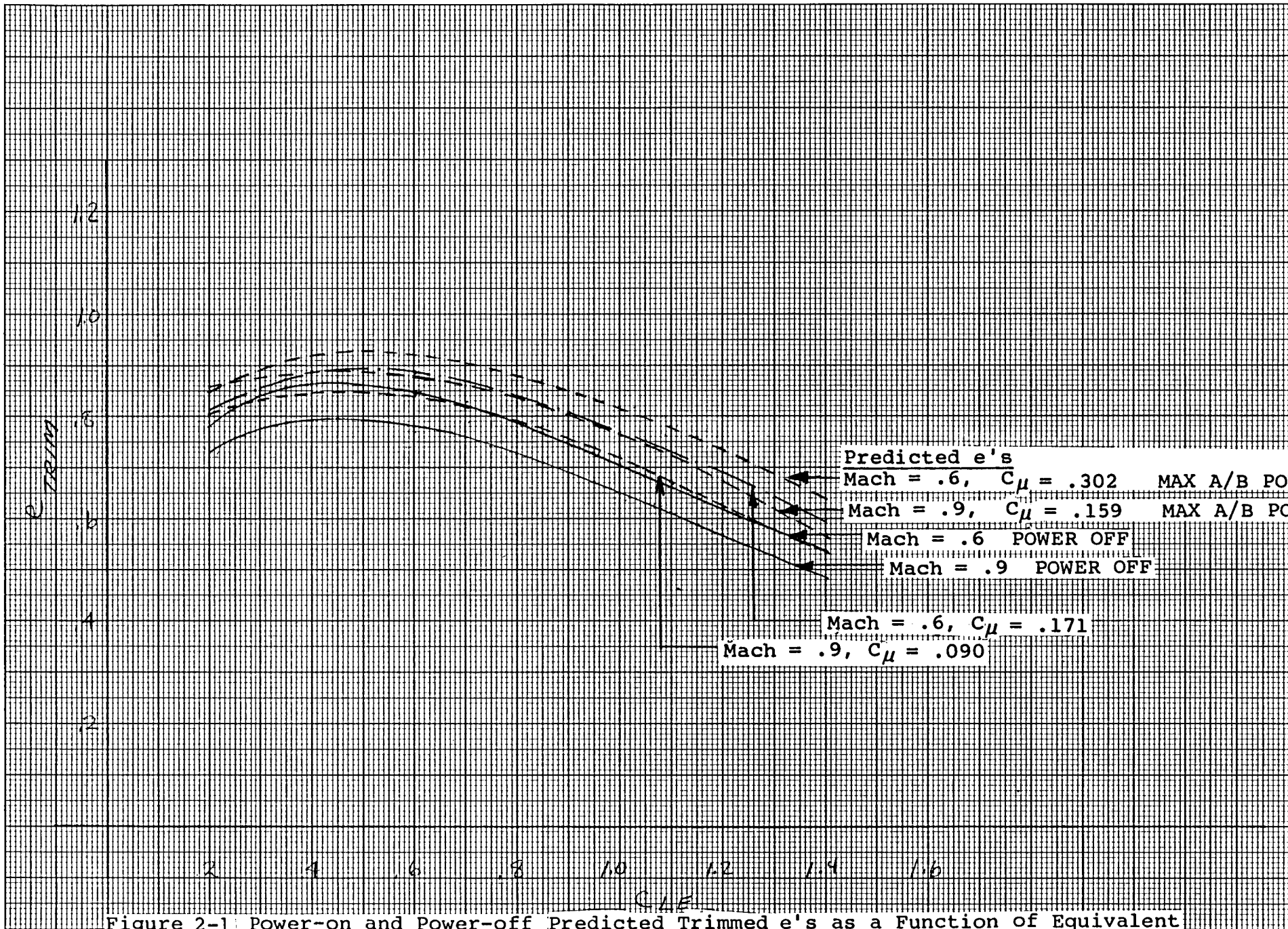

Figure 2-1 Power-on and Power-off Predicted Trimmed e's as a Function of Equivalent Lift Coefficient, C_{LE}, Mach Number, and C_μ (from Reference 1)

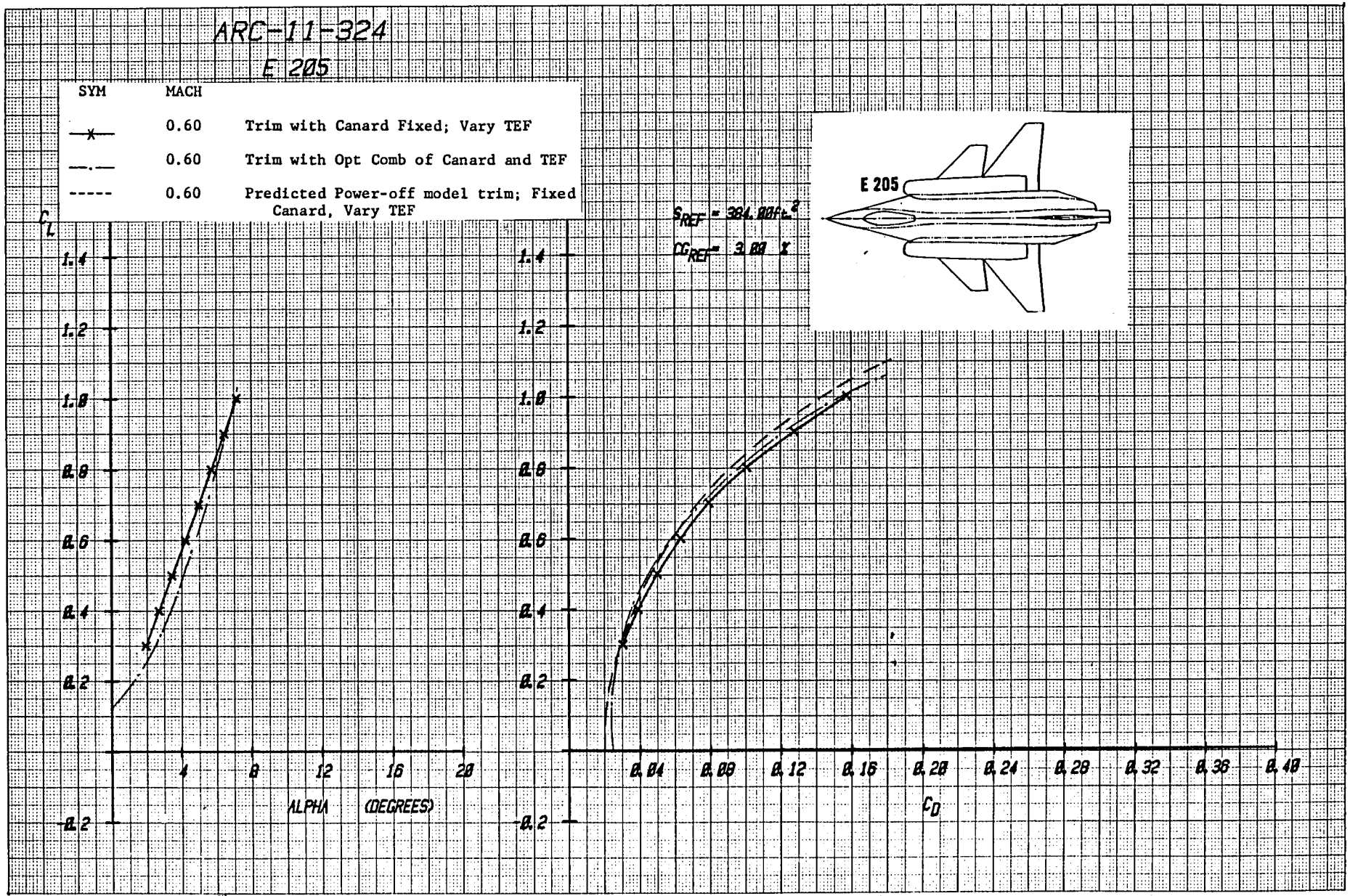

Figure 2-2 Trimmed Lift and Drag with Wing Trailing-Edge Flap Deflections and Canard Undeflected, Mach = .6

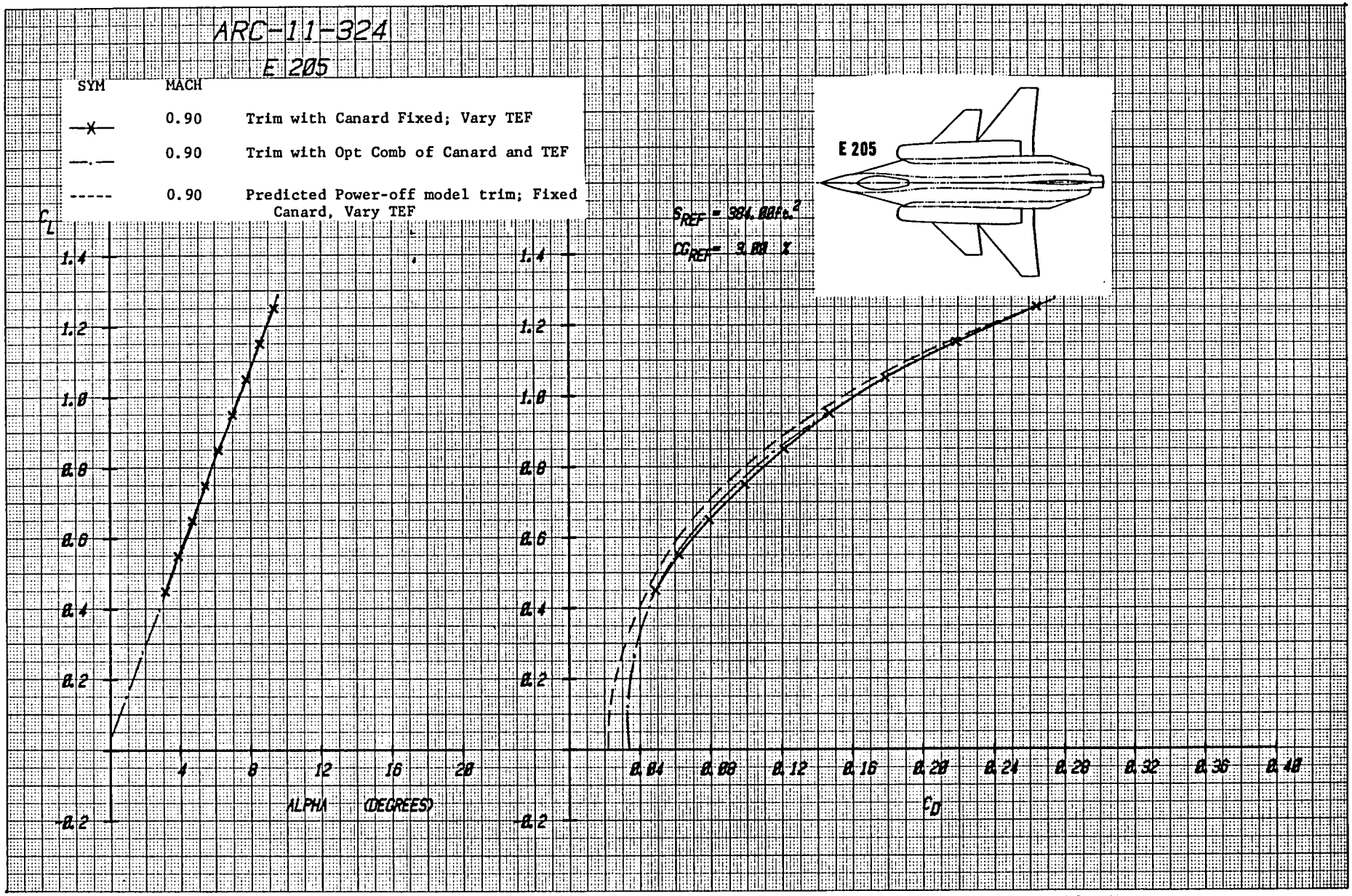

Figure 2-3 Trimmed Lift and Drag with Wing Trailing-Edge Flap Deflections and Canard Undeflected, Mach = .9

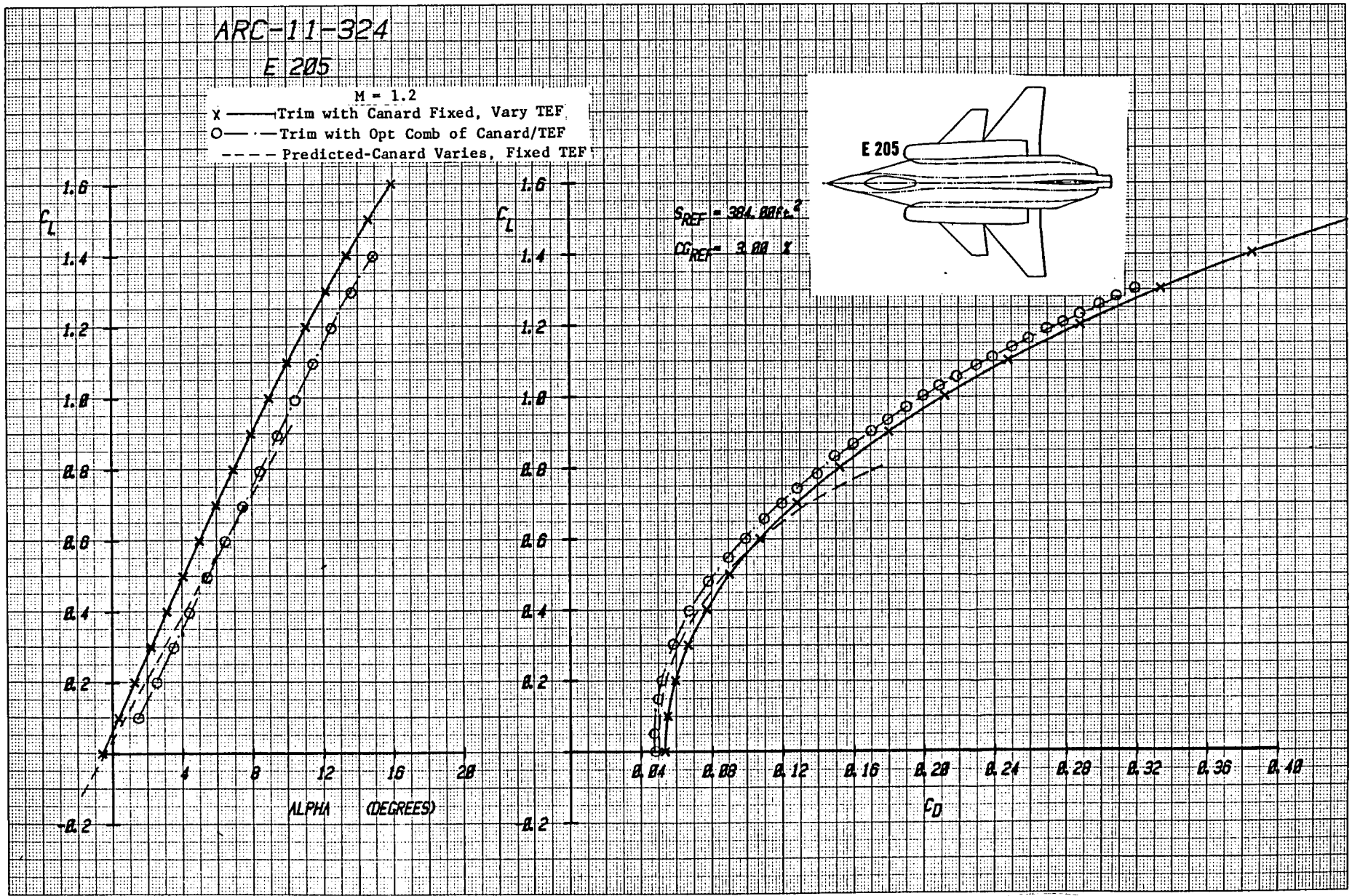

Figure 2-4 Trimmed Lift and Drag with Wing Trailing-Edge Flap Deflection and Canard Undeflected, Mach = 1.2

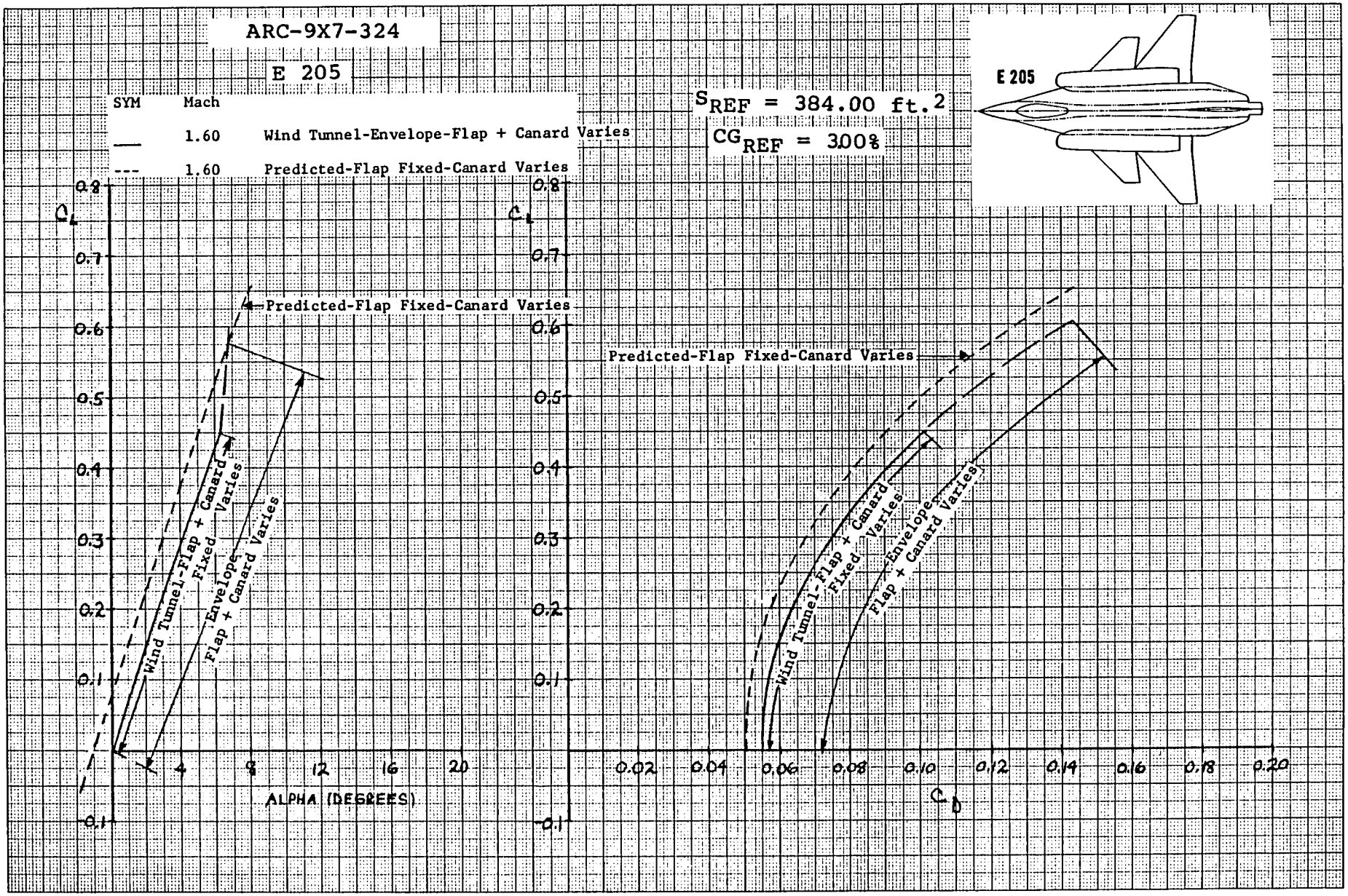

Figure 2-5 Comparison of Power-off Trimmed Lift Curves and Drag Polars for Trimming with Flap-Fixed, Canard Varies and with an Envelope of Optimum Canard and Flap Deflections, Mach = 1.6

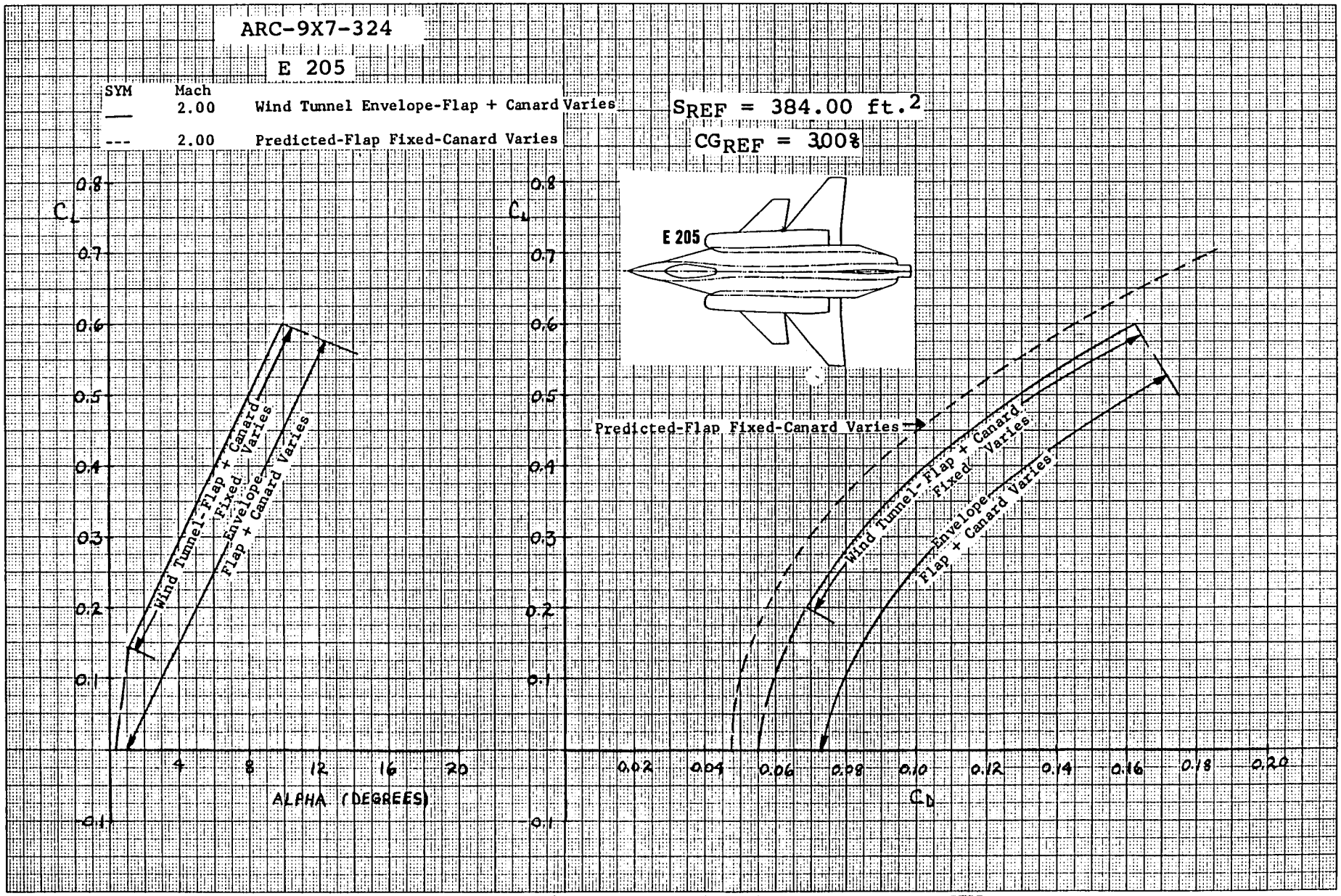

Figure 2-6 Comparison of Power-off Trimmed Lift Curves and Drag Polars for Trimming with Flap-Fixed, Canard Varies and with an Envelope of Optimum Canard and Flap Deflections, Mach = 2.0

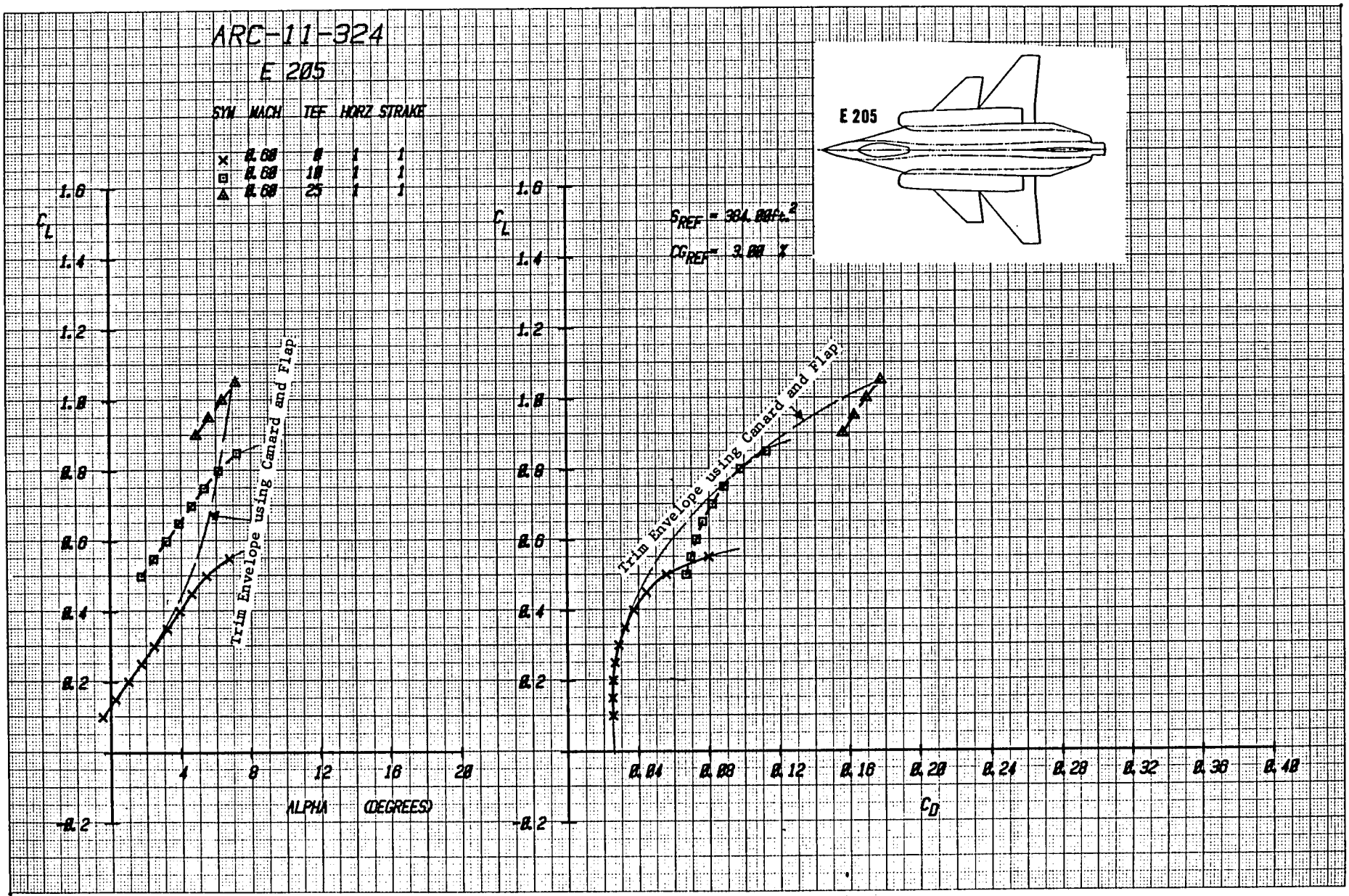

Figure 2-7 Trimmed Lift and Drag for Baseline E205 Configuration Using Canard and Trailing-Edge Flap Deflections, Mach = .6

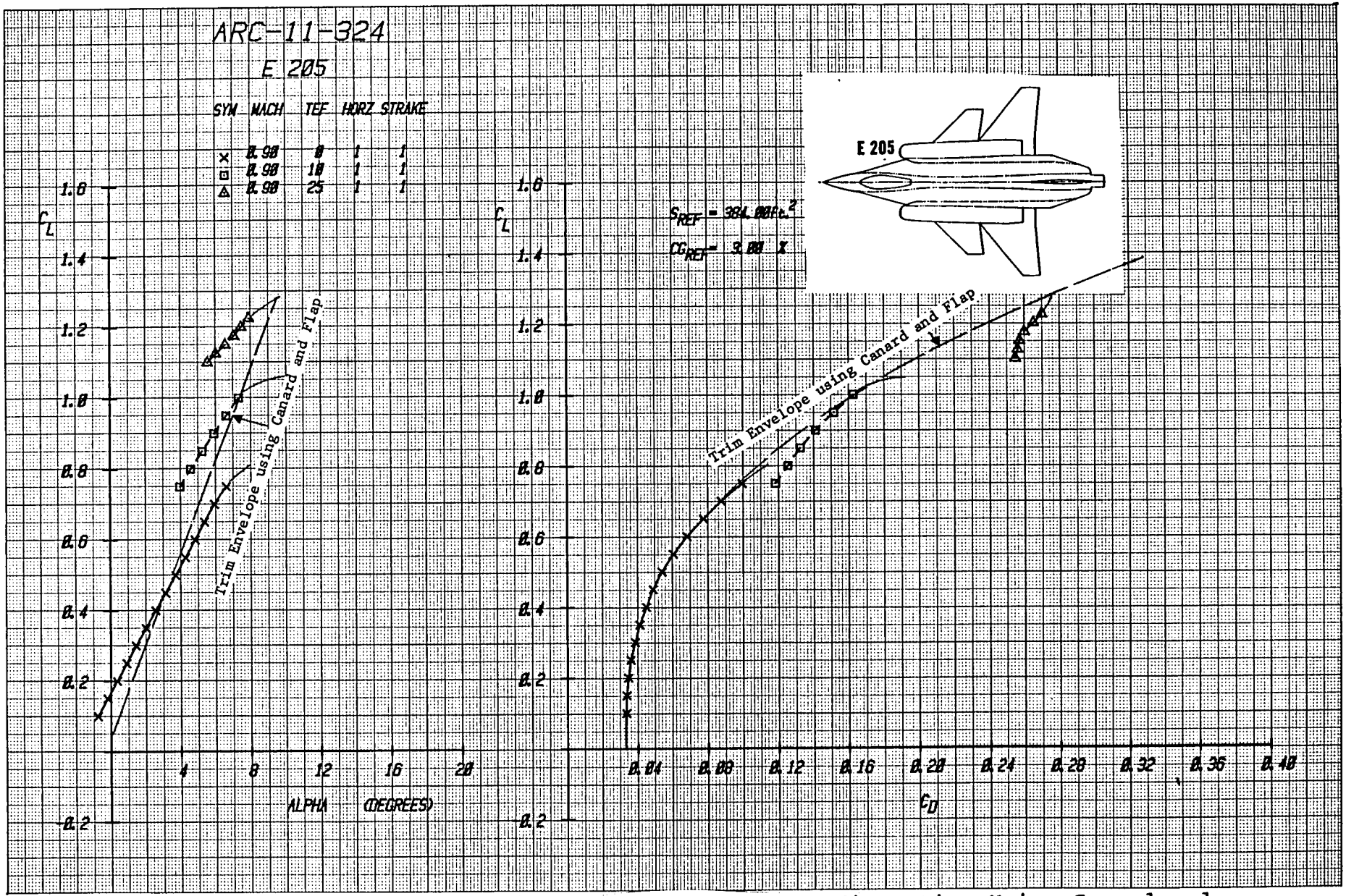

Figure 2-8 Trimmed Lift and Drag for Baseline E205 Configuration Using Canard and Trailing-Edge Flap Deflections, Mach = .9

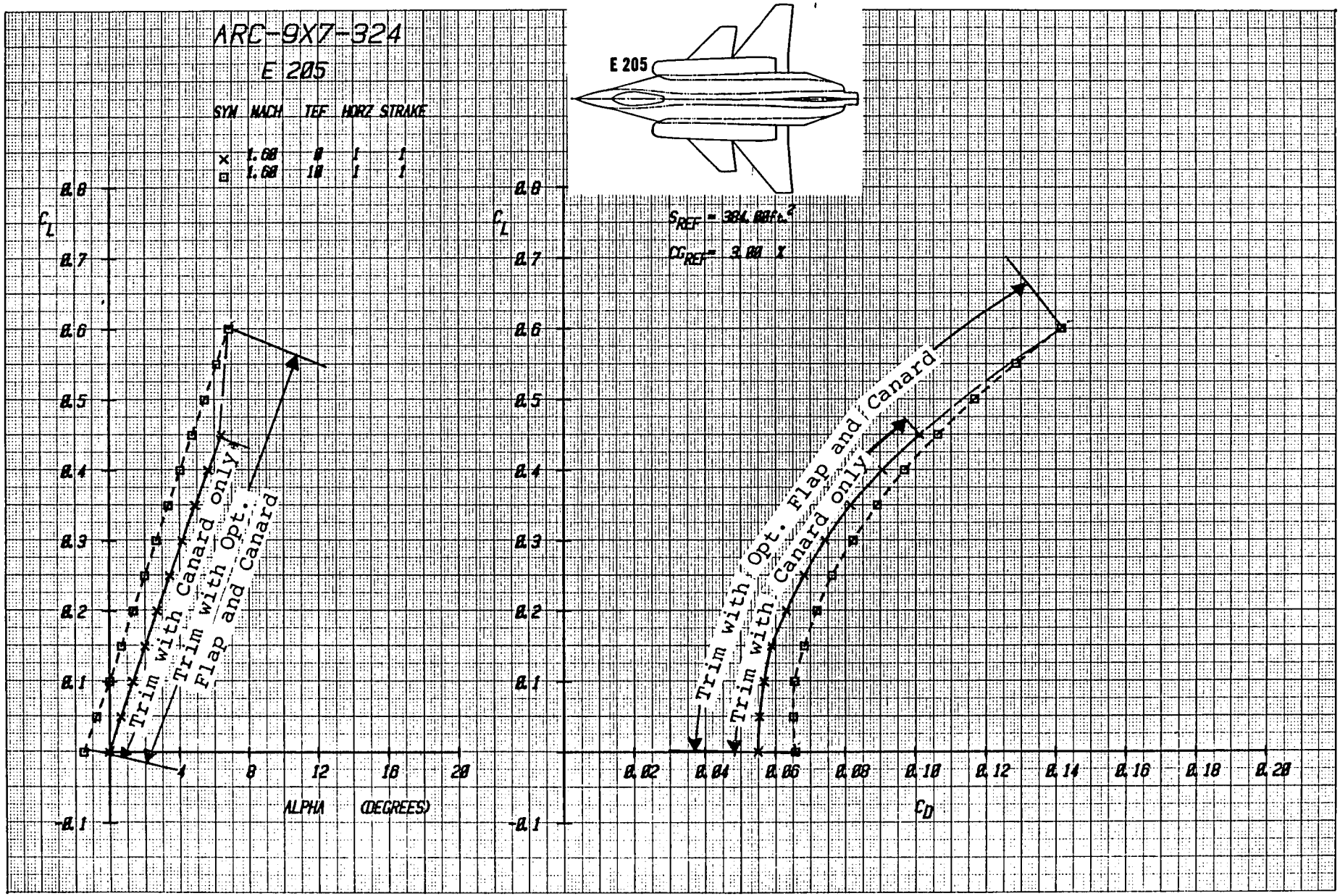

Figure 2-9 Development of Envelope Trimmed Lift Curve and Drag Polar, Mach = 1.6

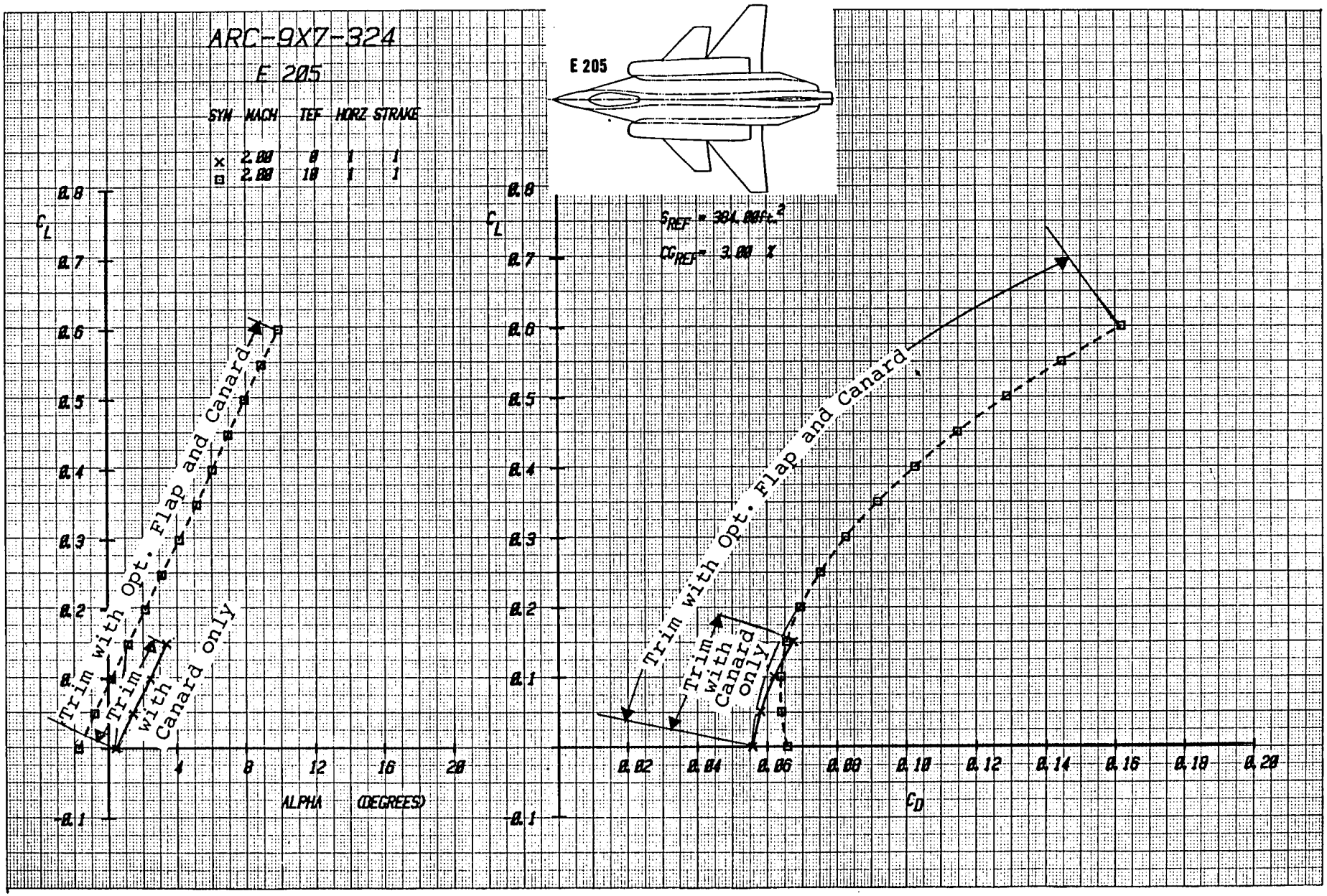

Figure 2-10 Development of Envelope Trimmed Lift Curve and Drag Polar, Mach = 2.0

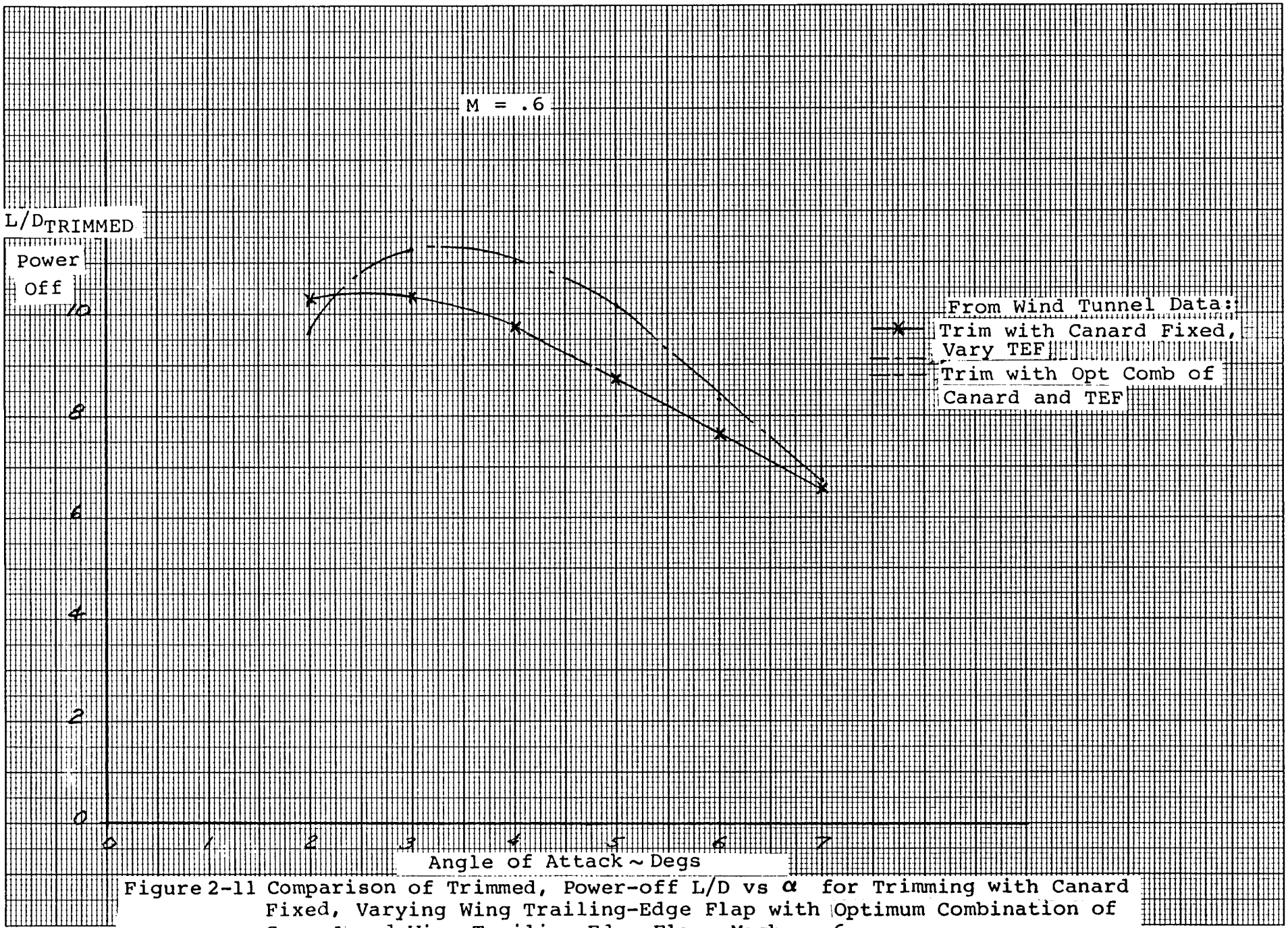

Figure 2-11 Comparison of Trimmed, Power-off L/D vs α for Trimming with Canard Fixed, Varying Wing Trailing-Edge Flap with Optimum Combination of Canard and Wing Trailing-Edge Flap, Mach = .6

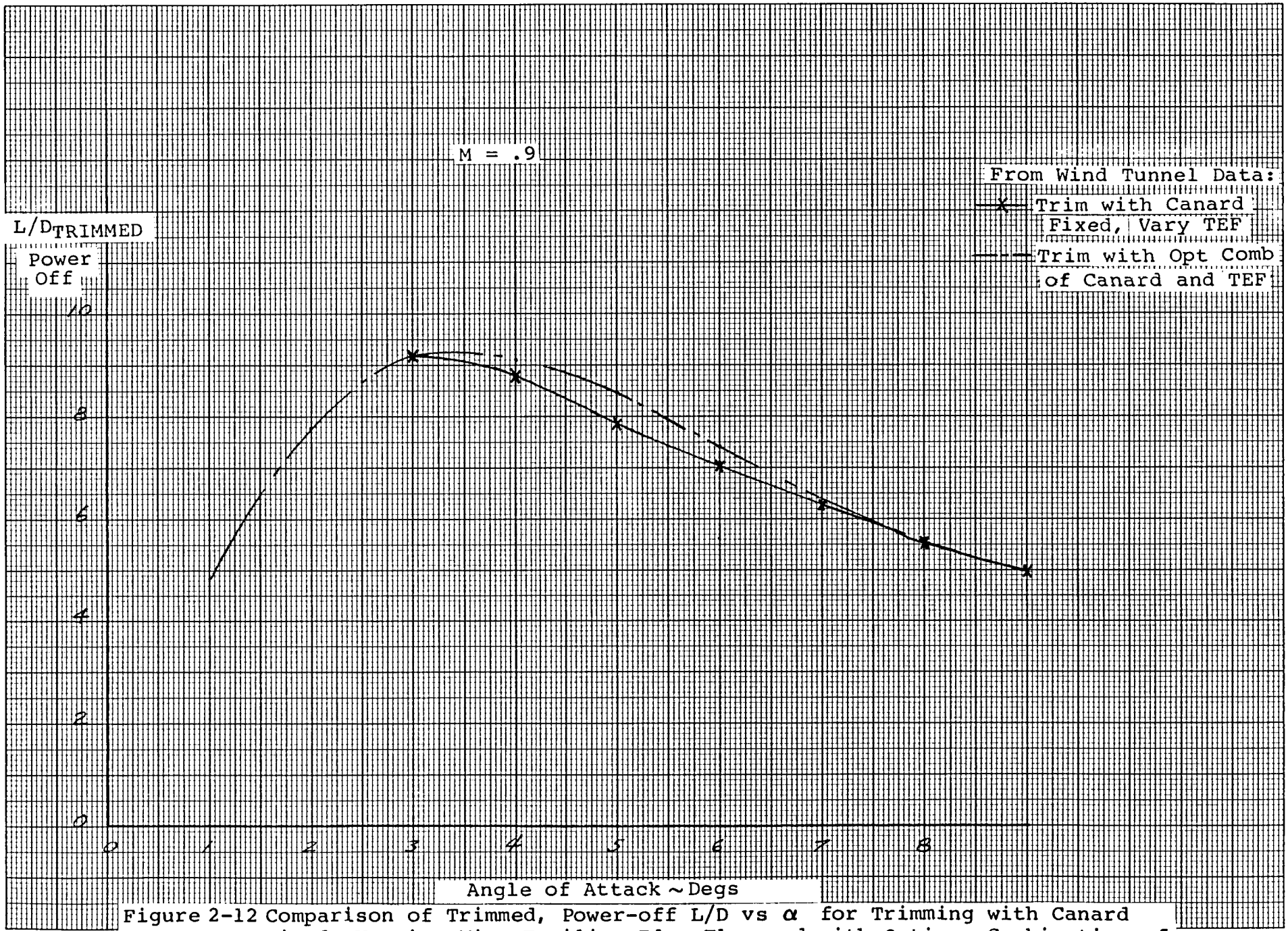

Figure 2-12 Comparison of Trimmed, Power-off L/D vs α for Trimming with Canard Fixed, Varying Wing Trailing-Edge Flap and with Optimum Combination of Canard and Wing Trailing-Edge Flap, Mach = .9

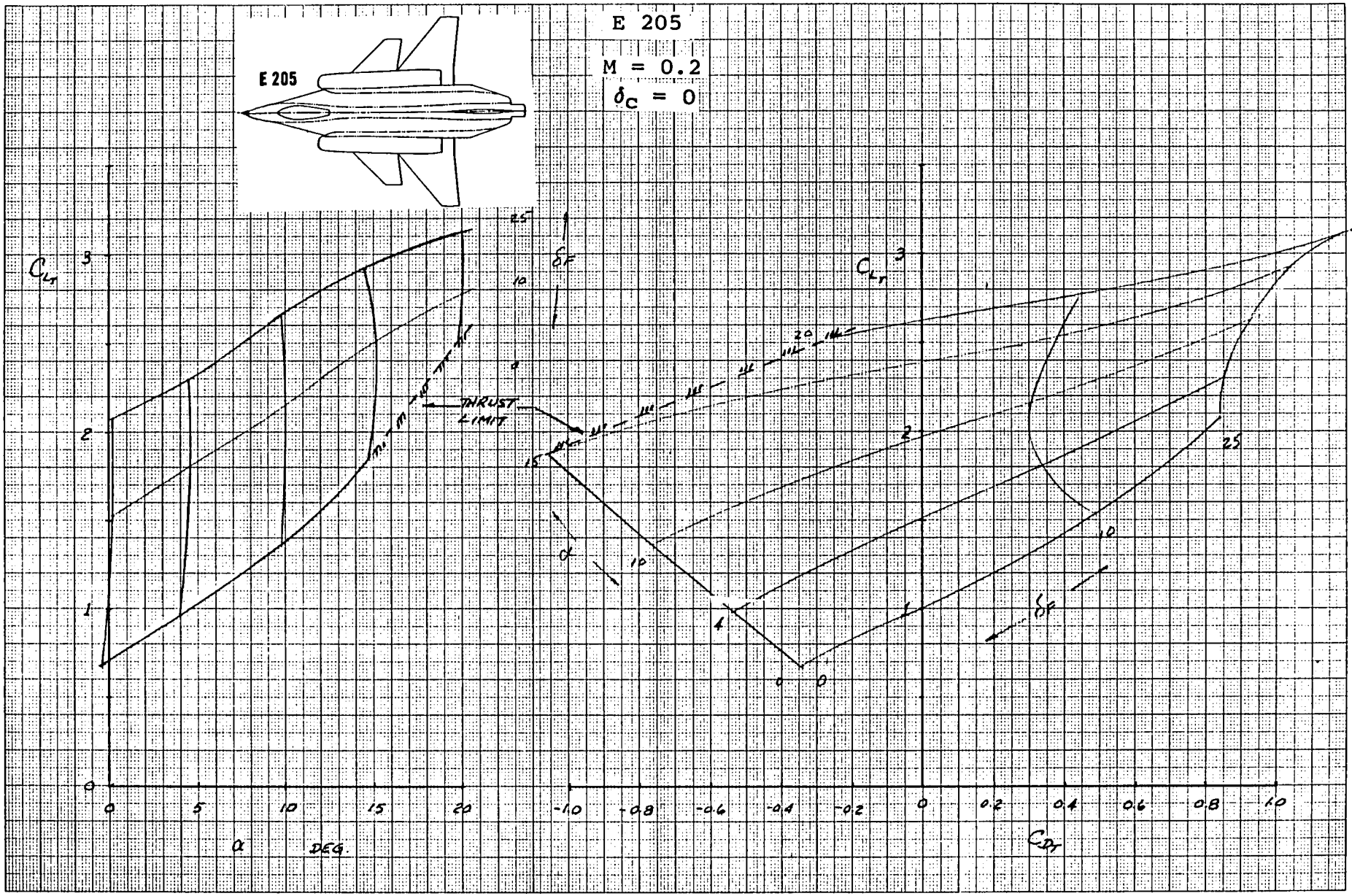

Figure 2-13 Full-Scale E205 Airplane Predicted, Power-on, Trimmed Lift Curve- and Drag Polar- Envelopes for M = .2, $C_{T_{TOTAL}}$ = 1.81

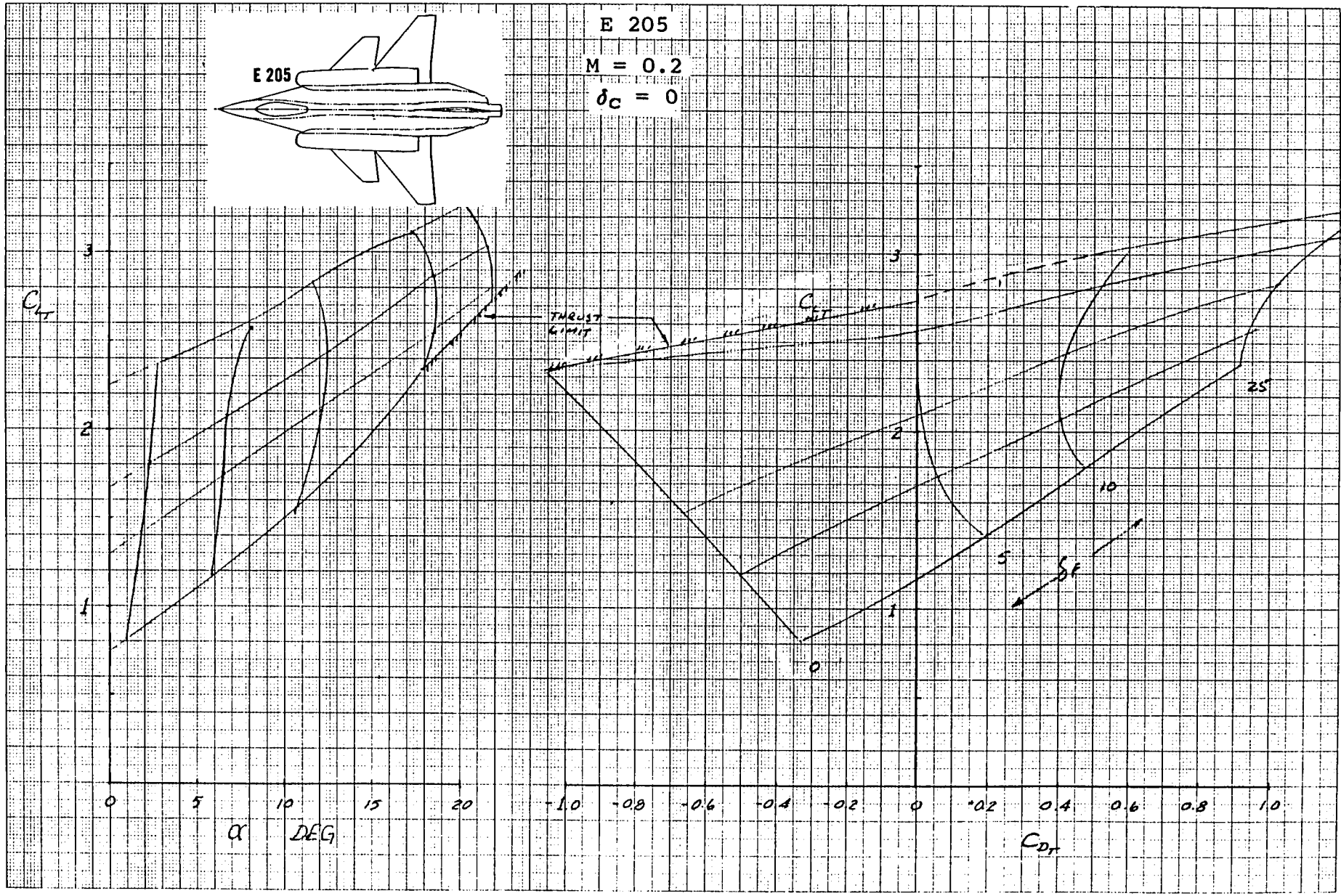

Figure 2-14 Full-Scale E205 Airplane Power-on, Trimmed Lift Curve- and Drag Polar-Envelopes from Wind Tunnel Data for M = .2, $C_{T_{TOTAL}}$ = 1.81

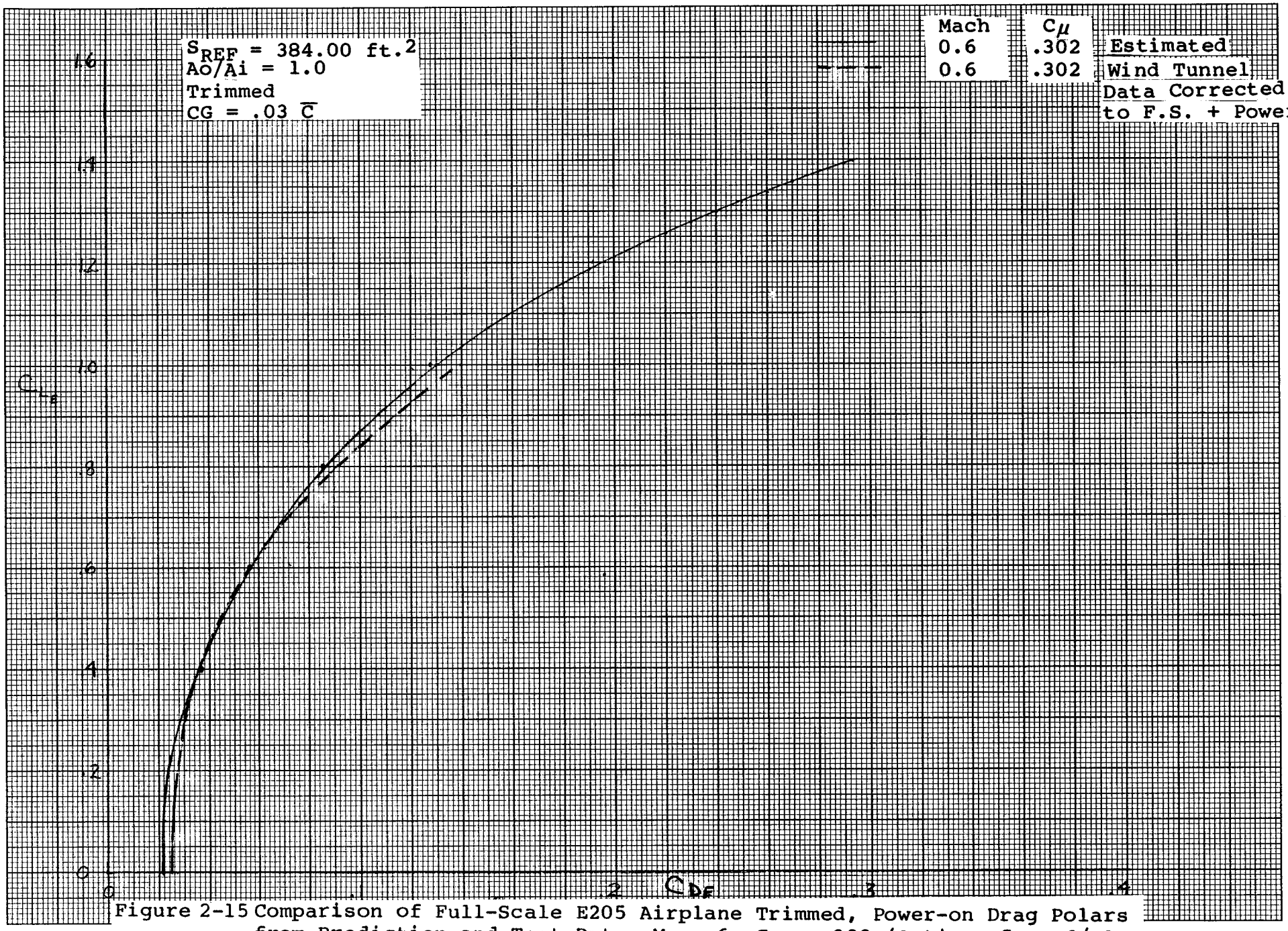

Figure 2-15 Comparison of Full-Scale E205 Airplane Trimmed, Power-on Drag Polars from Prediction and Test Data, M = .6, $C\mu$ = .302 (Optimum Canard/Flap Envelope Trim for Prediction)

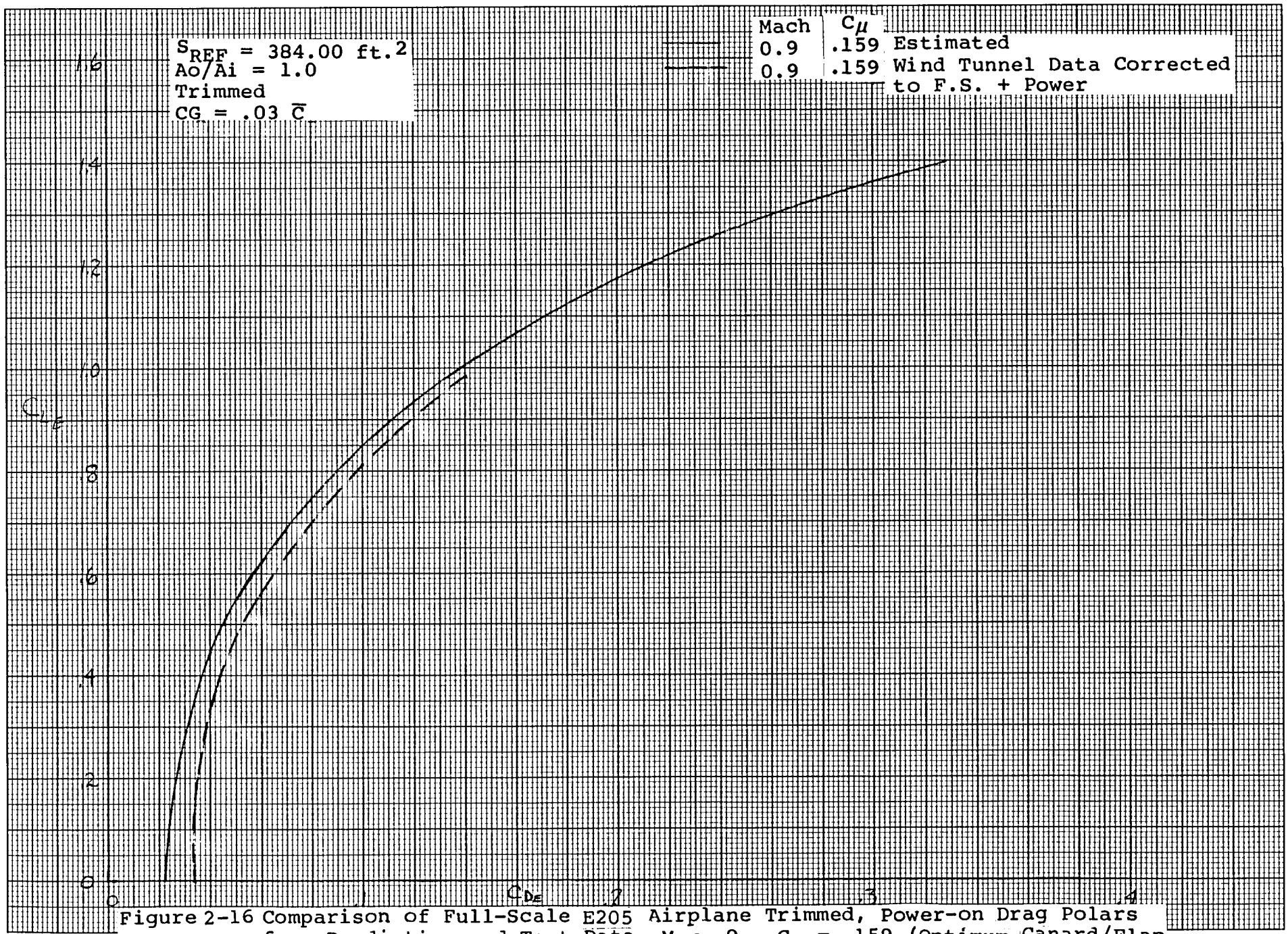

Figure 2-16 Comparison of Full-Scale E205 Airplane Trimmed, Power-on Drag Polars from Prediction and Test Data, M = .9, C_μ = .159 (Optimum Canard/Flap Envelope Trim for Prediction)

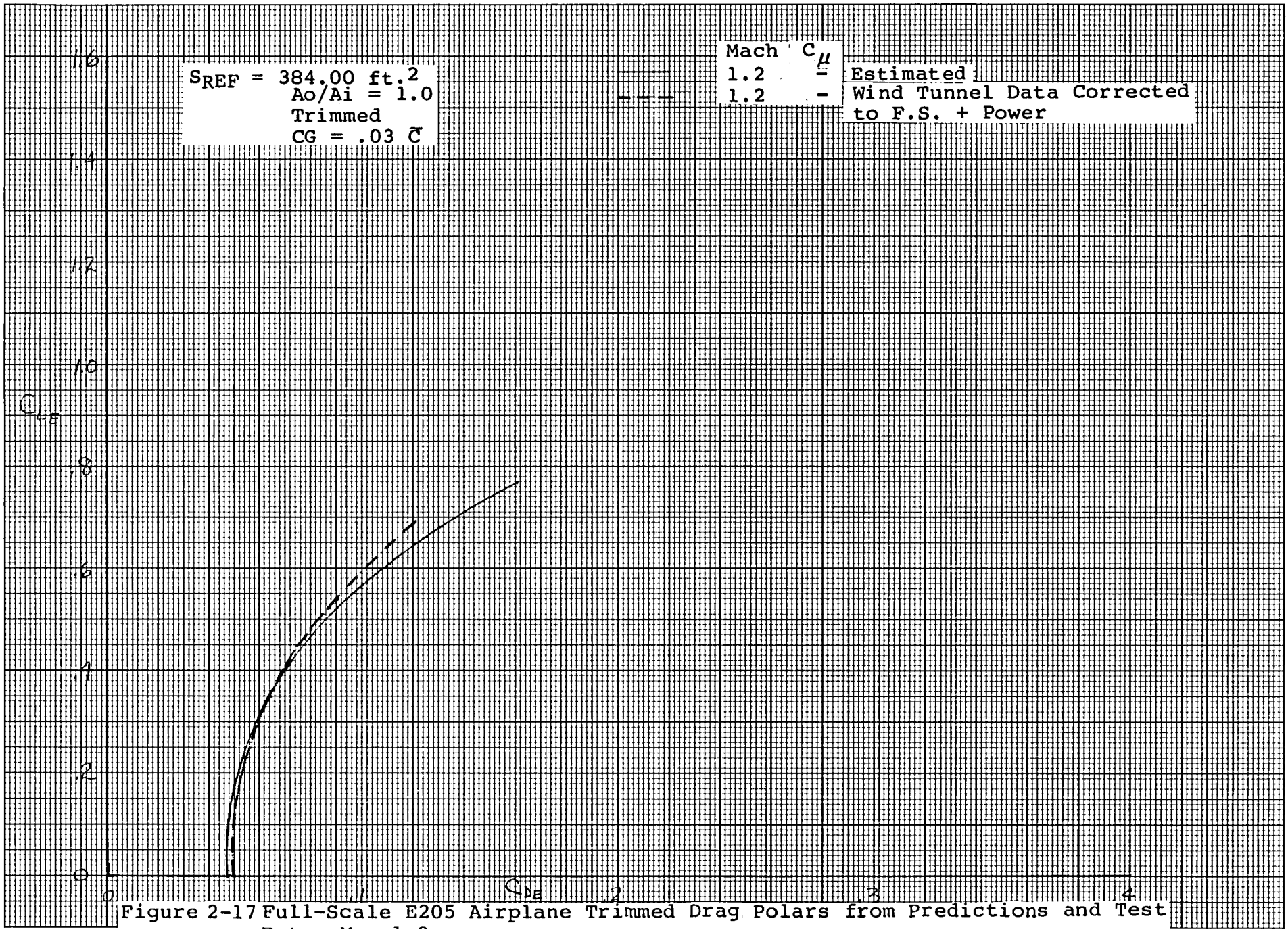

Figure 2-17 Full-Scale E205 Airplane Trimmed Drag Polars from Predictions and Test Data, M = 1.2

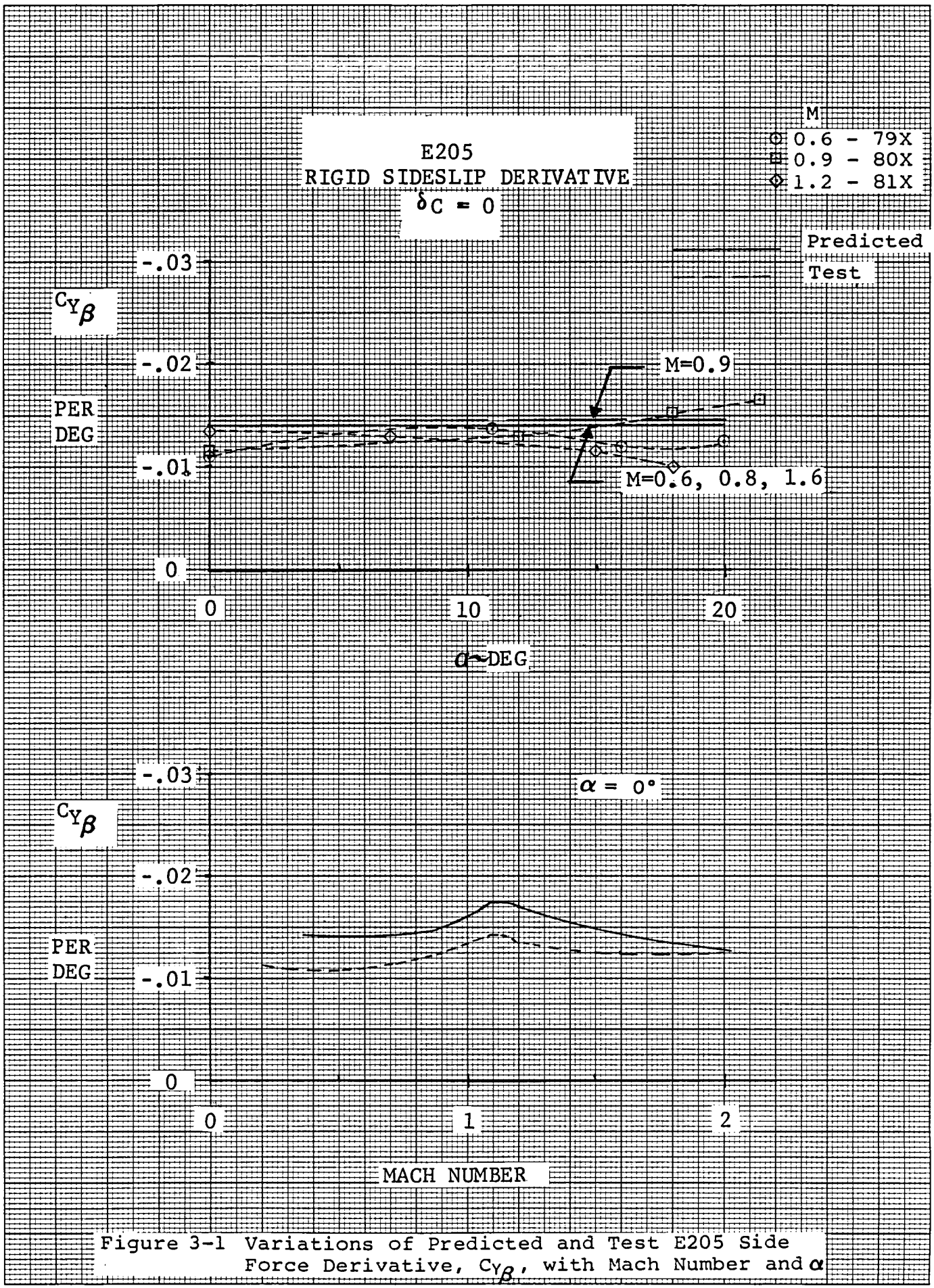

Figure 3-1 Variations of Predicted and Test E205 Side Force Derivative, C_{Y_β}, with Mach Number and α

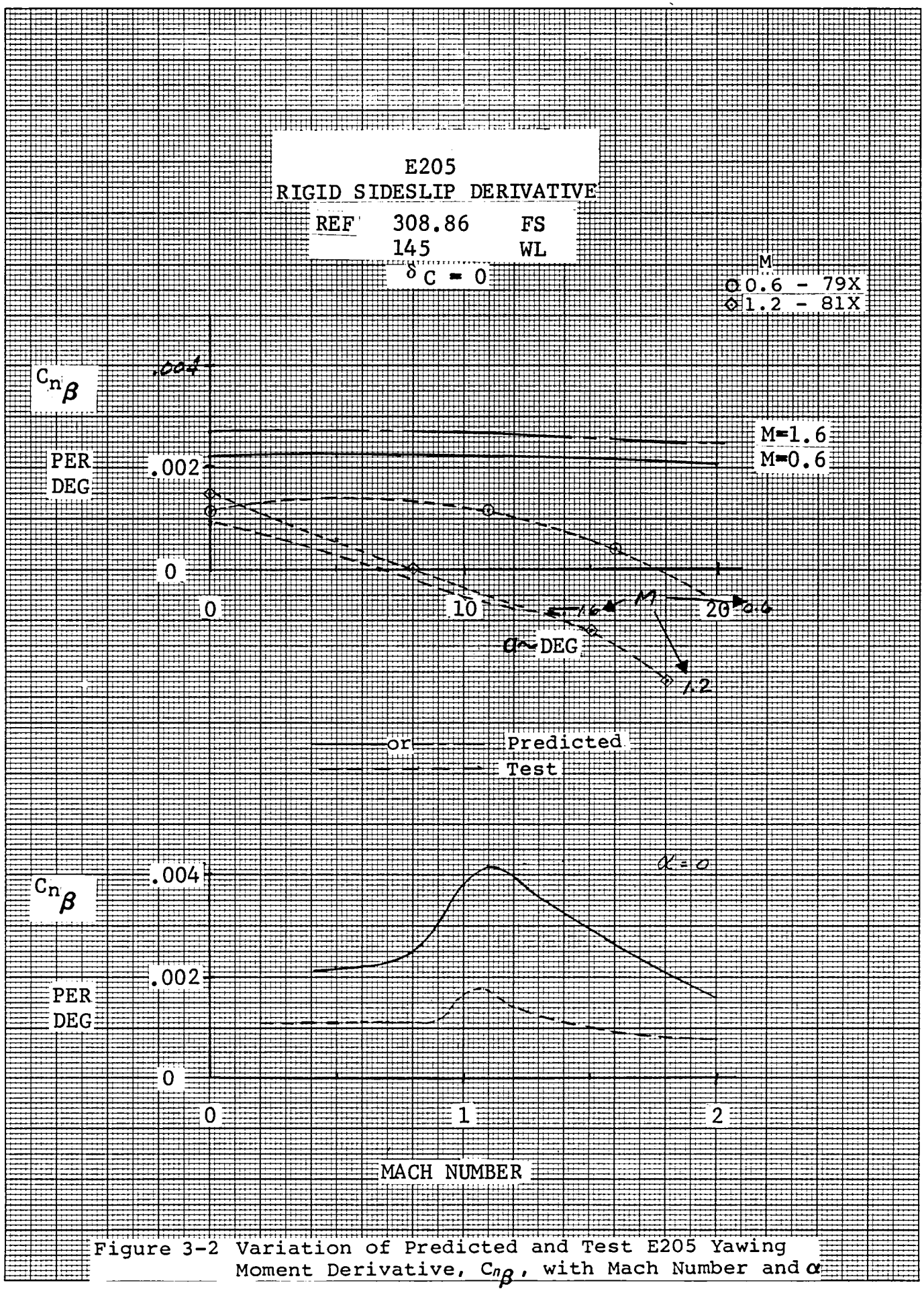

Figure 3-2 Variation of Predicted and Test E205 Yawing Moment Derivative, C_{n_β}, with Mach Number and α

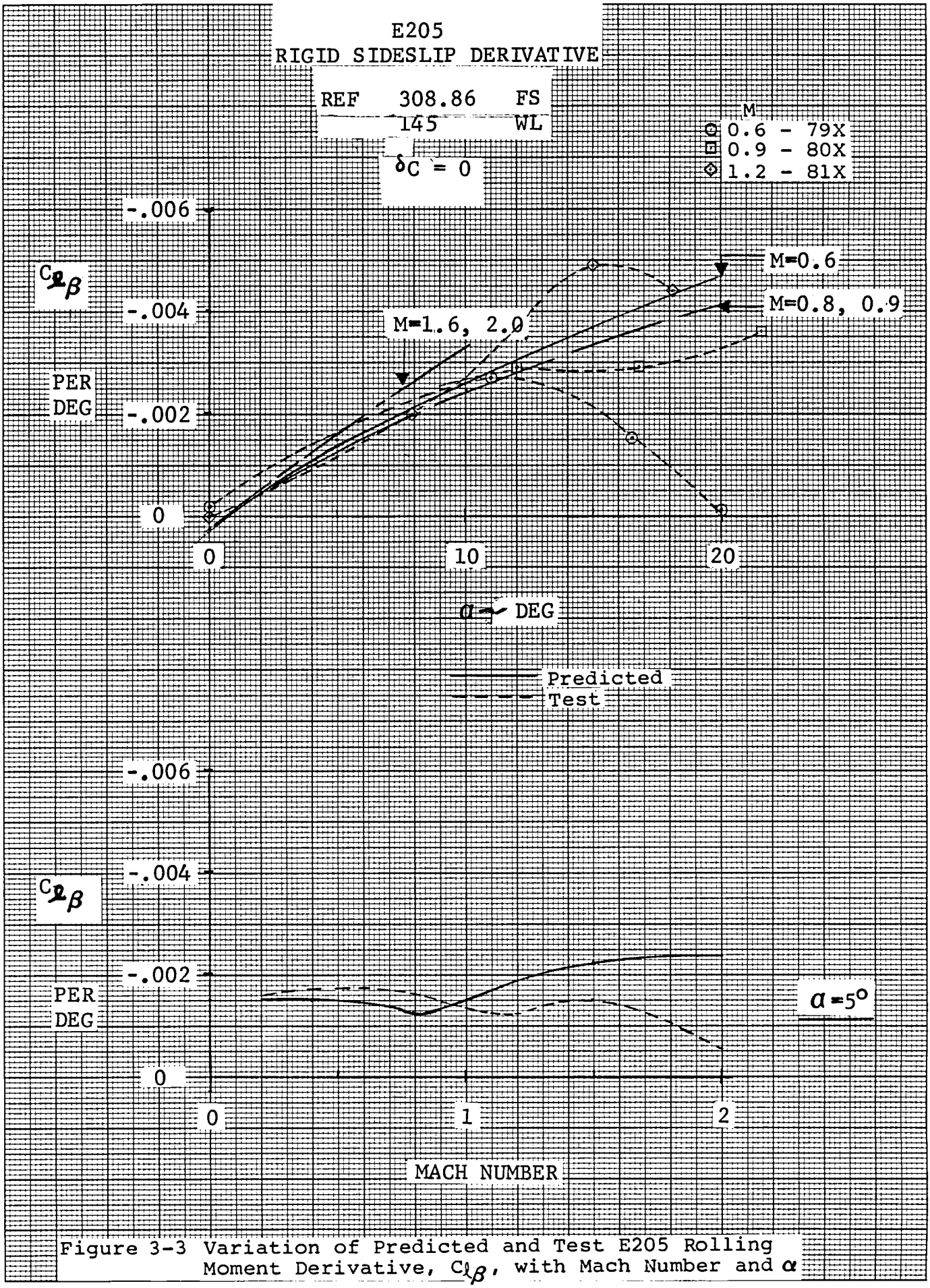

Figure 3-3 Variation of Predicted and Test E205 Rolling Moment Derivative, C_{l_β}, with Mach Number and α

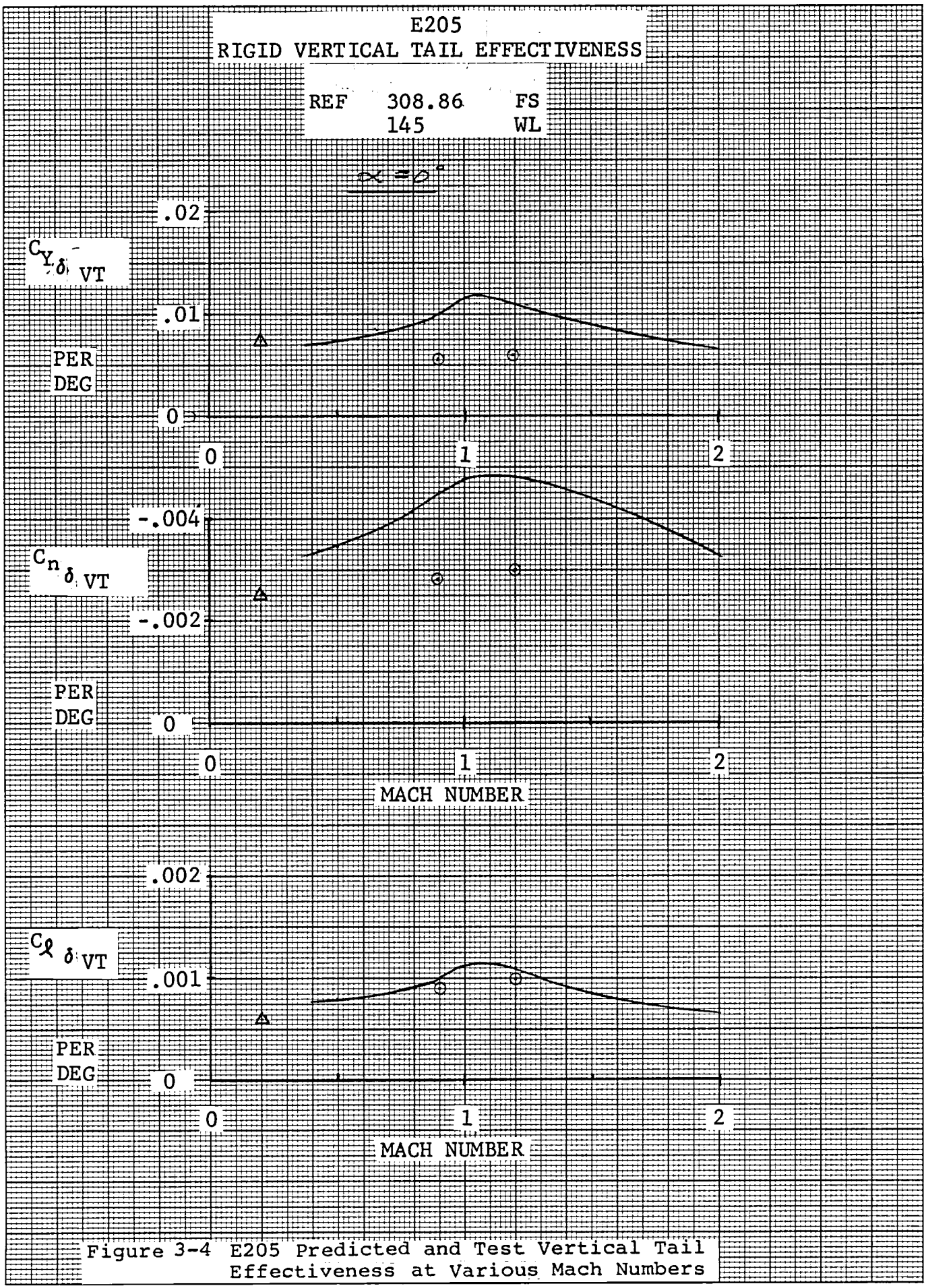

Figure 3-4 E205 Predicted and Test Vertical Tail Effectiveness at Various Mach Numbers

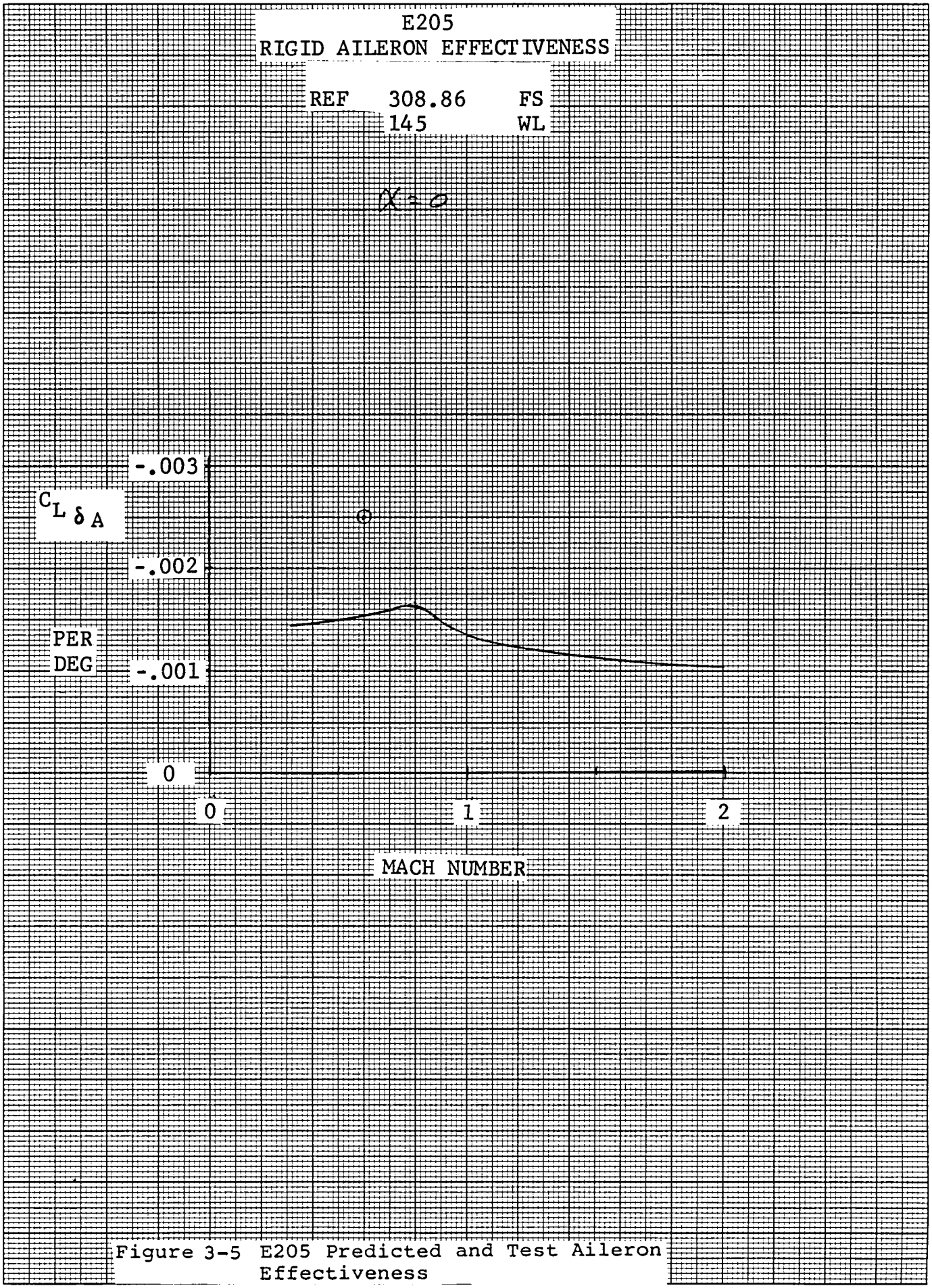

Figure 3-5 E205 Predicted and Test Aileron Effectiveness